Designing Pseudo-Random Staggered PRI Sequences

Rachel Chang

Submitted to the graduate degree program in the Department of Electrical Engineering and Computer Science and the Graduate Faculty of the University of Kansas in partial fulfillment of the requirements for the degree of Master of Science in Electrical Engineering.

Shannon D. Blunt, Chairperson

Committee members

Christopher T. Allen

James M. Stiles

Date defended: July 27, 2023

The Thesis Committee for Rachel Chang certifies
that this is the approved version of the following thesis:

Designing Pseudo-Random Staggered PRI Sequences

Shannon D. Blunt, Chairperson

Date approved: July 27, 2023

Abstract

In uniform pulse-Doppler radar, there is a well known trade-off between unambiguous Doppler and unambiguous range. Pulse repetition interval (PRI) staggering, a technique that involves modulating the interpulse times, addresses this trade-space allowing for expansion of the unambiguous Doppler domain with little range swath incursion. Random PRI staggering provides additional diversity, but comes at the cost of increased Doppler sidelobes. Thus, careful PRI sequence design is required to avoid spurious sidelobe peaks that could result in false alarms.

In this thesis, two random PRI stagger models are defined and compared, and sidelobe peak mitigation is discussed. First, the co-array concept (borrowed from the intuitively related field of sparse array design in the spatial domain) is utilized to examine the effect of redundancy on sidelobe peaks for random PRI sequences. Then, a sidelobe peak suppression technique is introduced that involves a gradient-based optimization of the random PRI sequences, producing pseudo-random sequences that are shown to significantly reduce spurious Doppler sidelobes in both simulation and experimentally.

Acknowledgements

Thank you to the stellar teachers I have encountered in my years at the University of Kansas, for gifting me knowledge I never knew existed. Thank you to my genius advisor Dr. Blunt for the presence and support, and for lighting my research path. And thank you to my lovely partner Noah for sharing this journey with me.

This is for my family, friends, felines, and fans.

This work was supported by the Office of Naval Research under Contract #N00014-20-C-1006.

Contents

1 Introduction **1**

1.1 Waveform Diversity (WD) 1

1.2 Moving Target Indication (MTI) Radar 2

1.2.1 Signal-to-Noise Ratio (SNR) and Coherent Integration 3

1.2.2 Radar Time Scales and the Data Matrix 4

1.2.2.1 Fast-Time/Slow-Time 4

1.2.2.2 Reshaping the Data 5

1.3 Doppler 6

1.3.1 The Doppler Effect and Doppler Shift 6

1.3.2 The Stop-and-Hop Approximation and Doppler Signal Model 8

1.3.3 Doppler Processing 9

1.3.4 Doppler Resolution and Coherent Processing Interval (CPI) 10

1.4 Range 11

1.4.1 Range Determination by Time-Delay 11

1.4.2 Range Resolution and Pulse Compression 12

1.4.2.1 Simple Pulse 12

1.4.2.2 Pulse Compression 13

1.5 Pulse Repetition Frequency (PRF), Interval (PRI), and Unambiguous Measurement 16

1.5.1 Range ambiguities 16

1.5.2 Doppler ambiguities 17

1.5.3 PRF Regimes 18

1.6 PRI Staggering Motivation 19

1.6.1 Random Staggering 21

2 PRI Staggering Model **22**

2.1 Random PRI Generation Methods 22

2.1.1 Cumulative Stagger 22

2.1.1.1 CPI Scaling 24

2.1.2 Grid Stagger 28

2.2 Receive Signal Model and Non-uniform Discrete Fourier Transform (NUDFT) . . 29

2.2.1 Doppler-Dependent Phase Response 29

2.2.2 Receive Signal Model 31

2.2.3 Non-uniform Discrete Fourier Transform (NUDFT) 31

2.2.3.1 Discretization 31

2.2.3.2 Doppler Expansion Factor 32

2.3 Doppler Response 32

2.3.1 Zero-referenced Doppler Response Model 32

2.3.2 Expected and Aggregate Doppler Response 33

2.3.2.1 Expectations 33

2.3.2.2 Aggregated Response Comparison 38

2.3.3 Phase-Doppler Frequency Fan Plots 39

3 Redundancy and the PRI Staggering Co-Array **46**

3.1 The Sparse Array/PRI Staggering Analogy 46

3.2 PRI Staggering Co-array 47

3.3 Redundancy and the Doppler Response 50

3.3.1 Peak Doppler Sidelobe Level 52

3.3.2 Average PDSL Behavior with Stagger Limit 53

3.3.2.1 Redundancy and Grid Staggering 53

3.3.2.2 Redundancy and Cumulative Staggering 56

3.4 Uniqueness of Redundant Sequences . . . 57
3.4.1 PRI Stagger Co-array Revisited . . . 58
3.4.2 Uniqueness . . . 58
3.4.2.1 Uniqueness and Grid Staggering . . . 59
3.4.2.2 Uniqueness and Cumulative Staggering . . . 61

4 Gradient-Based Optimization **64**

4.1 Cost Function and Gradient . . . 64
4.1.1 Cost Function: Generalized Integrated Sidelobe Level (GISL) . . . 64
4.1.2 Gradient . . . 66
4.2 Method . . . 66
4.3 Assessment of PRI Stagger Optimization . . . 67
4.3.1 Optimized Doppler Response . . . 67
4.3.2 Numerical Analysis . . . 70
4.3.2.1 Integrated Doppler Sidelobe Level (IDSL) and Peak Doppler Sidelobe Level (PDSL) Definitions . . . 70
4.3.2.2 IDSL and PDSL Histograms . . . 70
4.3.2.3 PDSL Behavior with Stagger Limit and Optimized Doppler Interval . . . 73
4.3.3 Uniqueness Assessment . . . 75
4.3.3.1 Shuffled Sequences . . . 78
4.3.4 Effect of CPI Scaling . . . 80
4.3.5 Timing Quantization . . . 81
4.4 Experimental Validation . . . 82
4.4.1 Waveform . . . 82
4.4.2 Range-Doppler Maps . . . 83
4.4.3 Callouts . . . 87

5 Conclusions and Future Work **91**

A Derivation of Expected Doppler Response for Grid Stagger Model **93**

B Gradient Derivation **95**

List of Figures

1.1 Signal in noise for different SNR 3

1.2 Reshaping I/Q data stream into fast-time/slow-time radar data matrix 6

1.3 Visualization for the Doppler effect 7

1.4 Doppler response after Doppler processing for a scatterer with Doppler frequency $f_{\mathrm{d}} = \frac{\mathrm{PRF}}{5}$ 10

1.5 Visualization for the concept of resolution in the Doppler context. 11

1.6 Visualization for range determination via time delay 12

1.7 Pulse compression response for matched filter and Hamming-weighted mismatched filter. 15

1.8 Point spread function for $M = 100$ pulses of an LFM with bandwidth $B = 50\ [MHz]$ and pulse width $\tau = 1\ [\mu s]$ 16

1.9 Visualization for unambiguous (orange) and ambiguous (blue) returns 17

1.10 Visualization of Doppler spectrum aliasing showing repeated and overlapping Doppler spectrum (black trace), observed Doppler spectrum, which is the combination of the overlapping spectrum (blue trace), and the nominal unambiguous Doppler interval (orange box) 18

1.11 Visualization for a coherent processing interval containing uniform PRIs and staggered PRIs 20

1.12 Staggered PRI data matrix 20

2.1 Visualization for generating random staggered PRI using the cumulative model where staggers are applied to the interpulse times 23

2.2 Example of smallest possible PRI due to fixing CPI extent 26

2.3 Minimum/Maximum PRI over 1000 trials of $M = 100$ pulse CPIs after scaling, compared with design per-PRI limit and minimum/maximum per-PRI boundary due to scaling 26
2.4 Histogram of randomly generated and scaled PRIs for 1000 trials of $M = 100$ pulses and $\bar{\delta} = 30\%$ 27
2.5 Visualization for generating random staggered PRI using the grid model where staggers are applied to a uniform grid of pulses 28
2.6 Expectation of Doppler response using cumulative staggering model for different number of pulses M and $\bar{\delta} = \pm 30\%$ 33
2.7 Expectation of Doppler response for different limits $\bar{\delta}$ on random cumulative staggering and $M = 100$ pulses 34
2.8 Single instantiation of random cumulative staggering for $\bar{\delta} = \pm 30\%$ limits and $M = 100$ pulses compared to expectation, illustrating Doppler sidelobe variation . . 35
2.9 Expectation of Doppler response using grid staggering model for different number of pulses M and $\bar{\delta} = \pm 30\%$ 36
2.10 Expectation of Doppler response for stagger limits $\bar{\delta}$ from 0% to 40% on random grid staggering and $M = 100$ pulses 37
2.11 Expectation of Doppler response for stagger limits $\bar{\delta}$ from 50% to 90% on random grid staggering and $M = 100$ pulses 37
2.12 Single instantiation of random grid staggering for $\bar{\delta} = \pm 80\%$ limits and $M = 100$ compared to expectation 38
2.13 Max and RMS Doppler response over 1000 random staggering trials comparing average performance between the cumulative and grid models for **(a)** $\bar{\delta} = \pm 10\%$, **(b)** $\bar{\delta} = \pm 20\%$, **(c)** $\bar{\delta} = \pm 30\%$, and **(d)** $\bar{\delta} = \pm 40\%$, ... 39
2.14 Phase-Frequency fan plot of the first 7 pulses for uniform PRI, wrapped phase for visibility, and associated Doppler response with $M = 50$ pulses 41

2.15 Phase-Frequency fan plot of the first 7 pulses for static PRI (alternation between $T = 1/3$ and 1), wrapped phase for visibility, and Doppler response with $M = 50$ pulses 42
2.16 Phase-Frequency slope deflection visualization for cumulative staggering 43
2.17 Phase-Frequency slope deflection visualization for grid staggering 43
2.18 Phase-Frequency fan plot, wrapped phase, and Doppler response for cumulative staggering with $M = 50$ pulses and **(a)** $\pm 10\%$ **(b)** $\pm 40\%$ 44
2.19 Phase-Frequency fan plot, wrapped phase, and Doppler response for grid staggering with $M = 50$ pulses and **(a)** $\pm 10\%$ **(b)** $\pm 80\%$ 45

3.1 CPI translated into impulse train denoting pulse onset times 47
3.2 Single random instantiation impulse train compared to uniform for $M = 20$ pulses . 48
3.3 Coarray for random stagger using grid model achieves low redundancy compared to uniform PRI case for $M = 20$ pulses 48
3.4 Doppler response for random stagger using grid model compared to uniform PRI. . 49
3.5 Coarray for random stagger using grid model with $\bar{\delta} = 90\%$ for two different levels of redundancy controlled by granularity factor K. 51
3.6 Doppler response for random stagger using grid model with $\bar{\delta} = 90\%$ for two different levels of redundancy controlled by granularity factor K. 51
3.7 Coarray for random stagger using cumulative model with $\bar{\delta} = 30\%$ for two different levels of redundancy controlled by granularity factor K. 52
3.8 Doppler response for random stagger using cumulative model with $\bar{\delta} = 30\%$ for two different levels of redundancy controlled by granularity factor K. 52
3.9 Average PDSL for 10^4 random trials of $M = 100$ pulse random grid staggered PRIs with varying $\bar{\delta}$ compared for $K = 5$ (Coarse) and $K = 25$ (Fine) 54
3.10 Histograms of peak Doppler sidelobe level for 10^5 random trials of $M = 100$ pulse random grid staggered PRIs with $\bar{\delta} = 90\%$. 55

3.11 Average PDSL for 10^4 random trials of $M = 100$ pulse random cumulative staggered PRIs with varying $\bar{\delta}$ compared for $K = 5, K = 25$. 56
3.12 Uniqueness metric applied pairwise to 1000 random coarse ($K = 5$) grid stagger sequences of $M = 100$ pulses for different $\bar{\delta}$ 59
3.13 Uniqueness metric applied pairwise to 1000 random fine ($K = 25$) grid stagger sequences of $M = 100$ pulses for different $\bar{\delta}$ 60
3.14 Uniqueness metric applied pairwise to 1000 random (no discretization) grid stagger sequences of $M = 100$ pulses for different $\bar{\delta}$ 60
3.15 Uniqueness metric applied pairwise to 1000 random coarse ($K = 5$) cumulative stagger sequences of $M = 100$ pulses for different $\bar{\delta}$ 61
3.16 Uniqueness metric applied pairwise to 1000 random fine ($K = 25$) cumulative stagger sequences of $M = 100$ pulses for different $\bar{\delta}$ 62
3.17 Uniqueness metric applied pairwise to 1000 random (no discretization) cumulative stagger sequences of $M = 100$ pulses for different $\bar{\delta}$ 62

4.1 Single instantiation of random staggering for M = 100 and compared to gradient-based optimization (9.8 dB PDSL improvement) 68
4.2 Single instantiation of random staggering for M = 100 and compared to gradient-based optimization (8.8 dB PDSL improvement)) 68
4.3 Aggregate mean and maximum of random staggering for M = 100 and compared to gradient-based optimization 69
4.4 Histogram of IDSL for 1000 independent initial and optimized random stagger sequences for $M = 100$, $\bar{\delta} = 30\%$, and $\beta_{\text{opt}} = 4$ 71
4.5 Histogram of PDSL for 1000 independent initial and optimized random stagger sequences for $M = 100$, $\bar{\delta} = 30\%$, and $\beta_{\text{opt}} = 4$ 72
4.6 Histogram of PDSL improvement between 1000 independent initial and optimized random stagger sequences for $M = 100$, $\bar{\delta} = 30\%$, and $\beta_{\text{opt}} = 4$ 73

4.7 Mean PDSL as a function of $\bar{\delta}$ over 1000 independent initial and optimized random stagger sequences for $M = 100$ and $\beta_{\text{opt}} = 4$ 74
4.8 Mean PDSL as a function of Doppler span β_{opt} over 1000 independent initial and optimized random stagger sequences for $M = 100$ and $\bar{\delta} = 30\%$ 75
4.9 Stagger co-array for $M = 100$ pulses in uniform, random, and optimized configurations 76
4.10 Histograms for uniqueness metric applied pairwise within the 1000 random stagger sequences and (separately) within the 1000 optimized sequences for $M = 100$ pulses and $\bar{\delta} = 5\%$ 77
4.11 Histograms for uniqueness metric applied pairwise within the 1000 random stagger sequences and (separately) within the 1000 optimized sequences for $M = 100$ pulses and $\bar{\delta} = 20\%$ 78
4.12 Histogram for uniqueness metric applied between an optimized PRI sequence and 1000 random permutations of the same sequence for $M = 100$ pulses, $\beta_{\text{opt}} = 4$, and $\bar{\delta} = 30\%$ 79
4.13 Histograms of PDSL for $M = 100$, $\bar{\delta} = 30\%$, and $\beta_{\text{opt}} = 4$ with each optimized sequence having the order of its PRIs randomly shuffled 80
4.14 Histograms of initial and optimized PRIs post-scaling for 100 trials with $M = 100$, $\bar{\delta} = 30\%$, and $\beta_{\text{opt}} = 4$ 81
4.15 Geometry of data collect 82
4.16 Simulated Doppler response of hypothetical mover at the speed limit for random instantiation and corresponding optimized staggering for $M = 100$, $\bar{\delta} = \pm 30\%$, and $\beta_{\text{opt}} = 8$ (6.8 dB PDSL improvement) 83
4.17 Range-Doppler Map of intersection 23rd and Iowa Streets in Lawrence, Kansas. Uniform PRF at 800 Hz uncovers ground truth. 84
4.18 Range-Doppler Map of intersection 23rd and Iowa Streets in Lawrence, Kansas. Using uniform PRF at 400 Hz, scene is heavily aliased. 85

4.19 Range-Doppler Map of intersection 23rd and Iowa Streets in Lawrence, Kansas. Random staggering uncovers aliased attributes at the cost of increased and random sidelobes that could result in false alarms. 86
4.20 Range-Doppler Map of intersection 23rd and Iowa Streets in Lawrence, Kansas. Pseudo-random optimized staggering flattens the peaks from the random case. . . . 86
4.21 Doppler slice for range cell containing Mover 2 showing 4.9 dB PDSL improvement via optimization 87
4.22 Doppler slice for range cell containing Mover 3 showing 3.9 dB PDSL improvement via optimization 88
4.23 Zoomed range-Doppler response of sidelobes from Mover 1 for random staggering 89
4.24 Zoomed range-Doppler response of sidelobes from Mover 1 for pseudo-random optimized staggering 89

List of Tables

3.1 Maximum, Minimum, and Median PDSL over 10^5 random trials of coarse ($K = 5$) and fine ($K = 25$) grid staggering. 56

3.2 Maximum, Minimum, and Median PDSL over 10^5 random trials of coarse ($K = 5$) and fine ($K = 25$) cumulative staggering. 57

Chapter 1

Introduction

1.1 Waveform Diversity (WD)

The term radar encompasses a wide range of techniques using radio waveforms to ascertain aspects about an illuminated scene, including the range, radial velocity, direction, size, or material of scatterers. Transmission (active or passive), subsequent scattering, reception, and processing of radio waves are used to perform a plethora of tasks, including imaging, detection, and tracking, based on attributes of the received signal like timing, phase, power, and polarization. Clearly radar is a broad field with many features. This thesis focuses on a particular type of radar system called Moving Target Indication (MTI) radar that uses pulsed waveform transmissions to recover information about the velocity of illuminated scatterers.

Technology has advanced tremendously in the past 60 years, leading to the burgeoning research and development area of Waveform Diversity (WD)[1, 2, 3, 4]. Different radar signal structures possess different properties that can be utilized for various applications, and with hardware advancements the possibilities for physical realization of waveforms have grown. Thus modulation of one/many attribute(s) of the radar signal (along with receive processing) can be the vehicle by which to address many challenges in radar [5]. This thesis specifically contributes to the WD category of waveform design and optimization by examining a pulse-by-pulse modulation strategy that is used to shape the Doppler spectrum response. This is a transmission scheme referred to as *random PRI staggering* (Section 1.6), where pulses are transmitted at non-uniform and random time intervals, and is used to mitigate Doppler ambiguities (Section 1.5) at the cost of increased Doppler sidelobes [6, 7]. The work presented in this thesis builds upon [7, 8, 9] and addresses this trade-

off. First, Chapter 1 provides context and background information for readers unfamiliar with MTI radar. Next, two generation methods for random (PRI) staggering are presented and compared in Chapter 2. Then Chapter 3 discusses the impact of redundancy in the interpulse times for both models. Last, a gradient-based optimization of the interpulse times is performed, analyzed, and experimentally demonstrated in Chapter 4.

1.2 Moving Target Indication (MTI) Radar

Radar waveforms are typically configured according to two classes: Continuous-wave (CW) or pulsed. CW radar, aptly named, continuously transmits a waveform and often employs a bistatic configuration (transmitter and receiver separated) to prevent receiver damage from high-powered transmissions. On the other hand, a pulsed radar emits short bursts, with some amount of time between pulses during which a collocated receiver can operate [10].

Pulsed radar offers isolation between a collocated transmitter and receiver, and an object's radial velocity relative to the radar (Section 1.3) and range (Section 1.4) can be determined simply, though trade-offs do arise. The peak transmit power of a pulsed system must be higher to realize sufficient energy-on-target [10, 11]. Additionally, while a pulse is transmitted, the receiver is turned off to avoid damage, thus creating a *blind range* (shown in Fig. 1.6) within which returns from objects cannot be received (therefore the objects remain undetected) [10, 12].

In a pulsed radar system, information obtained using a pulsed transmission scheme is exploited to determine information about the radial velocity of scattering objects in the illuminated scene. The pulsed data is used to eliminate returns from non-moving scatterers known as clutter (a mode known as Moving Target Indication (MTI)), and/or to determine the specific radial velocity of moving objects (Pulse-Doppler) [10, 12, 13] . Since MTI can be done by dedicated spectral analysis via a bank of Doppler filters, and both MTI and pulse-Doppler radar can consist of clutter rejection and specific velocity analysis, the line between MTI and pulse-Doppler radar has become blurred [12]. The following discussion will rely on the distinction in [12], where MTI is defined as those radars which operate with *pulse repetition intervals* (PRIs) low enough to avoid range ambiguities

(discussed in Section 1.5), and pulse-Doppler radars use high PRFs which incur range ambiguities. In this thesis, PRIs are designed to avoid range ambiguities, so the following development and analysis are in the context of an MTI mode radar.

The following sections in this chapter provide a basic overview of the theory of operation for MTI radar (and radar in general) and introduce some important concepts that arise from a pulsed system.

1.2.1 Signal-to-Noise Ratio (SNR) and Coherent Integration

Signal-to-Noise Ratio. SNR is a metric that describes the quality of a measured signal. Fig. 1.1 illustrates the importance of an adequate SNR by depicting a sinusoid in noise for varying degrees of SNR. When the ratio is low, the signal is difficult (maybe impossible) to distinguish from the noise. It is obvious then, why a high SNR is desireable.

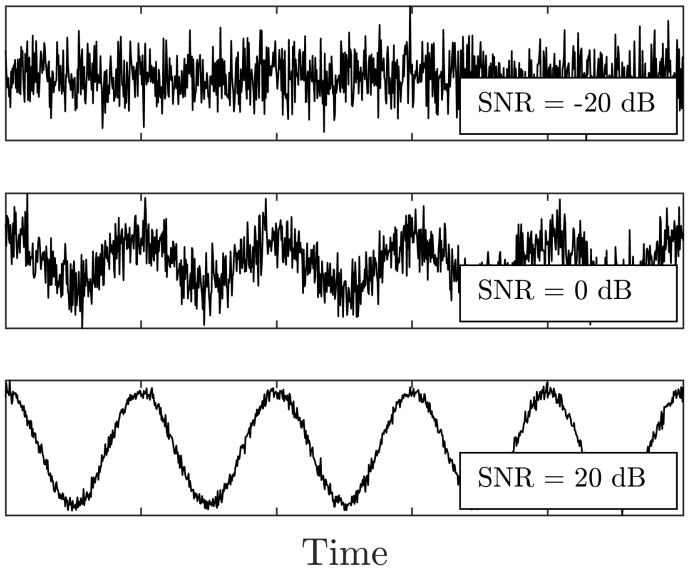

Figure 1.1: Signal in noise for different SNR

The signal-to-noise ratio is [10, 11, 12]

$$\text{SNR} = \frac{P_\text{t} G_\text{t} G_\text{r} \lambda^2 \sigma}{(4\pi)^3 R^4 k T_0 F B_\text{r}} \tag{1.1}$$

for P_t the transmitted power [W],

G_t the transmitter antenna gain,

G_r the receiver antenna gain,

λ the transmit wavelength [m],

σ the mean RCS of the scatterer in [m^2],

R the range from the scatterer to the radar [m],

k Boltzmann's constant ($1.38 \times 10^{-}23$ [W-s/K]),

T_0 the standard temperature (290 [K]),

B_r the receiver bandwidth [Hz],

and F the noise figure of the receiver. Only some of the variables found in Eq. 1.1 are within the radar engineer's control. One could improve SNR by increasing transmit power, transmit and/or receive gain, transmit wavelength, or decreasing the receiver bandwidth (while maintaining adequate bandwidth to capture the signal of interest), though tuning any of these variables has associated costs that may not be acceptable for a given application.

Coherent Integration. SNR is often improved via coherent integration (or summing) of pulsed data. This is done by adding associated complex data samples. Since noise is uncorrelated, summing the samples averages out noise while coherently combining signal components, thereby improving the SNR by factor M, the number of pulses.

1.2.2 Radar Time Scales and the Data Matrix

1.2.2.1 Fast-Time/Slow-Time

In pulse-Doppler radar using a single transmitter and receiver, data is sampled in two different time dimensions, delineated by their relative time scales. The first is the *fast-time* dimension, which consists of the data points obtained by I/Q sampling and corresponds to time delay (a.k.a. range, discussed in Section 1.4). The fast-time sampling rate (determined by the receiver analog-to-digital converter (ADC)) must be greater than or equal to the transmit signal's bandwidth per

the Nyquist-Shannon sampling theorem (which describes the criterion for the interchangeability of analog and digital signals) [14, 15]. The second dimension is referred to as *slow-time*, formed by pulse-to-pulse sampling and used to determine Doppler shift information (Section 1.3). When using a fixed time interval between pulses the slow-time sampling rate, more commonly referred to as the *pulse repetition frequency* (PRF, the inverse of PRI), should exceed the Doppler bandwidth to achieve Nyquist sampling and avoid ambiguities (more on this in Section 1.5). However, a non-uniform slow-time sampling structure as imposed by PRI staggering can uncover such ambiguities while maintaining the use of a low average PRF.

1.2.2.2 Reshaping the Data

The output of the receiver ADC is simply a stream of data samples. The data is reshaped into a matrix by aligning the range samples of each pulse, so that processing can be performed across the different dimensions. The data matrix is discussed in [10, 11] , which further extends the concept to a data cube that considers multiple antenna elements with spatial separation. In Fig. 1.2, a visualization of the reshaping process into a fast-time/slow-time data matrix for a uniform PRI arrangement is shown, with the green cells denoting the first sample of a pulse. The columns of this matrix are referred to as *range bins*, which are sampled returns from the same range across the pulses. Performing Doppler processing (Section 1.3.3) for each range bin coherently integrates the complex data and transforms the pulse dimension into a Doppler dimension. By doing so, Doppler processing produces *Doppler bins* which contain the range response at each bin's respective discretized Doppler frequency.

The rows of this matrix correspond to the pulse number, and consist of returns across the entire *range swath*, or sampled range extent. Pulse compression (Section 1.4.2.2) is performed in the fast-time dimension for each pulse.

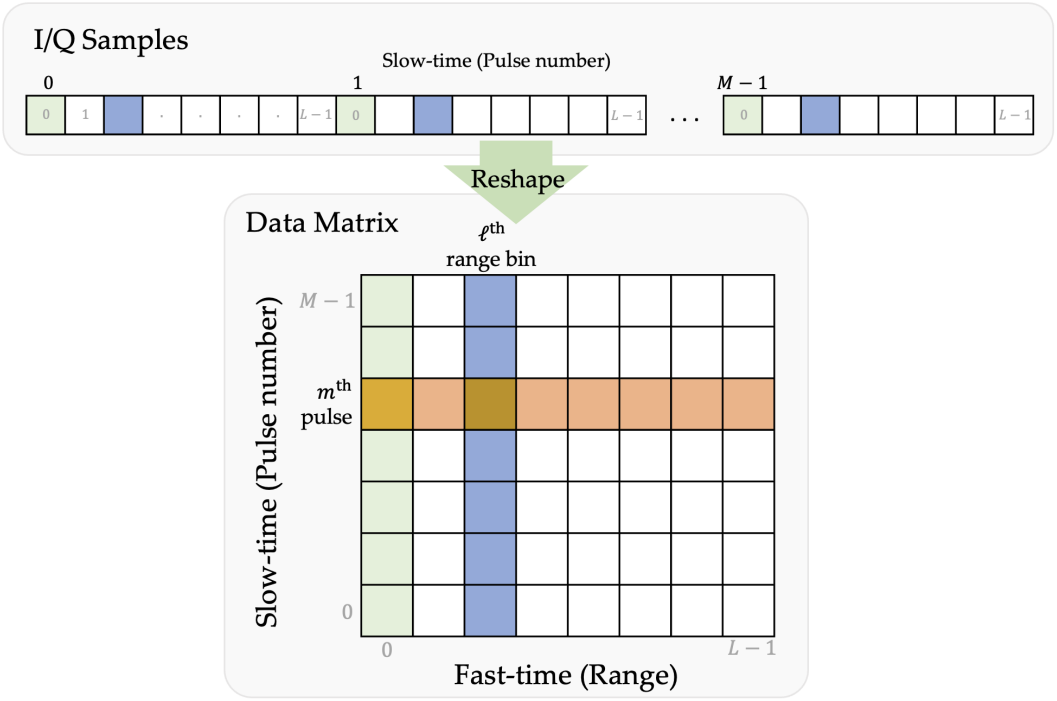

Figure 1.2: Reshaping I/Q data stream into fast-time/slow-time radar data matrix

1.3 Doppler

1.3.1 The Doppler Effect and Doppler Shift

The Doppler effect refers to the phenomenon predicted by special relativity [16, 17, 18] where the frequency of a wave is changed relative to an observer due to the motion of an object producing the wave. This effect is familiar to many in the exemplary auditory pitch shift produced by a moving firetruck blaring its sirens, a visualization of which is shown in Fig. 1.3. As the firetruck moves towards Observer 1, the wave is emitted from a progressively closer distance, thereby producing a contraction of the wavelength (higher observed frequency). Inversely, as the firetruck moves away from Observer 2, the wave is emitted at progressively further positions and the observed wavelength is dilated (lower observed frequency). Only when the object's radial velocity relative to the observer is zero (as is the case for Observer 3) is the original frequency of the emitted wave observed.

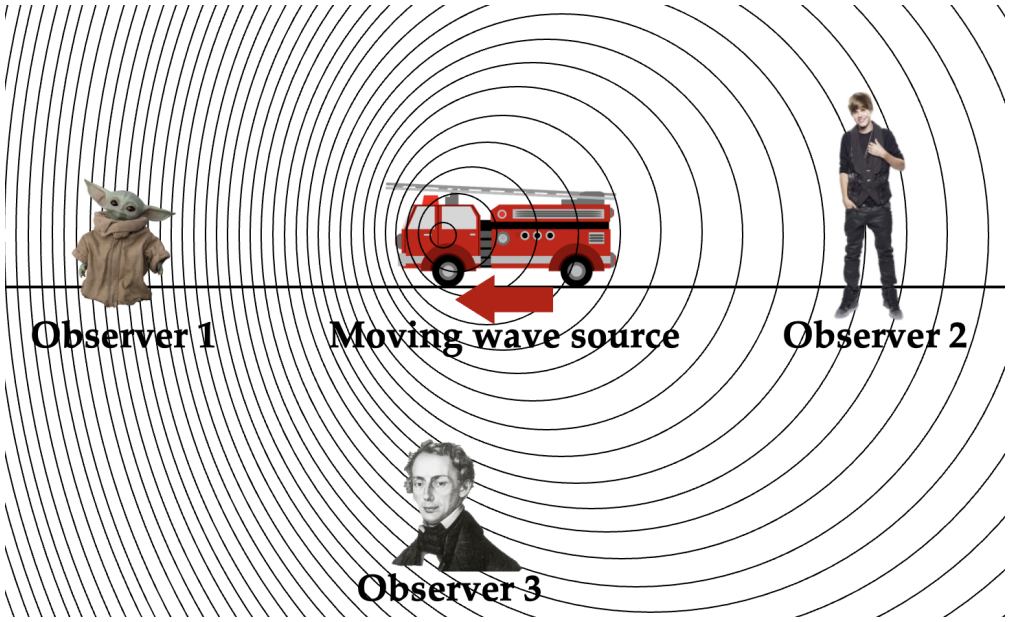

Figure 1.3: Visualization for the Doppler effect

The Doppler effect is observed for all types of waves. In fact, the phenomenon was first proposed by Austrian physicist Christian Doppler (Observer 3 from Fig. 1.3) in 1842 in the context of electromagnetic waves emitted by stars [16] . Specifically in MTI radar, the received electromagnetic wave's frequency f_r induced by the Doppler effect is exploited to cancel clutter and determine the radial velocity of moving objects.

For a monostatic radar (transmitter and receiver are collocated), the received frequency is predicted as

$$f_\mathrm{r} = \left(\frac{1+v/c}{1-v/c}\right) f \tag{1.2}$$

for v the instantaneous radial velocity of the object relative to the radar, c the speed of light, and f the transmit frequency [10, 11] . Due to this functional dependence, knowledge about the velocity of an object can be obtained by analyzing the frequency of the received signal.

The difference between the transmitted frequency f and the received frequency f_r is called *the Doppler shift*, or the *Doppler frequency*. For radar applications, the velocity of an object is in all likelihood only a small fraction of the speed of light, so the Doppler shift at a specific time instance

can be approximated by [10, 11, 12, 13]

$$f_{\mathrm{d}} \approx f - (1+2(v/c))\, f \tag{1.3}$$

$$= \frac{2v}{c} f \tag{1.4}$$

$$= \frac{2v}{\lambda} \tag{1.5}$$

for λ the transmit wavelength. A justification for this simplification relying on binomial expansion can be found in [10] and [11].

1.3.2 The Stop-and-Hop Approximation and Doppler Signal Model

Since the instantaneous velocity of an object is almost always only a small fraction of the speed of light, objects can be considered *quasi-stationary* [11] . In essence this means that the distance an object moves during the time it takes for a waveform to travel from the transmitter to the object is negligible. Under the quasi-stationary assumption, the "stop-and-hop" model offers a simplified view of the received signal due to object movement [11] . Since movement is assumed to cease while the transmitted pulse travels to the object (hence the term "stop"), the waveform envelope is unchanged during transit, and motion is captured as a series of range-dependent phases at each pulse (hence the term "hop"). Thus, velocity information is contained in the received slow-time signal, which for uniform pulse intervals is given by

$$y_{\mathrm{st,u}}(m) = A\exp[-j\frac{4\pi}{\lambda}R(mT)] \tag{1.6}$$

$$= A\exp[-j2\pi\phi(mT)] \tag{1.7}$$

where A is the amplitude, $m = 0, 1, ...M-1$, T is the PRI, and the term $\phi(mT)$ in the exponential constitutes the phase-modulation due to the object's range at time mT ($R(mT)$). Effectively this presents a phase sampling at a rate equal to the *pulse repetition frequency* (PRF). The time rate of

change of this phase signal

$$\frac{\Delta\phi(mT)}{\Delta mT} = \frac{2}{\lambda}\frac{\Delta R(mT)}{\Delta mT} \tag{1.8}$$

$$= \frac{2}{\lambda}v(mT) \tag{1.9}$$

is the approximate Doppler shift frequency from Eq. 1.5. Thus, the received slow-time data series gives rise to a complex sinusoid at the Doppler frequency f_{d} associated with the particular radial velocity. Explicitly stating the dependence on Doppler frequency, the slow-time received signal in Eq. 1.6 becomes

$$y_{\mathrm{st,u}}(m, f_{\mathrm{d}}) = A\exp[-j2\pi f_{\mathrm{d}} mT]. \tag{1.10}$$

1.3.3 Doppler Processing

Under the "stop-and-hop" model presented in the previous section, Doppler information is carried in the slow-time-sampled phase signal. Thus the response obtained via Doppler processing is waveform-agnostic. This section briefly discusses the theory behind traditional Doppler processing, with specific details pertaining to the PRI staggering model (the topic of this thesis) divulged in Section 2.2.

Doppler processing consists of a spectral analysis of the slow-time data at a specific range bin. The Doppler response is traditionally obtained by evaluating the discrete Fourier transform (DFT) of the slow-time phase signal [10, 11, 13, 19]. For a uniform PRI system, redundancies can be exploited and the famous and efficient fast Fourier transform (FFT) algorithm [19] can be used.

The uniform DFT of the slow-time scattering at the ℓ^{th} range bin is

$$u_{\mathrm{st,u}}(\ell, f_{\mathrm{d}}) = \sum_{m=0}^{M-1} y_{\mathrm{st,u}}(\ell, m)\,\exp[-j2\pi f_{\mathrm{d}} mT], \tag{1.11}$$

for $y_{\mathrm{st,u}}(\ell, m)$ the slow-time received sample from Eq. 1.10 at the m^{th} pulse, f_{d} the Doppler fre-

quency, and T the PRI. $20\log_{10}(|\bullet|)$ of the Doppler spectrum from Eq 1.11 is shown in Fig. 1.4 for a scatterer at arbitrary range with Doppler shift $f_\mathrm{d} = \frac{\mathrm{PRF}}{5}$. The uniform PRI Doppler spectrum exhibits a familiar periodic-sinc structure.

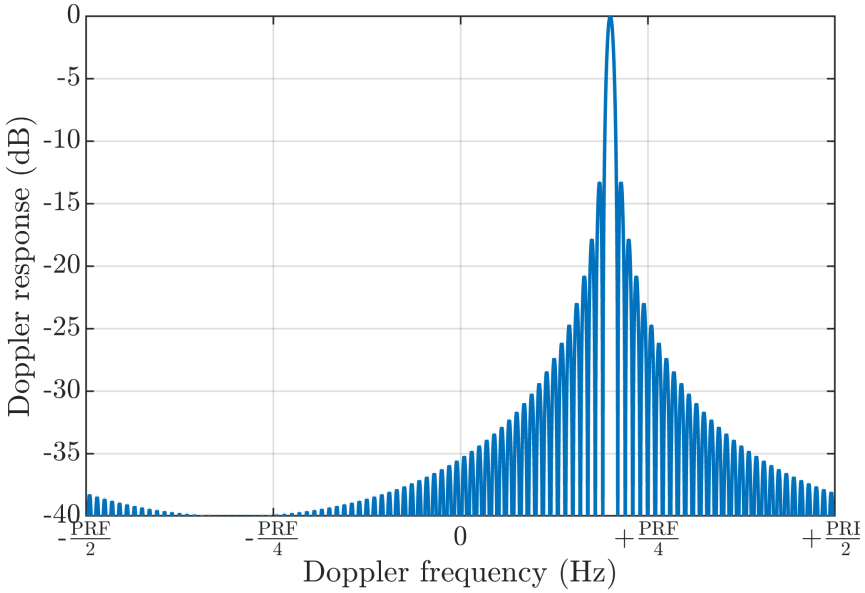

Figure 1.4: Doppler response after Doppler processing for a scatterer with Doppler frequency $f_\mathrm{d} = \frac{\mathrm{PRF}}{5}$

Doppler processing performs coherent integration and transforms the data matrix in Section 1.2 from an $M \times L$ matrix to an $N \times L$ matrix, for N the number of Doppler bins.

1.3.4 Doppler Resolution and Coherent Processing Interval (CPI)

In a pulsed-radar system, the overall time extent of a pulse sequence transmission is called the *coherent processing interval*:

$$T_\mathrm{CPI} = MT \tag{1.12}$$

for M pulses and T the fixed PRI in seconds.

The term resolution refers to the ability to distinguish or *resolve* more than one object from another in a given dimension. If no window is applied, the Rayleigh (peak-to-null) resolution in

the Doppler dimension is [10]

$$\Delta f_{\mathrm{d}} = \frac{1}{T_{\mathrm{CPI}}} = \frac{1}{MT}. \tag{1.13}$$

The application of a window would have the effect of widening the mainlobe by a factor dependent on the particular window used [10]. The concept of resolution in the Doppler context is illustrated in Fig. 1.5, where it is shown that the Doppler response mainlobes from objects with Doppler frequency spacing greater than or equal to the Doppler resolution are separable, but the returns from objects with lesser spacing are overlapping and therefore difficult to parse.

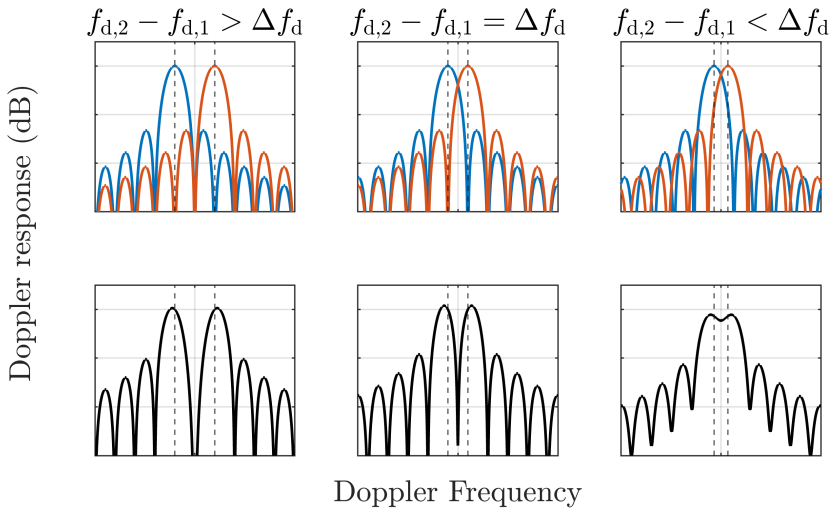

Figure 1.5: Visualization for the concept of resolution in the Doppler context.

1.4 Range

1.4.1 Range Determination by Time-Delay

In a pulsed-Doppler radar system, range is determined by the time delay between the transmission and reception of the waveform [10, 11, 13]. An illustration of this concept is shown in Fig. 1.6. The time delay ΔT accounts for the two-way pulse transit which consists of both the time for the pulse to reach an object plus the time for the pulse to return to the receiver (respectively labeled

t_t and t_b for time *there* and *back*). Since $t_t = t_b$, the range of an object can be determined via

$$R = \frac{c(t_t + t_b)}{2} = \frac{c\Delta T}{2}, \tag{1.14}$$

where c is the speed of light, and ΔT is the two-way time between the radar and the scatterer.

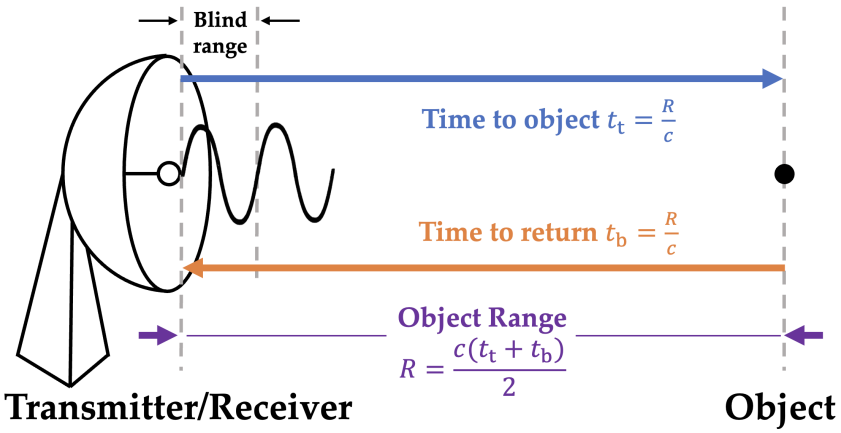

Figure 1.6: Visualization for range determination via time delay

The timing precision and thereby range precision is dependent on the receiver's analog-to-digital converter (ADC), which performs in-phase and quadrature (I/Q) sampling at a finite clock rate [10]. These range samples are referred to as *range bins*.

1.4.2 Range Resolution and Pulse Compression

1.4.2.1 Simple Pulse

When the transmit waveform is a simple time-gated sinusoid, the range resolution is proportional to the pulse width τ by [10]

$$\Delta R = \frac{c\tau}{2}, \tag{1.15}$$

which is approximately the blind range [10]

$$R_{\text{blind}} = \frac{c(\tau + t_{switch})}{2}, \tag{1.16}$$

for t_{switch} the Transmitter/Receiver switch time. The term *pulse eclipsing* refers to the scenario when all or part of a pulse return occurs during a pulse transmission. During this time, the receiver is turned off and the pulse return is not received. This phenomenon creates a *blind zone*, wherein objects cannot be detected due to the effect of eclipsing.

1.4.2.2 Pulse Compression

Finer resolution requirements can be met by decreasing the pulse width per Eq. 1.15, though shorter pulse times correspond to less transmitted power, leading to possible SNR issues. A common technique to address the SNR/range resolution trade-off is *pulse compression*, which introduces intrapulse modulation to decouple the two, enabling the use of longer pulses to meet energy requirements while improving the range resolution [10, 11]. With pulse compressed waveforms, the range resolution is no longer dependent on the transmitted pulse width but rather the bandwidth of the signal as

$$\Delta R = \frac{c}{2B}. \tag{1.17}$$

Linear Frequency Modulated (LFM) Waveform. The most common pulse compression waveform used in radar is the linear frequency modulated (LFM) waveform, known for it's Doppler tolerance [20] and ease of generation. The baseband LFM pulse is defined as [10, 11, 12, 5]

$$s_{\text{LFM}}(t) = A\exp\left[-j2\pi\left(\frac{B}{\tau}t^2\right)\right], \qquad -\frac{\tau}{2} \leq t \leq \frac{\tau}{2}, \tag{1.18}$$

for A the amplitude, B the bandwidth, and τ the pulsewidth. The baseband LFM's frequency function is simply a linear sweep from $-B/2$ to $B/2$.

Matched Filter. Pulse compression is performed by filtering the received signal with an appropriate filter that is correlated with the transmit signal. The matched filter, which maximizes SNR, is given by [5, 10, 11, 12]

$$h_{\mathrm{mf}}(t) = as^*(-t), \tag{1.19}$$

where a is an arbitrary scalar, $s(t)$ is the transmit waveform, and * denotes complex conjugation. In words, the matched filter is a (possibly scaled,) time-reversed and complex conjugated version of the transmit waveform. While beyond the scope of this thesis, the derivation for the range resolution for a pulse compression waveform in Eq. 1.17 (based on the Fourier uncertainty principle) and matched filter in Eq. 1.19 (based on maximum SNR), and more pulse compression waveforms can be found in [5, 10, 11, 12]. Discretizing Eq. 1.19 and allowing the scale factor to vary with time yields

$$h[n] = a[n]s^*[-n]. \tag{1.20}$$

When the weights $a[n]$ are equal for all $n = 0, 1, .., N-1$, Eq. 1.20 becomes the discretized matched filter. However $a[n]$ can be chosen such that specific properties of the pulse compression response

$$x[n] = \sum_{\ell} h[n]y[n-\ell] \tag{1.21}$$

are achieved, an approach known as *tapering*. Here $y[n]$ is the receive signal discretized via I/Q sampling. $20\log_{10}(|\bullet|)$ of the zero-delay referenced pulse compression response for an LFM waveform with a matched filter and Hamming-weighted mismatched filter are compared in Fig. 1.7. The matched filter produces a response with a higher peak, which is unsurprising given that it is derived to achieve maximum SNR. But the tapered mismatched filter exhibits dramatic sidelobe reduction compared to the matched filter response. The cost of slight mismatch loss due to tapering is overwhelmed by the sidelobe benefit. Because the focus of this thesis is the behavior of Doppler

sidelobes, the mitigation of range sidelobes that could obscure Doppler sidelobe performance is important, which justifies the use of a Hamming-weighted mismatched filter in Section 4.4.

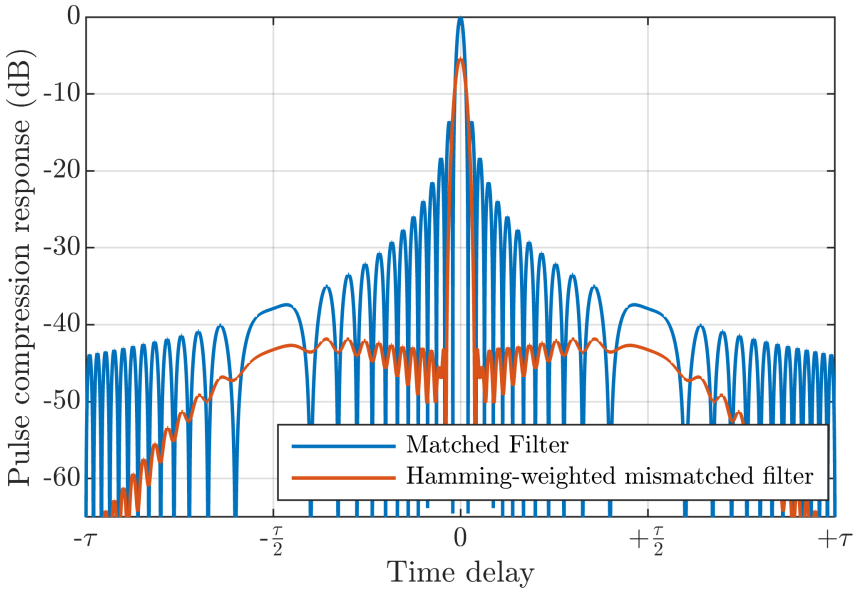

Figure 1.7: Pulse compression response for matched filter and Hamming-weighted mismatched filter.

Point Spread Function. When considering only the scattering from a point target at zero-delay and zero-Doppler, the output of pulse compression and Doppler processing is the *point spread function* (also referred to as the *point spread response*) [12, 21]. For $M = 100$ pulses of an LFM of bandwidth $B = 50$ $[MHz]$ and pulse width $\tau = 1$ $[\mu s]$, the point spread function is shown in Fig. 1.8. The zero-delay cut is a zero-referenced version of the Doppler response in Fig. 1.4, and the zero-Doppler cut is the matched filter response from Fig. 1.7.

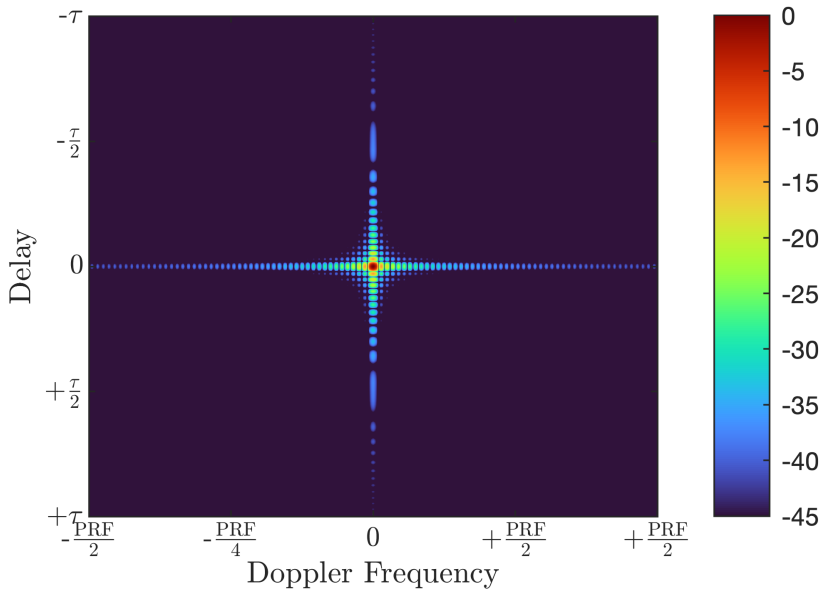

Figure 1.8: Point spread function for $M = 100$ pulses of an LFM with bandwidth $B = 50$ $[MHz]$ and pulse width $\tau = 1$ $[\mu s]$

1.5 Pulse Repetition Frequency (PRF), Interval (PRI), and Unambiguous Measurement

1.5.1 Range ambiguities

In Section 1.4.1 it was discussed that an object's range may be determined via the two-way delay time from transmission to reception. Consider a case when the delay is longer than the interpulse interval ($\Delta T > T$). The reception of the pulse occurs *after* the transmission of the next pulse, thereby rendering the measurement *ambiguous*, since the pulse from which the return came cannot be discerned. Fig. 1.9 illustrates (for a uniform PRI) a received pulse from an object at an unambiguous range (orange pulses), as well as one from an ambiguous range (blue pulses). The ambiguous pulse return appears to occur at a closer range determined by ΔT_{obs} than in reality. In a fixed PRI system, the ambiguous return appears at the same range for each pulse.

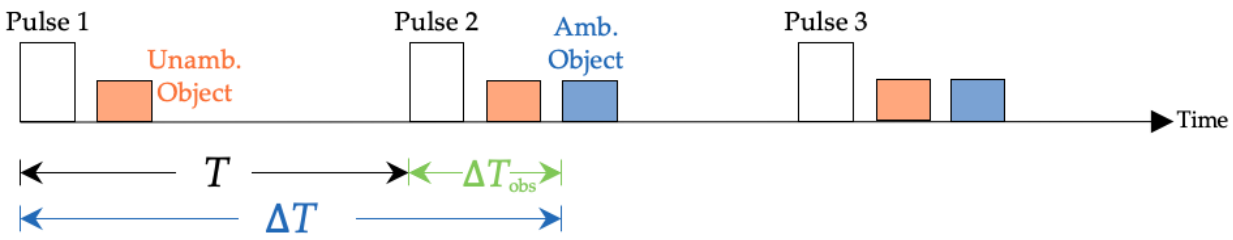

Figure 1.9: Visualization for unambiguous (orange) and ambiguous (blue) returns

To avoid the need for more complicated processing to unwrap these range ambiguities, the PRI can be designed to encompass the desired unambiguous range swath by

$$\text{PRI} = T \geq \frac{2R_{\max}}{c} \tag{1.22}$$

for $R_{\max}$ the desired maximum unambiguous range and c the speed of light.

1.5.2 Doppler ambiguities

As discussed in the previous section, for a uniform PRI system the PRI is proportional to the maximum unambiguous range. Thus mitigation of range ambiguities can be achieved via longer PRI, corresponding to lower PRF. However, recall that the PRF is the slow-time (Doppler) sampling rate, and by the Nyquist-Shannon sampling theorem for complex signals this rate is proportional to the unambiguous signal bandwidth. Thus the maximum Doppler frequency that can be unambiguously measured is

$$f_{\text{d,max}} = \pm\frac{\text{PRF}}{2} = \pm\frac{1}{2\text{PRI}}. \tag{1.23}$$

When the PRF is not high enough to sufficiently capture the Doppler signal bandwidth of interest, portions of this bandwidth are *aliased*. Fig 1.10 illustrates Doppler spectrum aliasing, where the black trace is the true Doppler spectrum which is repeated at intervals of the slow-time sampling frequency PRF. In this figure the Doppler spectrum bandwidth $B_{\text{d}} > PRF$, so portions of the spectrum bleed into adjacent zones. The blue dashed trace describes the actual observed

spectrum which is a combination of the overlapping repeated spectra, and the orange box denotes the nominal unambiguous interval. Within this nominal interval, aliasing is observed, where the edges of the true signal spectrum appear to wrap around to the other side of the interval.

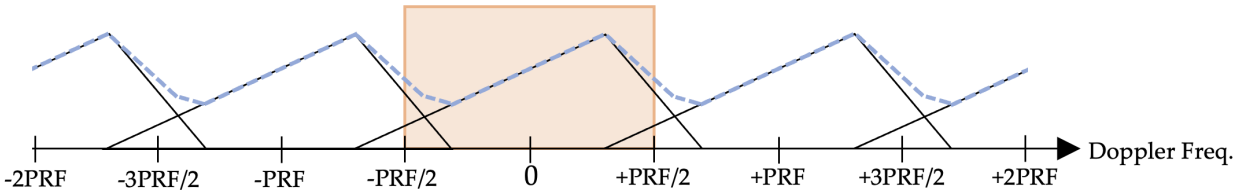

Figure 1.10: Visualization of Doppler spectrum aliasing showing repeated and overlapping Doppler spectrum (black trace), observed Doppler spectrum, which is the combination of the overlapping spectrum (blue trace), and the nominal unambiguous Doppler interval (orange box)

Thus a trade-off is introduced, where higher PRF allows for larger unaliased Doppler bandwidth, but results in a shorter range ambiguity.

1.5.3 PRF Regimes

Uniform PRF pulse radars are classified according to their PRFs into the following three categories [10]:

1) **Low PRF**, which can achieve precise and fine-resolution range measurements at the cost of ambiguous Doppler and higher peak power transmissions compared to the high PRF regime,

2) **Medium PRF**, which compromises on both range and Doppler ambiguities in an effort to achieve accurate performance in both dimensions, and

3) **High PRF**, which has a high unambiguous Doppler frequency with the trade-off of shorter range ambiguities and exacerbated pulse eclipsing effects.

In the next section a non-uniform Doppler sampling method is introduced which mitigates Doppler ambiguities, thereby working around the range/Doppler ambiguity tradespace while incurring associated costs.

1.6 PRI Staggering Motivation

Traditional MTI radar uses a uniform PRI, enabling the use of a uniform fast Fourier transform (FFT) [5, 10, 11, 13] for Doppler processing. This form of processing results in a Doppler response that repeats at intervals of the slow-time sampling frequency or PRF. To increase the unambiguous Doppler frequency, one could employ the use of higher PRFs, though range ambiguities could become problematic per the trade-space discussed in the previous section. An alternate solution involving modulation of the interpulse period, a technique called PRI or PRF staggering, provides an **expansion of unambiguous Doppler space by reducing aliasing of the Doppler spectrum** [6, 7, 10, 11, 13, 22, 23, 24], and the ability to resolve range ambiguities [10, 12, 13, 25, 26, 27, 28, 29] (translating to range swath increase which could mean less data for synthetic aperture radar (SAR) applications [10, 30]).

Staggering is a well known technique for achieving these goals, though usually in the context of alternation between predetermined PRF values where the staggering is imposed from CPI to CPI. This technique, commonly called *PRF staggering* is often used to resolve range ambiguities via modulus-based methods such as the Chinese Remainder Theorem, Coincidence Algorithm, or Clustering Algorithm [10, 12, 13, 25, 26, 27, 28, 29]. Variability is also imposed on a pulse-to-pulse basis [6, 8, 12, 31, 32, 33, 34, 35, 36, 37, 38, 39, 40, 41, 42, 43, 44, 45] , such that the benefits from staggering are observed from a single CPI, though with the trade-off of increased processing complexity since the uniform FFT is no longer viable for Doppler processing. This form of variation is referred to as *PRI staggering* and is illustrated in Fig. 1.11 for M pulses.

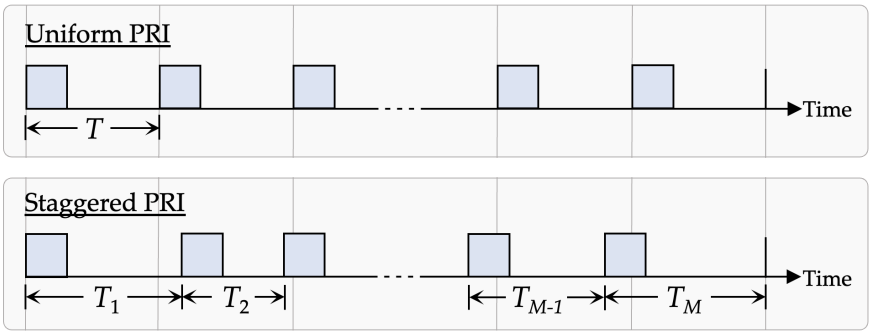

Figure 1.11: Visualization for a coherent processing interval containing uniform PRIs and staggered PRIs

Fig 1.12 shows the data matrix from Section 1.2.2.2 for PRI staggered data. After pulse-by-pulse range alignment, the staggering of the pulse interval is visually evident, with the grayed samples showing zero-padding to maintain L samples in each row. The green column denotes the first sample of each pulse and the pink column corresponds to the maximum unambiguous range for this staggering configuration. The unambiguous range swath is determined by the minimum PRI when using a staggered pulse arrangement.

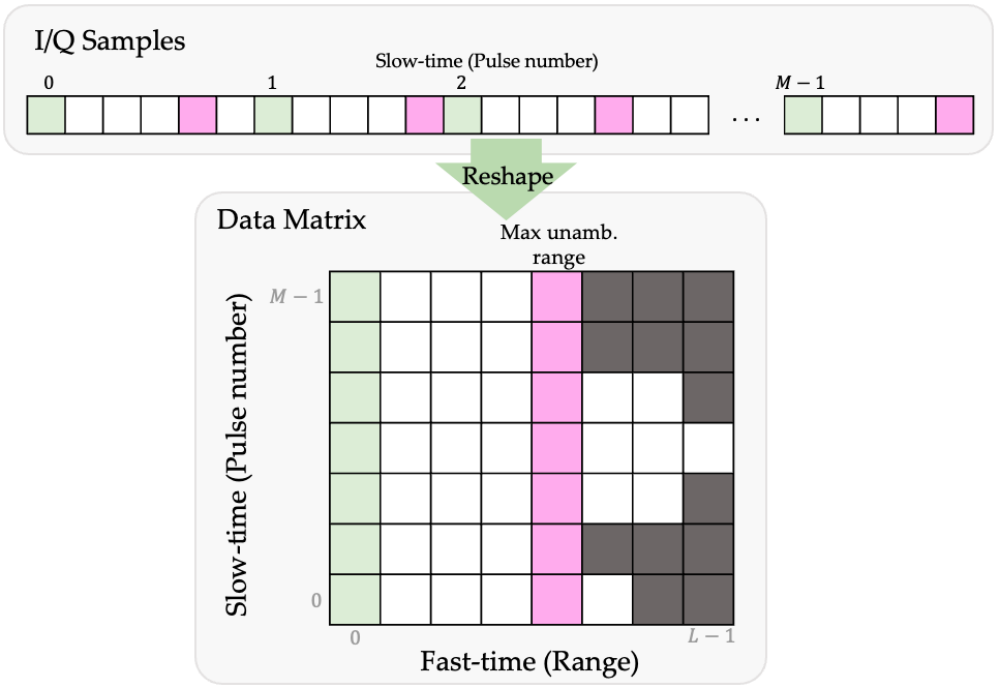

Figure 1.12: Staggered PRI data matrix

1.6.1 Random Staggering

PRI staggering can be categorized into the three following forms: static, in which interpulse times are taken from a finite set of values [12, 31, 32, 33], structured, for which PRIs exhibit a functional dependence on slow-time [8, 34, 35, 36], and random, where PRIs are independently and randomly selected [6, 37, 38, 39, 40, 41, 42, 43, 44, 45]. Using a staggered structure, the maximum unambiguous Doppler frequency is expanded by a factor that is determined by the least common multiple of the PRFs used [10]:

$$f_{\mathrm{D},max} = \frac{\mathrm{lcm}\left(\frac{1}{T_1}, ..., \frac{1}{T_M}\right)}{2}, \tag{1.24}$$

where $\mathrm{lcm}(\bullet)$ denotes the least common multiple of the arguments, T_m is the m^{th} PRI and recalling that PRF is the inverse of PRI. Based on this relationship, random PRI staggering can clearly offer additional benefits beyond those of static or structured forms due to the diversity inherent in the randomness. Random PRI staggering does incur a higher sidelobe pedestal and may exhibit large peaks that could mask lower power peaks from other moving objects, or result in false alarms. This thesis addresses this undesired quality of PRI staggering.

The following chapter develops a PRI staggering Doppler response model for two different random PRI sequence generation methods, and delves deeper into the behavior and characteristics of random PRI staggering. Chapter 3 then introduces the concept of a PRI stagger co-array, which is subsequently used to examine the effect of redundancy in the PRI sequence. Chapter 4 presents a gradient-based optimization to convert purely random PRI sequences into pseudo-random optimized PRI sequences that demonstrate significant sidelobe performance improvement, both in simulation and open-air experimental data. Chapter 5 concludes the thesis with prospects for future work.

Chapter 2

PRI Staggering Model

Two different methods of PRI generation/CPI construction based on random staggering of PRIs are delineated here, which both consider two requirements:

1) Bounded staggering to account for minimum PRI and

2) Fixed CPI extent to maintain nominal Doppler resolution.

The particular construction method makes a great deal of difference in the Doppler response and can affect design choices. This chapter first defines two different methods which will be called *cumulative staggering* and *grid staggering* (Section 2.1). Development of a model for the random PRI stagger receive signal and Doppler response is detailed, and the expected Doppler response for both generation methods are compared in Section 2.3.2.

2.1 Random PRI Generation Methods

2.1.1 Cumulative Stagger

First, consider the approach in [7] when each PRI is independently instantiated according to some distribution centered on an average value T_{avg}, then subsequently combined to form a full CPI. The m^{th} PRI is denoted as

$$T_{\text{c},m} = T_{\text{avg}} + \Delta T_{\text{c},m} \tag{2.1}$$

with the staggers $\Delta T_{c,m}$ for $m = 1,2,...,M$ drawn from a distribution bounded on $[-\delta,+\delta]$, thereby setting a limit on the minimum and maximum PRI. The subscript $(\bullet)_c$ stands for "cumulative", and will be used when the PRI generation method follows this model. For $m = 0$, the initial condition $\Delta T_{c,0} = T_{c,0} = 0$ is applied to ensure the CPI starts at the time instance $t_0 = 0$. A visualization of this particular model for random stagger generation is shown in Fig. 2.1.

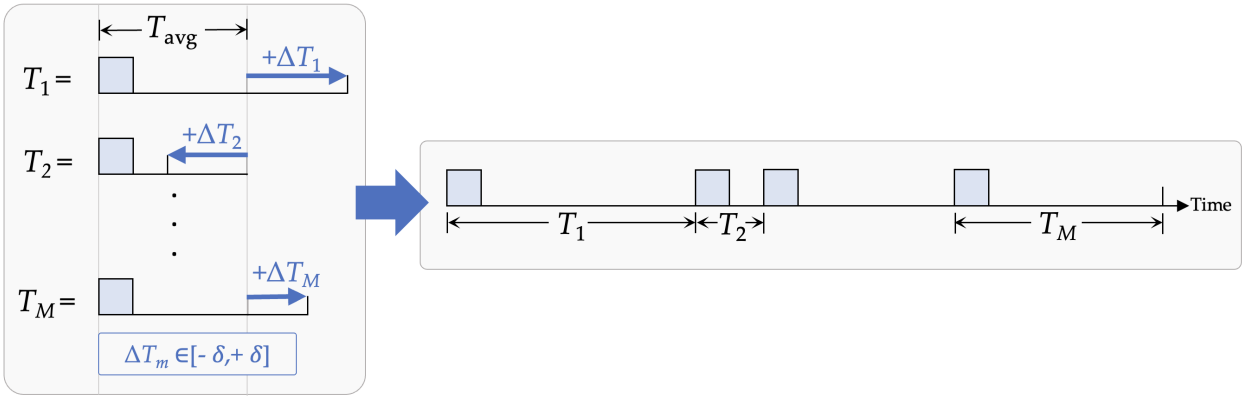

Figure 2.1: Visualization for generating random staggered PRI using the cumulative model where staggers are applied to the interpulse times

The accumulated slow-time at the onset of each pulse is

$$T_{c,acc}(m) = \sum_{q=0}^{m-1} T_{c,q} \tag{2.2}$$

for $m = 1,2,...,M$. The staggering is therefore also accumulated with the pulse progression, hence the moniker "cumulative". The average PRI is

$$T_{avg} = \frac{1}{M} \sum_{m=1}^{M} T_{c,m}. \tag{2.3}$$

This can also be thought of as the repeated PRI for the comparable uniform case. To enable generalization of staggering behavior, the PRI values are normalized by this average value as

$$\varepsilon_{c,m} = \frac{T_{c,m}}{T_{avg}} \tag{2.4}$$

so the total normalized CPI extent equals the number of pulses M. We now define a new, normalized staggering bound

$$\bar{\delta} = \frac{\delta}{T_{\text{avg}}} \tag{2.5}$$

which is expressed in terms of percentage. Thus $-\bar{\delta} \leq \Delta\varepsilon_{\text{c},m} \leq +\bar{\delta}$. Collecting the M PRI values from $m = 0, 1, ..., M-1$ into a vector, we have

$$\boldsymbol{\varepsilon}_{\text{c}} = [0 \quad \mathbf{1}^T_{(M-1)\times 1}]^T + [0 \quad \Delta\varepsilon_{\text{c},1} \quad \dots \quad \Delta\varepsilon_{\text{c},M-1}]^T \tag{2.6}$$

$$= [0 \quad \mathbf{1}^T_{(M-1)\times 1}]^T + \boldsymbol{\Delta\varepsilon}_{\text{c}} \tag{2.7}$$

where $\mathbf{1}_{(M-1)\times 1}$ is a ones a vector. Note that if the vector collecting the stagger terms $\boldsymbol{\Delta\varepsilon}_{\text{c}}$ is a zeros vector, then $\boldsymbol{\varepsilon}_{\text{c}}$ becomes the uniform PRI case. $\Delta\boldsymbol{\varepsilon}_{\text{c}}$ is now an optimizable parameter set. Let the normalized accumulated slow time be denoted as

$$\varepsilon_{\text{c,acc}}(m) = \sum_{q=0}^{m-1} \varepsilon_{\text{c},q}, \tag{2.8}$$

which can be written in vector notation as

$$\boldsymbol{\varepsilon}_{\text{c,acc}} = \mathbf{B}\boldsymbol{\varepsilon}_{\text{c}}, \tag{2.9}$$

where $\mathbf{B}$ is a lower triangular matrix which performs a cumulative sum across $\boldsymbol{\varepsilon}_{\text{c}}$.

2.1.1.1 CPI Scaling

At this point it is important to note that when generating the staggers in this manner, a fixed CPI extent of M cannot be expected. This aspect is explored in [9]. In order to have an accurate comparison between sequences, we must maintain a fixed CPI length (and thereby Doppler resolution via Eq. 1.13). This can be done by scaling the PRIs (note that pulse width should remain

unchanged), subsequently dilating or contracting the entire CPI to maintain a length of M. Thus the PRIs cannot be expected to uphold the design boundary of $\varepsilon_m \in [1-\bar{\delta}, 1+\bar{\delta}]$. Two extreme examples are presented to demonstrate the worst-case scenarios of dilation and contraction.

Consider the corner case where $M-1$ of the PRIs are the maximum value $\varepsilon_{c,m} = 1+\bar{\delta}$ and the remaining PRI the minimum $\varepsilon_{c,\bar{m}} = 1-\bar{\delta}$. This presents a scenario where upon CPI scaling, the maximum contraction occurs while there exists a PRI already at the minimum design boundary. This case results in the practical minimum bound on a single PRI that could arise from this staggering formulation. An example is shown in Fig. 2.2. Conversely, consider the case where the maximum degree of CPI dilation occurs, where all but one of the PRIs fall on $\varepsilon_{c,m} = 1-\bar{\delta}$ and one has the maximum $\varepsilon_{c,\bar{m}} = 1+\bar{\delta}$. Dilation of this largest PRI results in the practical maximum bound. For these two cases, the CPI would need to be scaled by factor

$$\frac{M}{\big((M-1)(1\pm\bar{\delta})+(1\mp\bar{\delta})\big)} = \frac{M}{\big(M\pm(M-1)\bar{\delta}\mp\bar{\delta}\big)} \approx \frac{1}{1\pm\bar{\delta}} \tag{2.10}$$

when M is large. This produces the scaled bounds

$$\varepsilon_{c,\bar{m},\text{scale}} \approx \frac{(1\mp\bar{\delta})}{(1\pm\bar{\delta})}. \tag{2.11}$$

These bounds are plotted as a function of $\bar{\delta}$ in Fig. 2.3 using solid lines. Also shown are the design boundaries given by $1\pm\bar{\delta}$ (long dashed lines) and the longest/shortest PRIs over a set of 1000 scaled random cumulative staggered PRIs for $M = 100$ pulses (short dashed lines). Observe that while the practical boundaries due to the most extreme dilation/contraction is quite severe, in actuality the worst case only violates the design boundaries by a small amount.

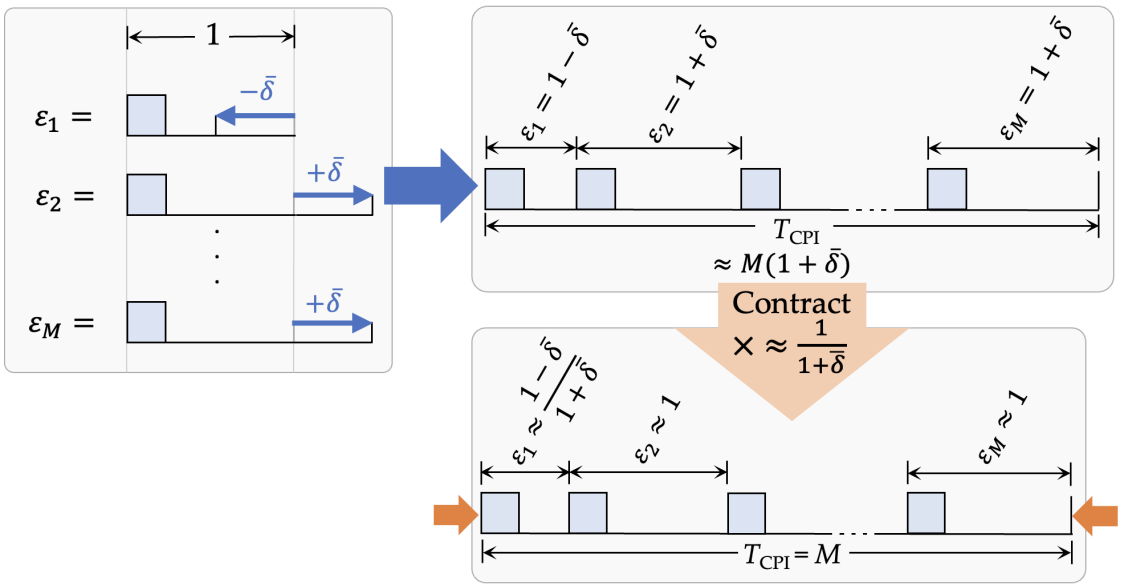

Figure 2.2: Example of smallest possible PRI due to fixing CPI extent

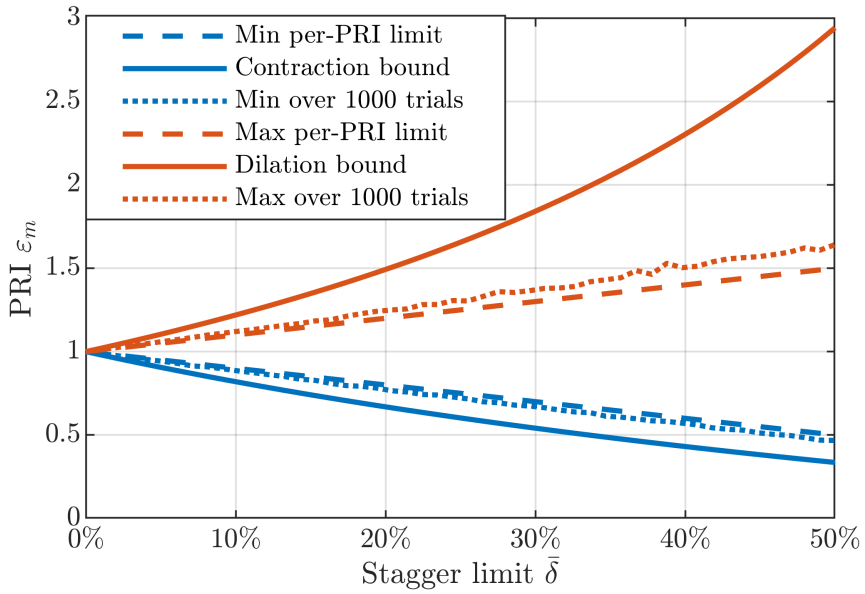

Figure 2.3: Minimum/Maximum PRI over 1000 trials of $M = 100$ pulse CPIs after scaling, compared with design per-PRI limit and minimum/maximum per-PRI boundary due to scaling

Fig. 2.4 further describes this effect via a histogram of 10^5 scaled cumulative staggered PRIs. The dashed line denotes the distribution on which the PRIs lie before scaling. Only a small tail is observed on each side, demonstrating that while the PRIs do happen to violate the design boundaries occasionally, it is rare and only by a small amount.

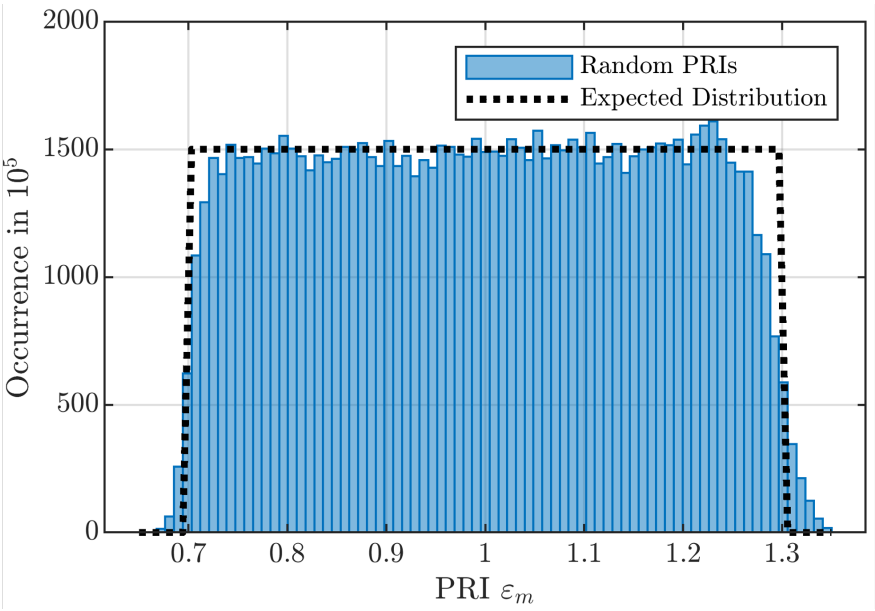

Figure 2.4: Histogram of randomly generated and scaled PRIs for 1000 trials of $M = 100$ pulses and $\bar{\delta} = 30\%$

Due to the shrunken PRIs, the contraction case could result in issues with blind ranges and shorter range ambiguities that would need to be contended with using more sophisticated processing. Based on the aggregate results in Figs. 2.3 and 2.4, contraction tends to produce minimum PRIs similar to the design limit. Conversely, dilation of the CPI results in a contraction of the Doppler response, which could be problematic in the optimization context in Chapter 4, by pulling an unoptimized section of the Doppler response into the span of interest thereby impacting sidelobe performance. This can be easily accounted for by including an additional optimized buffer zone as is discussed later in Section 2.2.3.2.

The cumulative stagger model discussed in this section provides a high level of PRI diversity since each PRI is independently generated, and the diversity has a cumulative effect. However a potential pitfall is the violation of minimum PRI requirements due to contraction for preserving a fixed CPI. This section demonstrated that such a pitfall is a rare occurrence.

2.1.2 Grid Stagger

Now consider another stagger generation approach that naturally achieves a fixed CPI. Here it is called the "grid stagger" model. With this approach staggering is performed *after* the PRIs are already placed in a uniform CPI, where the staggers are then applied directly to the *boundaries between* PRIs. In short, it is the grid of uniform pulse onset times that is staggered. The accumulated slow-time is

$$T_{\mathrm{g,acc}}(m) = mT_{\mathrm{avg}} + \Delta T_{\mathrm{g},m} \tag{2.12}$$

for $m = 1,2,...,M$, the same T_{avg} as in Eq. 2.3, the endpoints $\Delta T_{\mathrm{g},0} = \Delta T_{\mathrm{g},M} = 0$, and the rest of the staggers $\Delta T_{\mathrm{g},m}$ for $m = 1,2,...,M-1$ drawn from a distribution on $[-\delta/2, +\delta/2]$ so that the stagger limit remains δ. Here the subscript $(\bullet)_{\mathrm{g}}$ is used to specify grid staggered PRIs. Fig 2.5 shows an example of this arrangement.

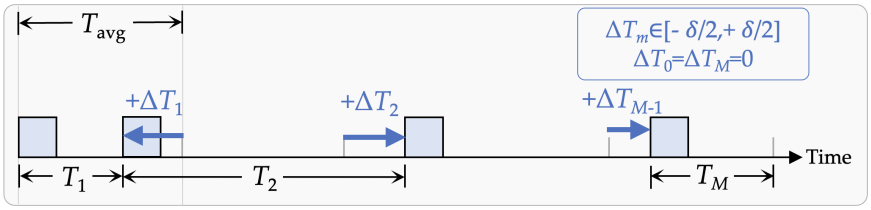

Figure 2.5: Visualization for generating random staggered PRI using the grid model where staggers are applied to a uniform grid of pulses

Since the endpoints of the CPI are always fixed with this approach, CPI scaling is not necessary, contrary to the cumulative model presented in the previous section. The design boundary on the minimum PRI is therefore not violated.

The m^{th} PRI is affected by two independent perturbations as

$$T_{\mathrm{g},m} = T_{\mathrm{avg}} + \Delta T_{\mathrm{g},m} - \Delta T_{\mathrm{g},m-1} \tag{2.13}$$

Again, division by Eq. 2.3 produces the time-normalized PRIs:

$$\varepsilon_{\mathrm{g},m} = \frac{T_{\mathrm{g},m}}{T_{\mathrm{avg}}}, \tag{2.14}$$

and the vector that collects the normalized PRIs is

$$\begin{aligned} \boldsymbol{\varepsilon}_{\mathrm{g}} &= [\varepsilon_{\mathrm{g},0} \quad \varepsilon_{\mathrm{g},1} \quad \dots \quad \varepsilon_{\mathrm{g},M-1}] && (2.15)\\ &= [0 \quad \mathbf{1}^T_{(M-1)\times 1}]^T + [0 \quad \Delta\varepsilon_{\mathrm{g},1} \quad \dots \quad \Delta\varepsilon_{\mathrm{g},M-1}]^T && (2.16)\\ &\quad - [0 \quad \Delta\varepsilon_{\mathrm{g},0} \quad \dots \quad \Delta\varepsilon_{\mathrm{g},M-2}]^T, && (2.17) \end{aligned}$$

recalling that $\Delta\varepsilon_{\mathrm{g},0} = 0$, and the normalized stagger values lie on $[-\bar{\delta}/2, +\bar{\delta}/2]$ for $\bar{\delta}$ the normalized stagger limit from Eq. 2.5. The normalized pulse onset times are then the same accumulated slow-time as in Eq. 2.8, but are defined directly via the stagger values as

$$\begin{aligned} \boldsymbol{\varepsilon}_{\mathrm{g,acc}} &= [0 \quad 1 \quad \dots \quad M-1]^T + [\Delta\varepsilon_{\mathrm{g},0} \quad \Delta\varepsilon_{\mathrm{g},1} \quad \dots \quad \Delta\varepsilon_{\mathrm{g},M-1}]^T && (2.18)\\ &= [0 \quad 1 \quad \dots \quad M-1]^T + \boldsymbol{\Delta\varepsilon}_{\mathrm{g}}. && (2.19) \end{aligned}$$

Two different random stagger construction models have now been presented. Perfomance differences between the two models are explored in Section 2.3.2. Because much of the subsequent modelling of the Doppler response is the same for both, the discussion in the following few sections is agnostic to the particular construction method. For formulations that are specific to either the cumulative or grid model, the respective labels $(\bullet)_{\mathrm{c}}$ and $(\bullet)_{\mathrm{g}}$ are used to denote this specificity.

2.2 Receive Signal Model and Non-uniform Discrete Fourier Transform (NUDFT)

2.2.1 Doppler-Dependent Phase Response

In Eq. 1.10, the slow-time receive signal for a uniform PRI system was given. Switching consideration to a staggered PRI scheme, the phase (disregarding amplitude) at the m^{th} slow-time

instance due to a moving scatterer in the illuminated scene is

$$v_m(f_{\mathrm{nD}}) = \exp\{j2\pi f_{\mathrm{nD}}\varepsilon_{\mathrm{acc}}(m)\} \tag{2.20}$$

$$= \exp\left\{j2\pi f_{\mathrm{nD}}\mathbf{b}_m^T\boldsymbol{\varepsilon}\right\}, \tag{2.21}$$

where $\exp\{\bullet\}$ denotes elementwise exponentiation,

$$\mathbf{b}_m = [\mathbf{1}_{(m)\times 1}^T \quad \mathbf{0}_{(M-m)\times 1}^T] \tag{2.22}$$

(the m^{th} row of matrix $\mathbf{B}$ from Eq. 2.9) performs a sum over the 0 through $(m-1)^{th}$ elements of $\boldsymbol{\varepsilon}$, $\mathbf{0}_{(M-m)\times 1}^T$ is vector of zeros, and f_{nD} is the normalized Doppler frequency

$$f_{\mathrm{nD}} = 2T_{\mathrm{avg}}\frac{v_{\mathrm{rad}}}{\lambda} \tag{2.23}$$

for λ the operating wavelength and v_{rad} the specific radial velocity of the mover relative to the radar. Extending Eq. 2.20 to the full CPI, the phase progression across slow-time, which is equal to the $M \times 1$ Doppler steering vector is

$$\mathbf{v}(f_{\mathrm{nD}}) = \exp\{j2\pi\mathbf{B}\boldsymbol{\varepsilon}f_{\mathrm{nD}}\} \tag{2.24}$$

where again $\mathbf{B}$ is a lower triangular matrix which, when applied as $\mathbf{B}\boldsymbol{\varepsilon}$, produces the accumulated time sequence $\boldsymbol{\varepsilon}_{\mathrm{acc}}$.

2.2.2 Receive Signal Model

The receive signal model for Doppler processing comprised of beamforming, pulse compression, and in-phase/quadrature (I/Q) sampling is given in [7] as

$$\mathbf{z}(\ell) = \sum_{f_{\text{nD}}} x(\ell; f_{\text{nD}})\mathbf{v}(f_{\text{nD}}) + \mathbf{n}(\ell) \tag{2.25}$$

$$\approx \mathbf{V}\mathbf{x}(\ell) + \mathbf{n}(\ell), \tag{2.26}$$

where $x(\ell; f_{\text{nD}})$ is the scattering in the ℓ^{th} range bin that corresponds to the normalized Doppler shift f_{nD}, and $\mathbf{n}(\ell)$ is an $M \times 1$ noise vector. The approximation in the second line comes about due to a discretization of the continuous model in the first line. $\mathbf{V}$ is a matrix containing the Doppler steering vectors from Eq. 2.24, with Doppler frequency equally spaced on a prescribed interval.

2.2.3 Non-uniform Discrete Fourier Transform (NUDFT)

The matrix $\mathbf{V}$ is a non-uniform discrete Fourier transform (NUDFT) matrix containing the N Doppler steering vectors from Eq. 2.24 and is compactly represented as

$$\mathbf{V} = \exp\left\{ j2\pi \mathbf{B}\boldsymbol{\varepsilon}\mathbf{f}_{\text{nD}}^{T} \right\}. \tag{2.27}$$

with $\mathbf{f}_{\text{nD}}$ containing the N normalized Doppler frequencies.

2.2.3.1 Discretization

The nominal discretization would be M equally spaced Doppler bins on the normalized interval $f_{\text{nD}} \in [-1/2, +1/2]$. Including oversampling by a factor K for visibility and extending to the full desired Doppler span $[-\beta/2, +\beta/2]$, the discretized Doppler axis contains $N = \lceil \beta KM \rceil$ points for $\lceil \bullet \rceil$ the ceiling operation. If $\lceil \beta KM \rceil$ is even, it is convenient to set $N = \lceil \beta KM \rceil + 1$ in order to include zero-Doppler.

2.2.3.2 Doppler Expansion Factor

The factor β, which describes the unambiguous Doppler interval that results from the least common multiple of the normalized PRFs (i.e. a normalized version of Eq. 1.24), may be unnecessarily large and could even exceed Doppler frequencies corresponding to speeds greater than physically possible. It is therefore sufficient, as suggested in [7], to set a practical limit β_{mov} that encompasses the fastest radial movement expected, so that the Doppler interval of interest lies on $[-\beta_{\text{mov}}/2, +\beta_{\text{mov}}/2]$. In the context of stagger sequence optimization, in order to provide a flat sidelobe response over this entire interval the optimization in Chapter 4 must be performed over a larger span, since a mover existing at the edge of this interval would have a sidelobe response at the opposite edge. It is therefore necessary to achieve a desired sidelobe response for an expansion factor of $\beta_{\text{opt}} = 2\beta_{\text{mov}}$. Furthermore, the Doppler response should be optimized for an additional extent to compensate for a possible contraction after CPI-fixing (discussed in Section 2.1.1.1). To account for the worst case scenario of CPI contraction, the optimization should be performed over $\beta_{\text{opt}}(1+\bar{\delta})$.

2.3 Doppler Response

2.3.1 Zero-referenced Doppler Response Model

Since the Doppler response is shift-invariant, the zero-referenced response is generalizable to non-zero Doppler shifts. Therefore consideration is limited to the $N \times 1$ zero-referenced, discretized, and gain normalized Doppler response

$$\mathbf{u}(\boldsymbol{\varepsilon}) = \frac{1}{M}\mathbf{V}^H\mathbf{v}_0 \tag{2.28}$$

for $\mathbf{v}_0$ the zero-Doppler steering vector (from Eq. 2.24 when $f_{\text{nD}} = 0$) which is equivalently an $M \times 1$ ones vector, and $(\bullet)^H$ the Hermitian operation. The values $\boldsymbol{\varepsilon}$ lie on a continuum, and each element of $\mathbf{u}(\boldsymbol{\varepsilon})$ is a continuous function of the given parameters, so a gradient may be determined

for use in the optimization procedure detailed in Chapter 4.

2.3.2 Expected and Aggregate Doppler Response

2.3.2.1 Expectations

Expected Response for Cumulative Staggering The expectation of the magnitude-squared of the Doppler response in Eq. 2.28 for the cumulative model described in Section 2.1.1 is derived in [7] for $\Delta\boldsymbol{\varepsilon}$ on the uniform distribution $[-\bar{\delta}, \bar{\delta}]$. The closed-form solution is:

$$E\left[|u_{\mathrm{c}}(f_{\mathrm{nD}})|^2\right] = \frac{1}{M} + \frac{2}{M^2}\sum_{m=1}^{M-1}\left(m\cos\left(2\pi f_{\mathrm{nD}}(M-m)\right) \times \left[\mathrm{sinc}(2\pi f_{\mathrm{nD}}\bar{\delta})\right]^{(M-m)}\right), \tag{2.29}$$

which is a function of the number of pulses M and the stagger limit $\bar{\delta}$. This functional relationship of $u_{\mathrm{c}}(f_{\mathrm{nD}})$ on M is shown in Fig. 2.6. Note that here the mainlobe width decreases according to the inverse relationship between Doppler resolution and CPI extent from Eq. 1.13, since here responses are compared for the same average PRI. The expected sidelobe structures produced by differing M possess the same general shape albeit with varying pedestal levels at $-10\log_{10}(M)$ dB.

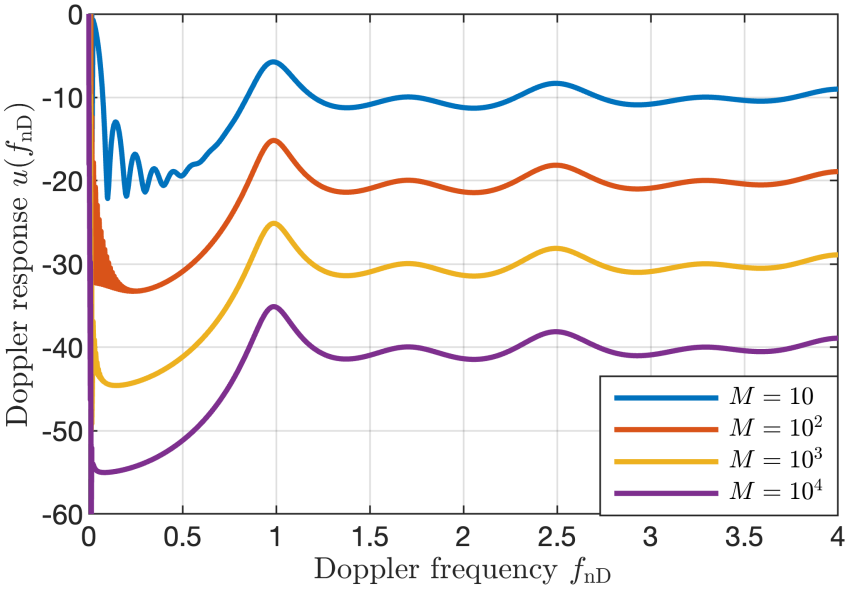

Figure 2.6: Expectation of Doppler response using cumulative staggering model for different number of pulses M and $\bar{\delta} = \pm 30\%$

The expected Doppler response exhibits a ripple about a value determined by M, but the nature of this rippling varies with stagger limit $\bar{\delta}$. As $\bar{\delta}$ is increased, the degree of ripple in the Doppler response decreases, shown in Fig. 2.7. Larger staggers provide more variation thereby contributing to a flattened Doppler response, the result of a phase-decoherence phenomenon that is explored in Section 2.3.3. Since the traces for $\pm 30\%$ and $\pm 40\%$ staggering display a similar degree of flatness, and because larger stagger limit $\bar{\delta}$ contributes to a shortened range ambiguity, the choice of $\bar{\delta} = \pm 30\%$ for the cumulative staggering method is adequate to achieve the available diversity granted by random staggering.

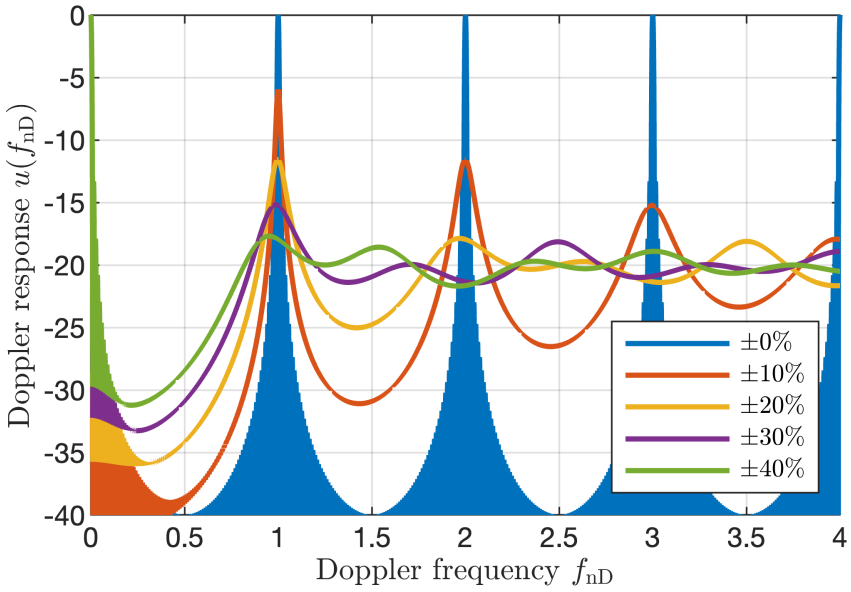

Figure 2.7: Expectation of Doppler response for different limits $\bar{\delta}$ on random cumulative staggering and $M = 100$ pulses

Though the expected responses in Fig. 2.7 may suggest that simply increasing the stagger limit yields a smooth and flat Doppler response, a single instance with $\bar{\delta} = 30\%$ shown in Fig. 2.8 demonstrates the unpredictability of random staggering. The single instance (blue trace) does indeed flatten the response compared to the uniform case, but sidelobe peaks are uncontrolled and could result in false alarms in a subsequent detection stage of the radar. From this perspective of unpredictability, it is clearly desirable to produce optimized sequences for which Doppler sidelobes are flattened to reduce the probability of false alarms.

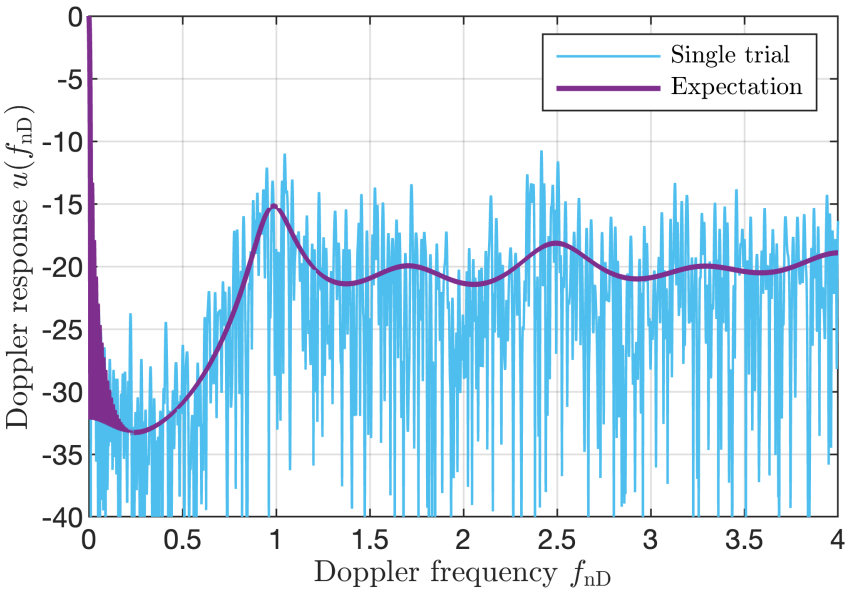

Figure 2.8: Single instantiation of random cumulative staggering for $\bar{\delta} = \pm 30\%$ limits and $M = 100$ pulses compared to expectation, illustrating Doppler sidelobe variation

Expected Response for Grid Staggering The expected Doppler response for the grid staggering model is derived in Appendix A, leveraging the derivation for the cumulative staggering model found in [7]. It is likewise a function of the number of pulses M and the stagger amount $\bar{\delta}$ as

$$E\left[\left|u_{\mathrm{g}}(f_{\mathrm{nD}})\right|^2\right] = \frac{1}{M} + 2\left(\frac{\mathrm{sinc}(\pi f_{\mathrm{nD}}\bar{\delta})}{M}\right)^2 \times \sum_{m=1}^{M-1} m\cos\left(2\pi f_{\mathrm{nD}}(M-m)\right). \tag{2.30}$$

Similar to the expected response for cumulative staggering, the average sidelobe level is related to the number of pulses M by $-10\log_{10}(M)$ dB, a relationship shown in Fig 2.9.

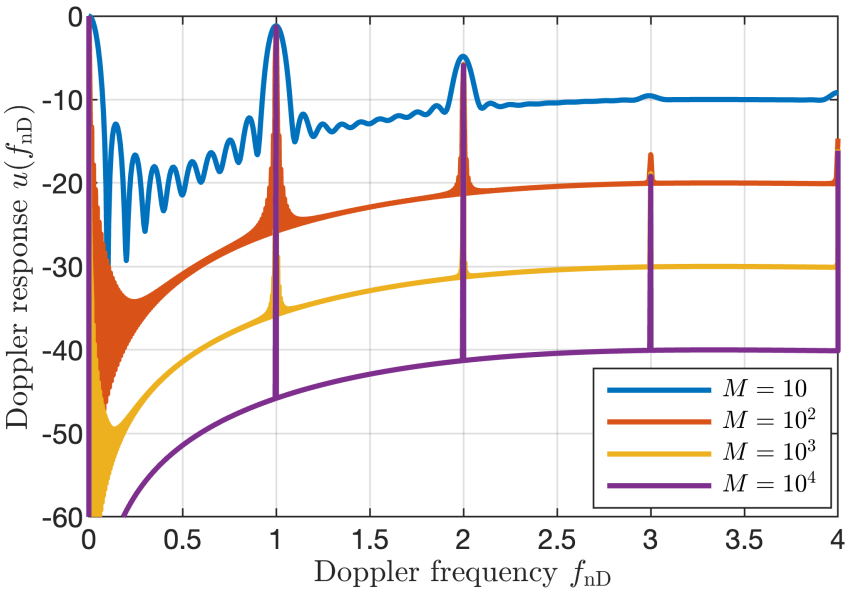

Figure 2.9: Expectation of Doppler response using grid staggering model for different number of pulses M and $\bar{\delta} = \pm 30\%$

The grid model produces an expected response that contains significantly less fluctuation compared to the cumulative model, though at the cost of sharp peaks that resemble the uniform PRI Doppler response. By increasing M, these peak levels are slightly decreased for $f_{\mathrm{nD}} \geq 2$, though the peak at $f_{\mathrm{nD}} = 1$ is not changed with varied M.

Figs. 2.10 and 2.11 shows increasing $\bar{\delta}$ results in decreasing peaks (this result was separated into two figures for visibility). The responses for $\bar{\delta} \leq 40\%$ are large and would appear similar to the Doppler spectrum aliasing experienced by uniform PRI. Thus, for the grid staggering model, $\bar{\delta} \geq 40\%$ should be used to mitigate repeated Doppler ambiguities, though two "quasi-ambiguities" corresponding to the high peaks on either side of the mainlobe at $f_{\mathrm{nD}} = \pm 1$ remain. Around $\bar{\delta} = 80\%$, ambiguity at $f_{\mathrm{nD}} = \pm 1$ becomes suppressed enough to be masked by random sidelobe fluctuations, shown in Fig. 2.12. Due to the larger required stagger limit compared to the cumulative model, grid staggering incurs heavier range swath loss compared to the cumulative model.

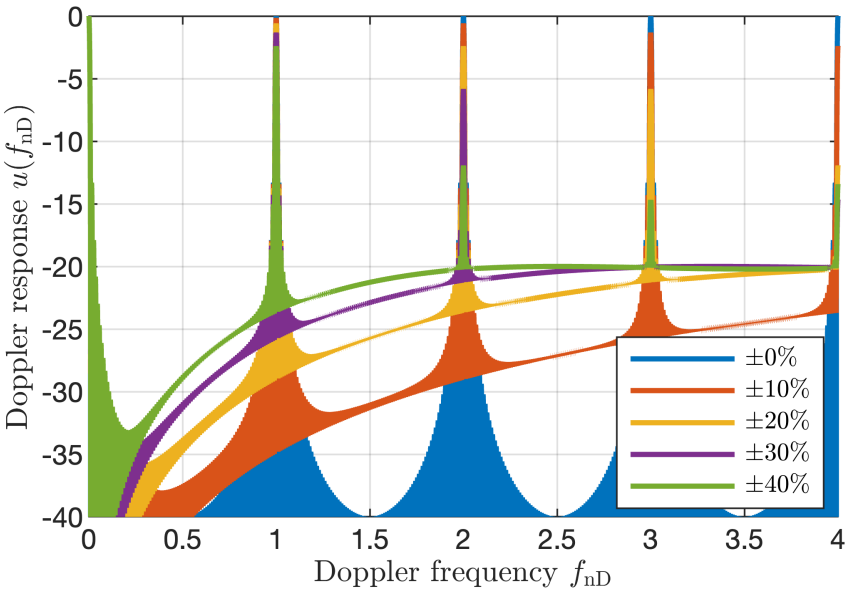

Figure 2.10: Expectation of Doppler response for stagger limits $\bar{\delta}$ from 0% to 40% on random grid staggering and $M = 100$ pulses

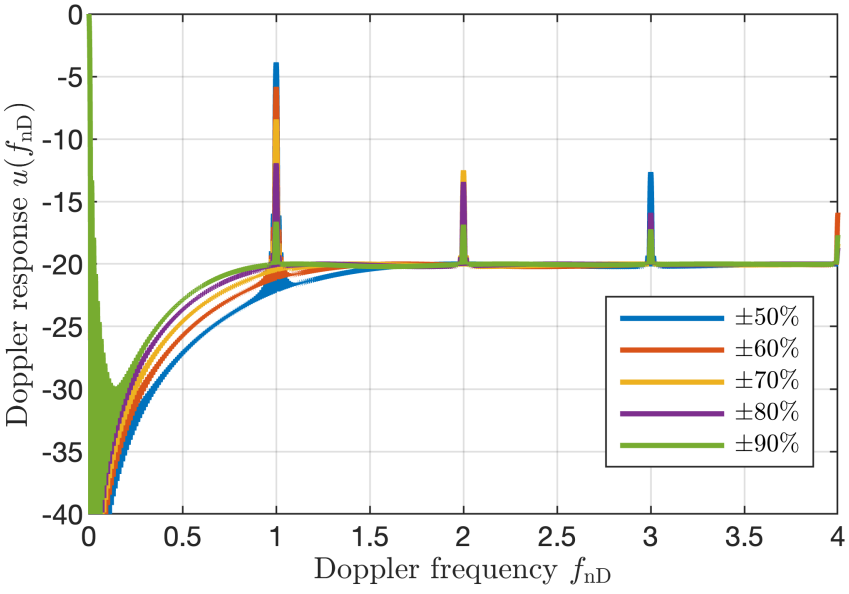

Figure 2.11: Expectation of Doppler response for stagger limits $\bar{\delta}$ from 50% to 90% on random grid staggering and $M = 100$ pulses

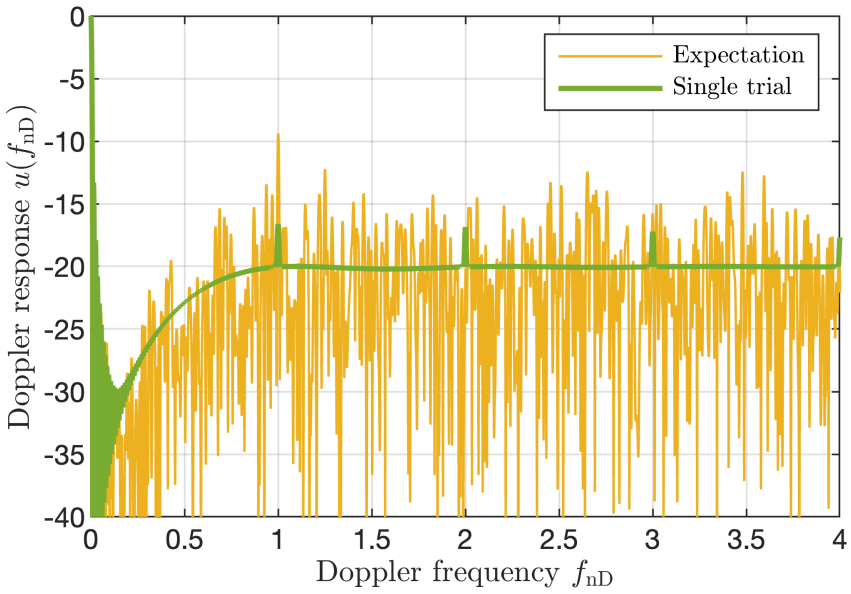

Figure 2.12: Single instantiation of random grid staggering for $\bar{\delta} = \pm 80\%$ limits and $M = 100$ compared to expectation

2.3.2.2 Aggregated Response Comparison

1000 trials of random PRI generation were performed according to the two models from Section 2.1 using $M = 100$ pulses. The maximum across the trials at each Doppler frequency f_{nD}, and the root-mean-square (RMS) average of these trials are presented in Fig. 2.13 for varying degrees of staggering. Fig. 2.13 demonstrates that higher available staggering diversity allows for better mitigation of Doppler ambiguities. Larger $\bar{\delta}$ provide more diversity than smaller $\bar{\delta}$, and the cumulative staggering model provides more diversity over the grid staggering model. For $\bar{\delta} = 10\%$, the sidelobe peak at $f_{\mathrm{nD}} = 1$ remains poorly suppressed for both random staggering models. However as $\bar{\delta}$ increases, cumulative staggering clearly presents a dramatic maximum sidelobe suppression benefit over the grid staggering model.

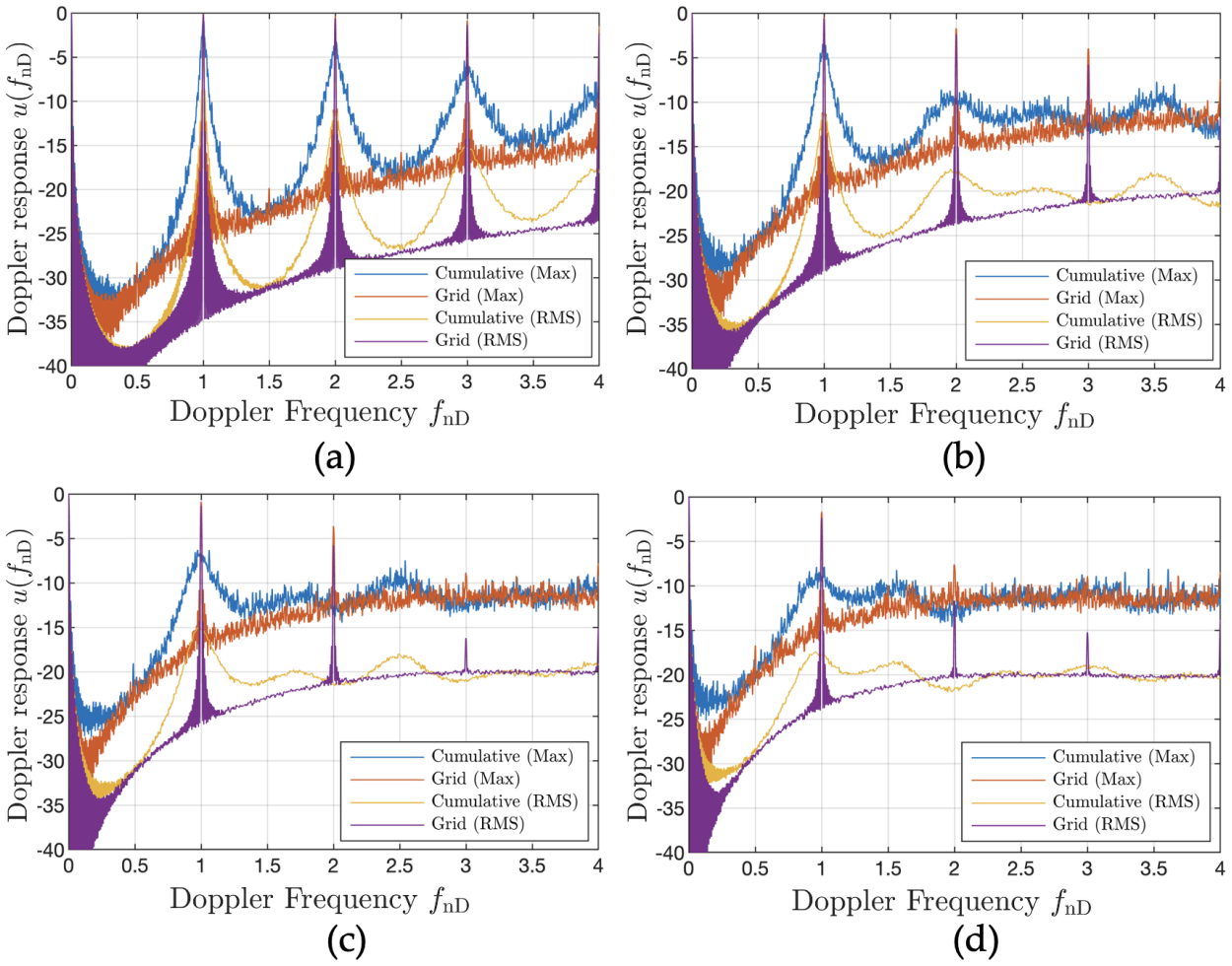

Figure 2.13: Max and RMS Doppler response over 1000 random staggering trials comparing average performance between the cumulative and grid models for **(a)** $\bar{\delta} = \pm 10\%$, **(b)** $\bar{\delta} = \pm 20\%$, **(c)** $\bar{\delta} = \pm 30\%$, and **(d)** $\bar{\delta} = \pm 40\%$,

The maximum curves are consistently about 7-8 dB higher than their associated average curves, signifying that high sidelobe peaks always remain a possibility when using purely random instantiations of PRI staggering. In the next chapters, design approaches for mitigating these sidelobe peaks are presented.

2.3.3 Phase-Doppler Frequency Fan Plots

Discussed in Section 1.3.3, Doppler processing realizes a form of coherent integration across the pulses, so it makes intuitive sense that phase-decoherence is the mechanism behind the flattened

sidelobe response granted by staggering. In this section, the Doppler-phase "fan plot" from [7] is used as a visual tool to help build intuition for the phase-decoherence phenomenon that results in Doppler ambiguity suppression, and the two random staggering models from the previous section are compared in this context. Recall the slow-time signal from Eq. 2.20

$$v_m(f_{\mathrm{nD}}) = \exp\{j2\pi f_{\mathrm{nD}}\varepsilon_{\mathrm{acc}}(m)\},$$

for f_{nD} the normalized Doppler frequency and $\varepsilon_{\mathrm{acc}}(m)$ the accumulated normalized slow-time at the m^{th} pulse for $m = 0, 1, ...M-1$. Thus the Doppler-rate-of-change of the phase progression for the m^{th} pulse is

$$\frac{\Delta\phi(m, f_{\mathrm{nD}})}{\Delta f_{\mathrm{nD}}} = 2\pi\varepsilon_{\mathrm{acc}}(m). \tag{2.31}$$

For the uniform case, the Doppler-phase slopes are simply $2\pi m$ for $m = 0, 1, ...M-1$. The phase $\phi(f_{\mathrm{nD}})$ for the first 7 pulses of a uniform PRI arrangement are plotted in Fig. 2.14 as a function of normalized Doppler frequency, resembling a fan shape. Vertical black lines are placed at integer values of f_{nD}, where it can be seen that all of the phases align with an integer multiple of 2π. The coherence aspect is more visible in the provided wrapped phase plots. All of the pulses cohere at these Doppler frequencies, corresponding to repeated Doppler response mainlobes, also shown in the figure.

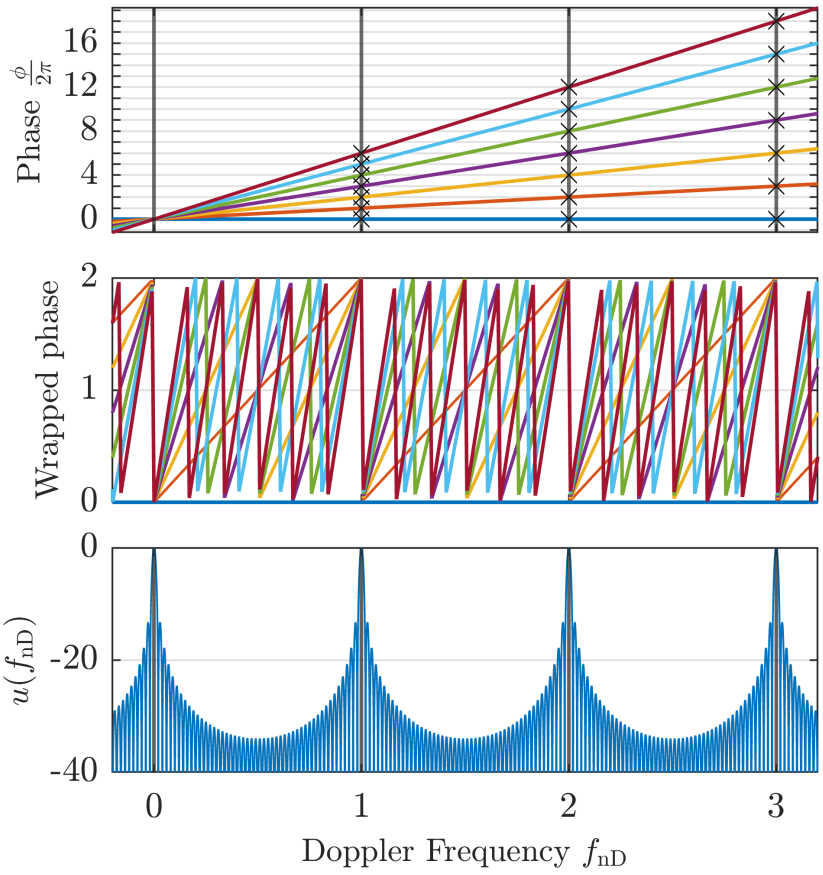

Figure 2.14: Phase-Frequency fan plot of the first 7 pulses for uniform PRI, wrapped phase for visibility, and associated Doppler response with $M = 50$ pulses

Now consider a static staggering formulation, where the PRI values alternate between the two values $\varepsilon_m = 1/3, 1$. According to Eq. 1.24, this results in a Doppler mainlobe repetition at $f_{\mathrm{nD}} = \mathrm{lcm}(\frac{1}{1/3}, 1) = 3$. Indeed, Fig. 2.15 shows that this is the case, but reveals more to the story. The solid vertical lines indicate where perfect coherence across all M pulses occurs (shown by the exes), but partial coherence may occur as well, denoted by the dashed vertical lines. At these frequencies, the phase values remain close to integer multiples of 2π.

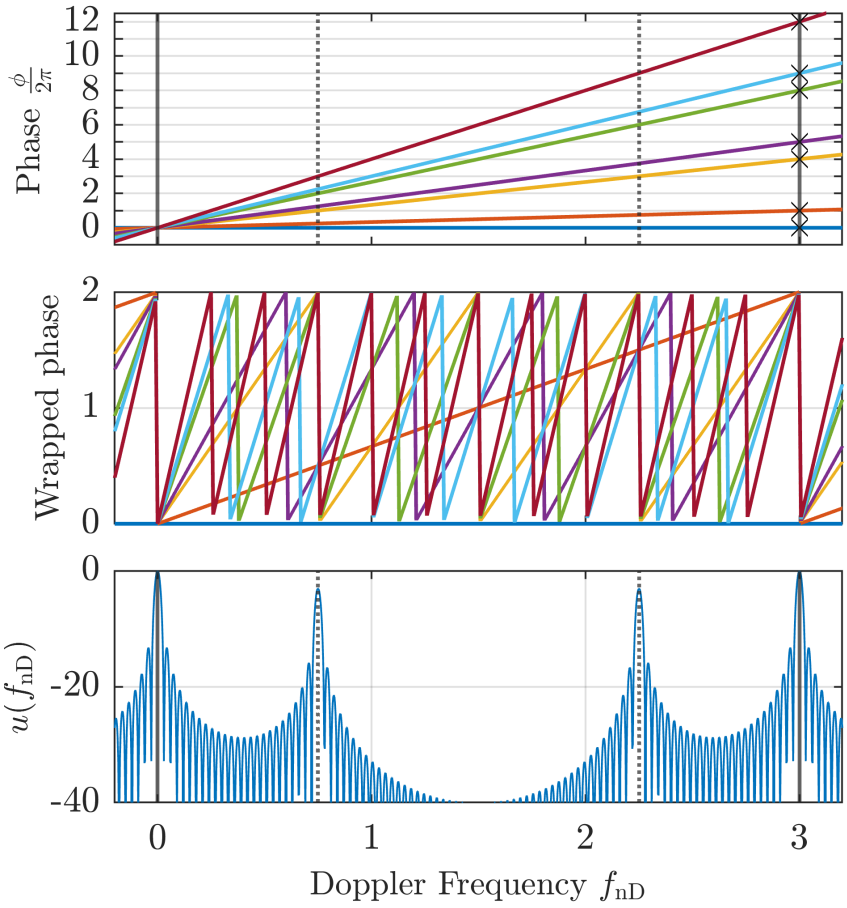

Figure 2.15: Phase-Frequency fan plot of the first 7 pulses for static PRI (alternation between $T = 1/3$ and 1), wrapped phase for visibility, and Doppler response with $M = 50$ pulses

Next, the effect of random staggering is explored through the lens of the fan plot. The concept of "phase slope deflection" produced by staggering is represented in Figs. 2.16 and 2.17, where the same stagger value $\Delta\varepsilon$ is applied to the $m = 1,2,3$ pulses using the cumulative model (Fig. 2.16) and the grid model (Fig. 2.17), respectively. For the cumulative model, the phase slope deflections are accumulated so that the slope for the m^{th} pulse is given by

$$\frac{\Delta\phi_{\mathrm{c}}(m, f_{\mathrm{nD}})}{\Delta f_{\mathrm{nD}}} = 2\pi(m + m\Delta\varepsilon). \tag{2.32}$$

In contrast, the grid model applies staggering directly to these phase slope deflections and the slope

for the m^{th} pulse is

$$\frac{\Delta\phi_{\text{g}}(m, f_{\text{nD}})}{\Delta f_{\text{nD}}} = 2\pi(m + \Delta\varepsilon). \tag{2.33}$$

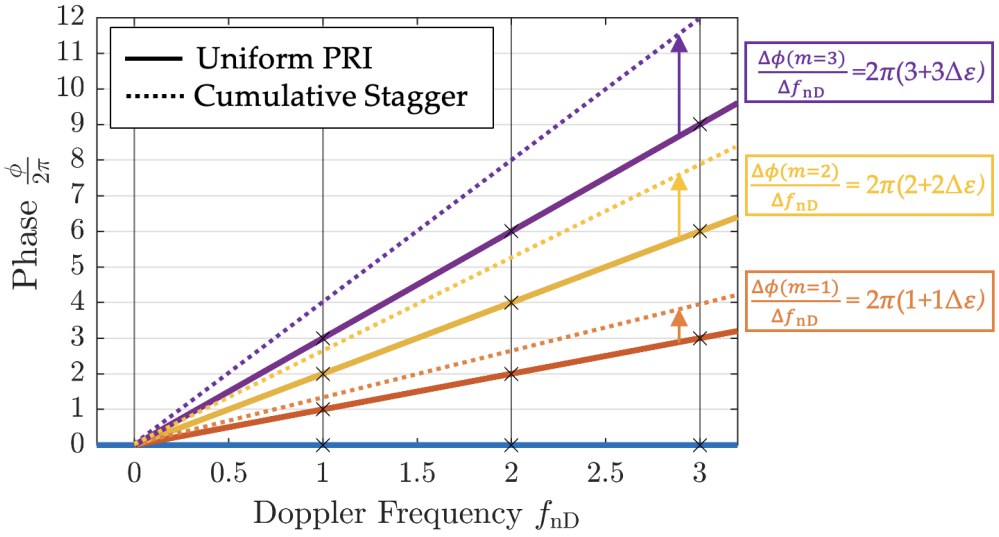

Figure 2.16: Phase-Frequency slope deflection visualization for cumulative staggering

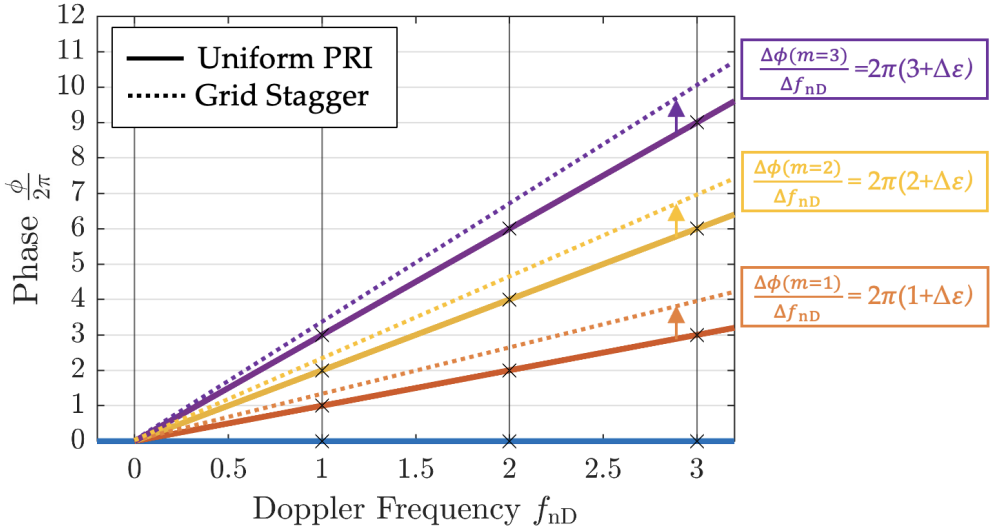

Figure 2.17: Phase-Frequency slope deflection visualization for grid staggering

Clearly as m increases, cumulative staggering can achieve higher degrees of phase slope deviation from the uniform PRI structure than the grid model can grant.

Now the intuition behind the greater diversity afforded by cumulative staggering compared to grid staggering has been built. For completeness, fan plots for a low diversity case with $\bar{\delta} = \pm 10\%$ as well as a high diversity case with $\bar{\delta} = \pm 40\%$ for cumulative staggering and $\bar{\delta} = \pm 10\%, \pm 80\%$ for grid staggering are shown in Figs. 2.18-2.19. These plots demonstrate that higher diversity, presented by either cumulative staggering or increased stagger limit, results in a flatter Doppler sidelobe response, and that phase coherence or partial coherence depicted by the fan plot is the mechanism behind Doppler sidelobe perfomance.

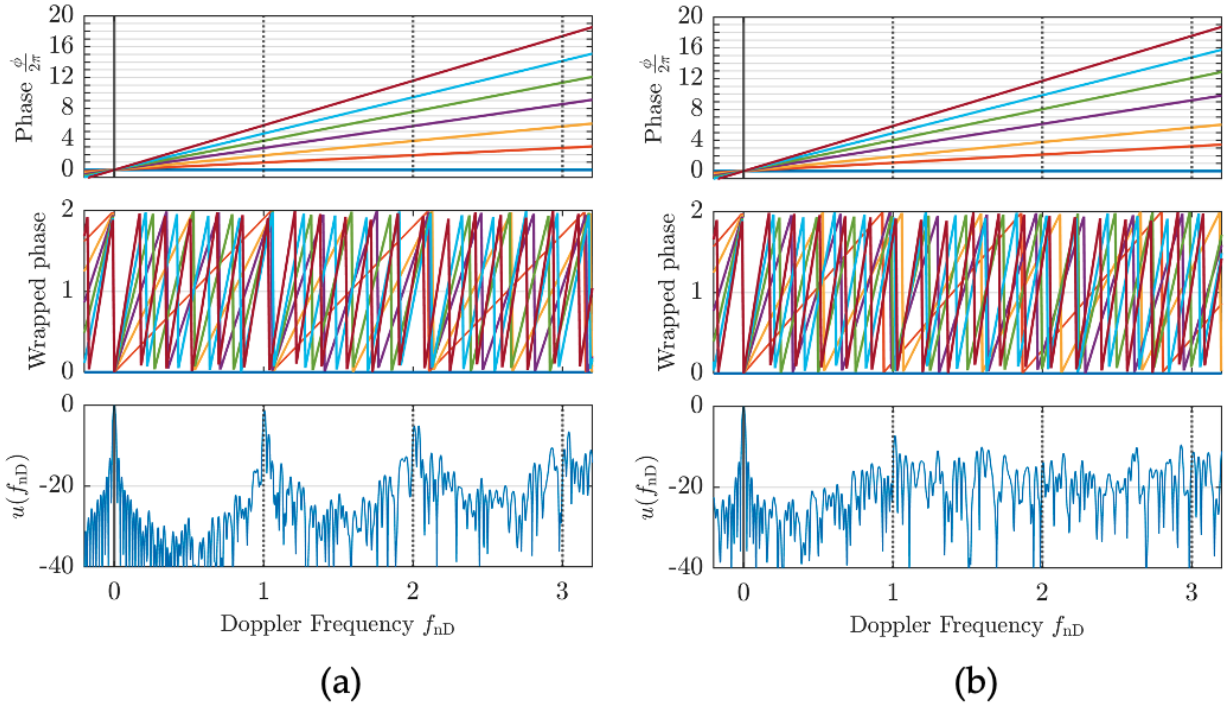

Figure 2.18: Phase-Frequency fan plot, wrapped phase, and Doppler response for cumulative staggering with $M = 50$ pulses and **(a)** $\pm 10\%$ **(b)** $\pm 40\%$

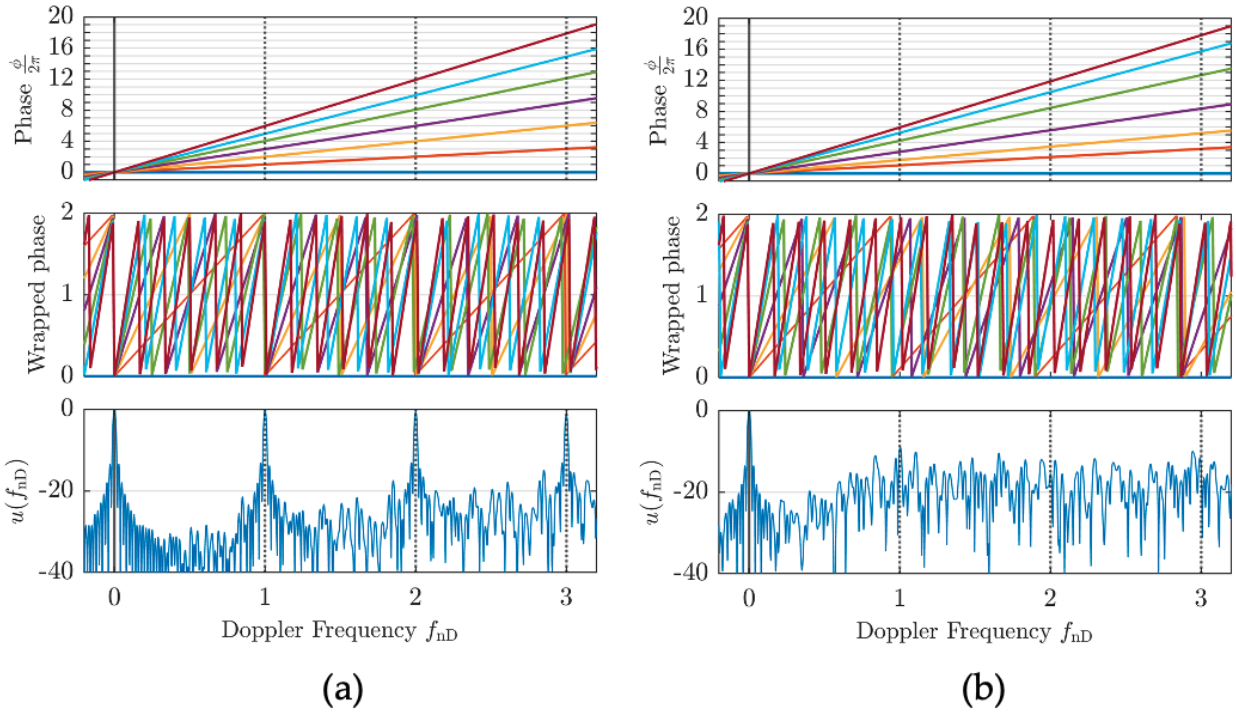

Figure 2.19: Phase-Frequency fan plot, wrapped phase, and Doppler response for grid staggering with $M = 50$ pulses and **(a)** $\pm 10\%$ **(b)** $\pm 80\%$

Chapter 3

Redundancy and the PRI Staggering Co-Array

3.1 The Sparse Array/PRI Staggering Analogy

There is a well-known structural similarity between the phase models for antenna arrays (spatial) and a CPI of pulses (slow-time, Eq. 2.20). Non-uniformity in both domains achieves a similar flattening of the power spectrum, though the purpose of the non-uniformity is different for the two cases, leading to some **key distinctions**:

1. **What is kept fixed:** For PRI staggering, the overall dwell time is kept fixed, whereas for sparse arrays it is the minimum spacing between elements ($\lambda/2$).

2. **What is expanded:** PRI staggering yields an expansion of the unambiguous Doppler span, while staggering allows for an expanded antenna aperture, thereby granting better spatial resolution for the same number of elements.

3. **Observation limit:** The physical observation angle for an antenna array spans $[-90°, +90°]$, which is hard limited by electromagnetic constraints. If power is pushed outside of this "real-space" limit, it encroaches on the "invisible-space" [46] , which could result in transmitter damage. In contrast, the observable Doppler frequency span is hard-limited by the speed of light. Since realistically a radar system would not need to observe movers at that speed, the Doppler frequency is more soft-limited by high radial speeds where the "stop-and-hop" model (Section 1.3.2) for Doppler breaks down. Since appropriate compensation on receive may be applied to address this, there is effectively no limit for Doppler frequency.

Because of these distinctions, the solutions to non-uniform design tend to be different between the two domains, which is explored later in this chapter. Even so, the mathematical tools used for analysis and design can be interchanged. Previous work exploring the analogy between non-uniform time/spatial sampling includes [47] , which uses the sparse array design technique Marginal Fisher's Information (MFI) [48] to optimize fast-time sampling for signal reconstruction. In [49] , the co-prime antenna structure is used to produce a PRI staggering arrangement for CPI combination in processing.

This chapter expands upon previous work in [8] , where the co-array concept widely used in sparse array design [50] is leveraged to analyze staggered PRI sequence structure with the goal of aiding PRI staggering design. The effect of redundancy in PRI staggering is explored, and uniqueness between redundant sequences is analyzed.

3.2 PRI Staggering Co-array

In this section, the concept of the PRI staggering co-array is developed, which largely resembles the co-array for antenna array design. First, consider the CPI containing staggered PRIs as a set of impulses denoting the pulse onset locations on a temporal aperture, described by the accumulated normalized slow-time in Eq. 2.8. This CPI containing impulses at the pulse onset times (and zero-valued intervals in between) is denoted as $w(\boldsymbol{\varepsilon}_{\text{acc}})$. An example of this arrangement is shown in Fig. 3.1.

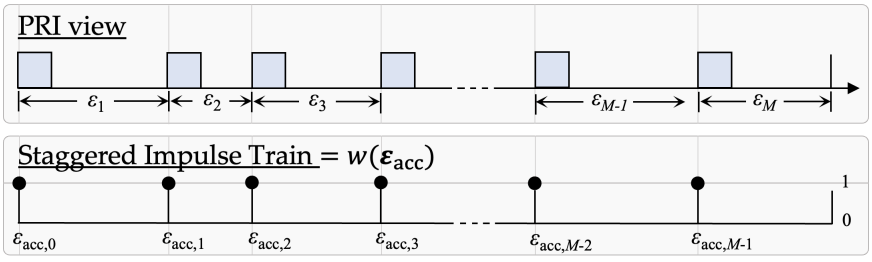

Figure 3.1: CPI translated into impulse train denoting pulse onset times

Denote the $MK \times 1$ discretization of $w(\boldsymbol{\varepsilon}_{\text{acc}})$ as $\mathbf{w}$, where M is again the number of pulses and K is an oversampling factor that sets the granularity of the discretized grid. K is also the number

of samples corresponding to T_{avg} in the discretized CPI. The PRI staggering co-array is then

$$c(\ell) = \sum_{n} w(n)w(n-\ell), \tag{3.1}$$

which is an autocorrelation of the CPI containing the pulse onset locations. The co-array depicts the degree of redundancy in the sequence. The staggered impulse train from Fig. 3.1 for a uniform PRI sequence with $M = 20$ and $K = 2000$ is compared to a randomly staggered PRI sequence in Fig. 3.2. The ensuing stagger co-arrays from Eq. 3.1 are shown in Fig. 3.3. Since it is symmetric, only one side of the co-array is displayed.

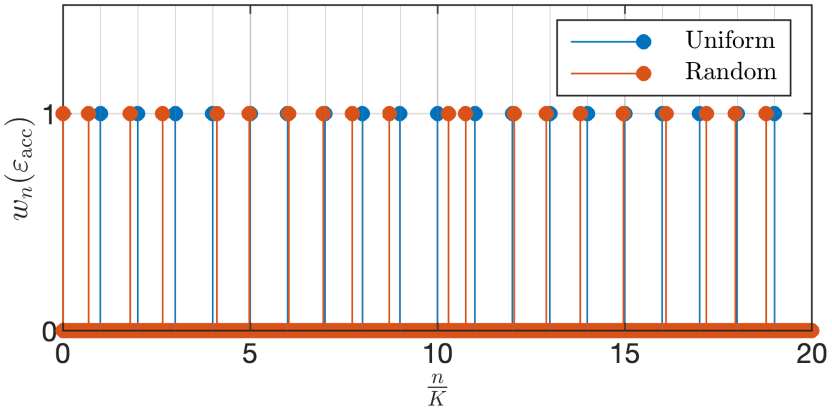

Figure 3.2: Single random instantiation impulse train compared to uniform for $M = 20$ pulses

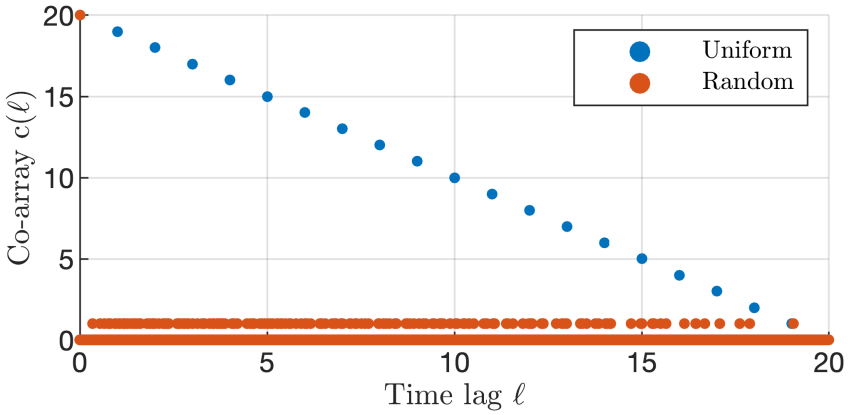

Figure 3.3: Coarray for random stagger using grid model achieves low redundancy compared to uniform PRI case for $M = 20$ pulses

The co-array displays the number of redundancies at each value of lag ℓ. For uniform PRI, the co-array (blue) in Fig. 3.3 exhibits the familiar peak of M at $\ell = 0$ and linear taper to 1 at $\ell = M - 1$. The grid staggered co-array (orange) demonstrates that the staggering shown in Fig. 3.2 corresponds to an almost complete elimination of redundancy in the PRI sequence, indicating that the random stagger instantiation naturally realizes a minimally redundant co-array since K is set sufficiently high for fine granularity. Note that for smaller K, the grid on which the PRIs are discretized becomes coarser, thereby introducing more possibility for redundancy. Therefore the factor K can be used as a "tuning knob" to control the level of redundancy in a generated random PRI sequence.

Conveniently, the Doppler power spectrum in Eq. 2.28 is a Fourier transform (FT) pair with Eq. 3.1, so that a fast Fourier Transform (FFT) can be used to observe the Doppler response despite the nonuniformity of the PRI sequence. The FFT is more computationally efficient than the Discrete Fourier Transform (DFT) ($O(N\log(N))$ compared to $O(N^2)$). Fig. 3.4 shows the corresponding Doppler response for the co-arrays in Fig. 3.3 to demonstrate the random PRIs' realization of the anticipated Doppler spectrum sidelobe flattening.

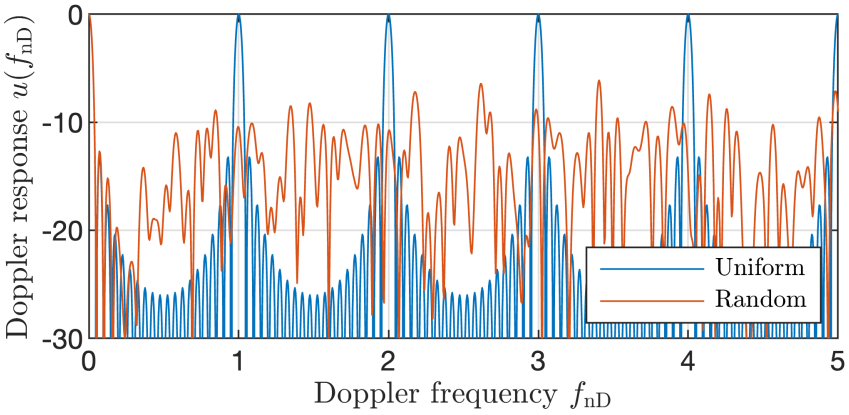

Figure 3.4: Doppler response for random stagger using grid model compared to uniform PRI.

Here the co-array does not consider the transmit waveform. Each pulse is depicted as an impulse with no time extent, so a single sample of lag results in complete decoherence. Later, when uniqueness between sequences is addressed in Section 3.4, the waveform is accounted for, result-

ing in a co-array consisting of scaled pulse compression responses. As discussed in the mentioned section, the pulse compression response mainlobe resolution is likely negligible compared to interpulse times, so ignoring this aspect for now does not affect the ensuing analysis.

3.3 Redundancy and the Doppler Response

The PRI staggering co-array from [8] was defined in the previous section and was demonstrated to be a useful tool for analyzing redundancy in PRI sequences. In this section the effect of redundancy on the Doppler spectrum response, specifically on the peak Doppler sidelobe, is explored, in the context of both cumulative and grid staggering.

The co-arrays for the same random grid stagger instantiation ($\bar{\delta} = 90\%$), discretized according to two different redundancy factors $K = 5$ and $K = 25$ are shown in Fig. 3.5, as well as their associated Doppler responses in Fig. 3.6. The same comparisons for the cumulative model (with $\bar{\delta} = 30\%$) are made in Figs. 3.7 and 3.8.

A coarser grid corresponds to a raised co-array level and steeper roll-off, indicating higher levels of redundancy. Clearly the different discretization granularities have affected the response structure, with higher co-array redundancy likewise translating to more redundancy in the Doppler response, displayed in the higher frequency of repeated mainlobes. The Doppler response repeats at intervals of K. The required value for K is then dependent on the required maximum unambiguous Doppler frequency as

$$K_{\text{req}} = 2f_{\text{nD}}. \tag{3.2}$$

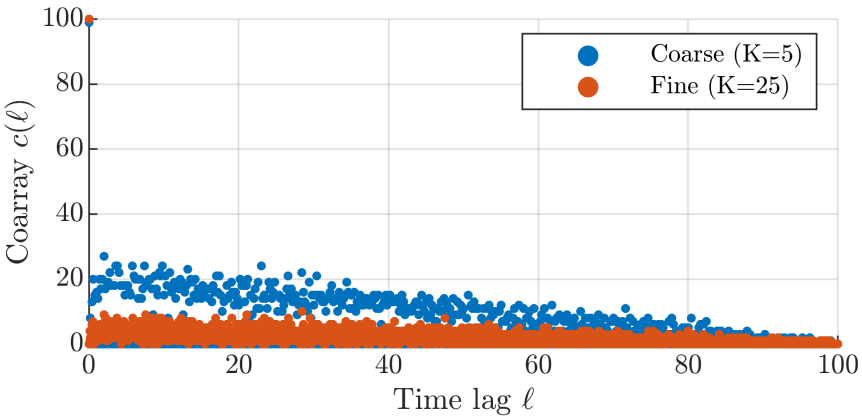

Figure 3.5: Coarray for random stagger using grid model with $\bar{\delta} = 90\%$ for two different levels of redundancy controlled by granularity factor K.

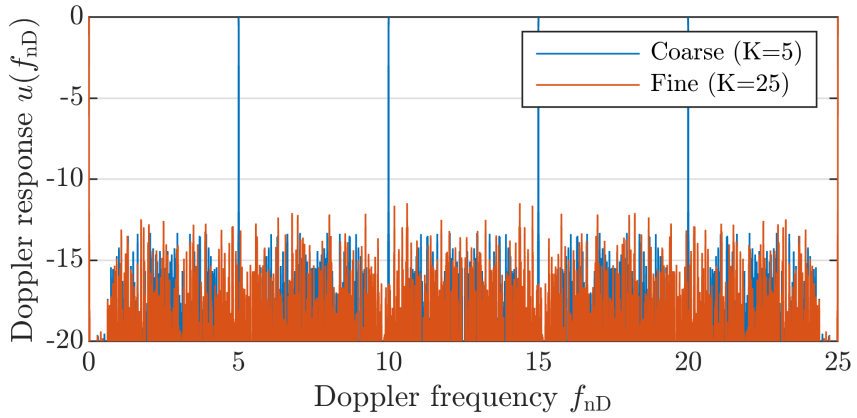

Figure 3.6: Doppler response for random stagger using grid model with $\bar{\delta} = 90\%$ for two different levels of redundancy controlled by granularity factor K.

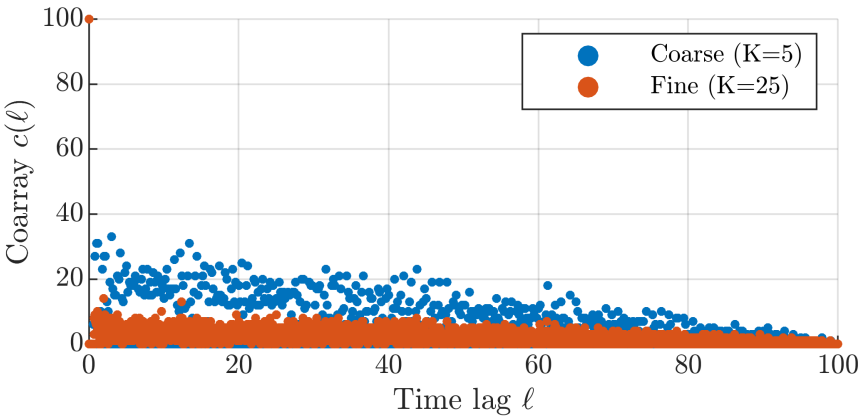

Figure 3.7: Coarray for random stagger using cumulative model with $\bar{\delta} = 30\%$ for two different levels of redundancy controlled by granularity factor K.

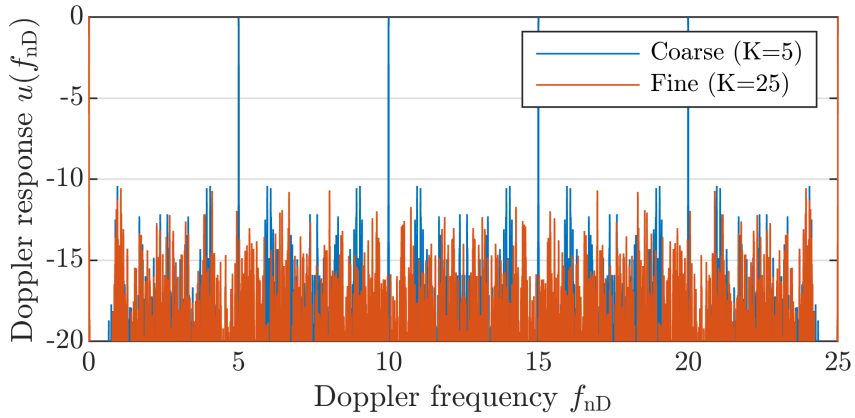

Figure 3.8: Doppler response for random stagger using cumulative model with $\bar{\delta} = 30\%$ for two different levels of redundancy controlled by granularity factor K.

3.3.1 Peak Doppler Sidelobe Level

The peak Doppler sidelobe level (PDSL) is a useful metric for the application of designing flat PRI stagger Doppler spectrums. PDSL is formally defined in terms of a p-norm in Section 4.3.2.1 to analyze optimization performance. Here it is used in conjunction with the PRI staggering co-

array to evaluate the effect of redundancy on the Doppler response. PDSL is defined as

$$\text{PDSL} = \frac{\max\limits_{f_{\text{nD}}} |\mathbf{w}_{\text{sl}} \odot \mathbf{u}|^2}{\max\limits_{f_{\text{nD}}} |\mathbf{w}_{\text{ml}} \odot \mathbf{u}|^2}, \tag{3.3}$$

where $\mathbf{w}_{\text{sl}}$ and $\mathbf{w}_{\text{ml}}$ are vectors containing ones and zeros that select for the sidelobes and mainlobe respectively, $\odot$ denotes a Hadamard product, $\mathbf{u}$ is a discretized version of the Doppler response in Eq. 2.28, and $\max\limits_{f_{\text{nD}}}(\bullet)$ denotes the maximum operation for all normalized Doppler.

3.3.2 Average PDSL Behavior with Stagger Limit

The effect of redundancy on the PDSL varies with stagger limit $\bar{\delta}$. To demonstrate this relationship, 10^4 Monte Carlo trials were performed for varying $\bar{\delta}$ for both the grid staggering and cumulative staggering models. The findings are detailed in the following sections.

3.3.2.1 Redundancy and Grid Staggering

10^4 grid stagger instantiations ($M = 100$) were discretized according to $K = 5$ and $K = 25$. This was performed for various $\bar{\delta}$, the PDSL was evaluated, and the aggregate results are shown in Fig. 3.9. The interval $[1/M, 5 - 1/M]$ was chosen for sidelobe selection because it encompasses the full span of the unambiguous sidelobe region for the high redundancy case ($K = 5$). The same interval was used to compute the PDSL for the fine grid (low redundancy) case. Thus the following analysis considers whether high or low redundancy is beneficial for the design interval $[1/M, 5 - 1/M]$, ignoring behavior outside this region.

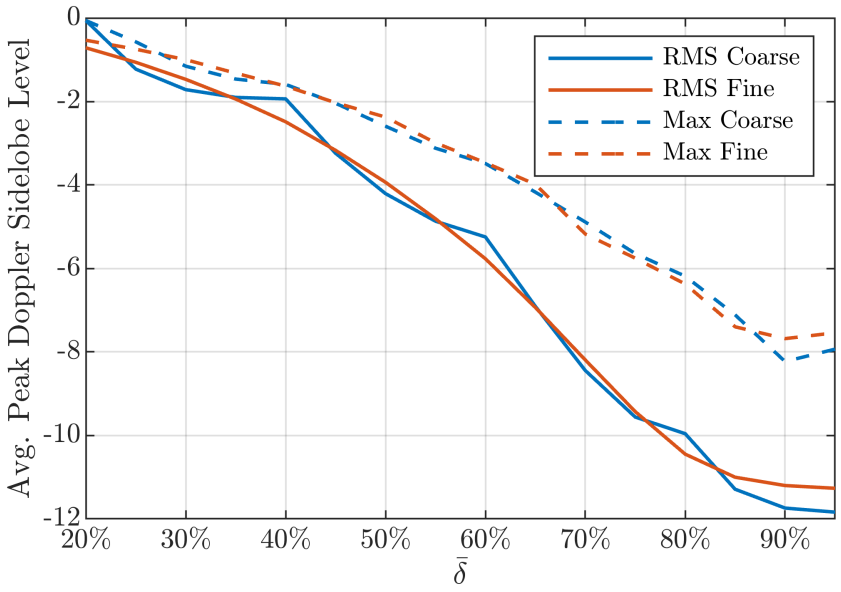

Figure 3.9: Average PDSL for 10^4 random trials of $M = 100$ pulse random grid staggered PRIs with varying $\bar{\delta}$ compared for $K = 5$ (Coarse) and $K = 25$ (Fine)

Fig. 3.9 for grid staggering shows that coarse and fine sequences possess similar maximum PDSL over the 10^4 trials, indicating that in this regard neither formulation presents a large advantage over the other, though for $\bar{\delta} > 85\%$, coarse grid staggering displays a slight decrease in maximum PDSL. The average PDSL trend for coarse grid staggering displays a strange "scalloped" behavior, which intersects the coarse trend line for fine grid staggering (which is smoother). This suggests that depending on the available staggering limit, one may choose either high or low redundancy arrangements for purely random grid staggering to provide a better chance for lower sidelobes. Histograms of 10^5 random trials are shown in Fig. 3.10 for both $K = 5$ and $K = 25$ at $\bar{\delta} = 90\%$ that provide a more detailed view.

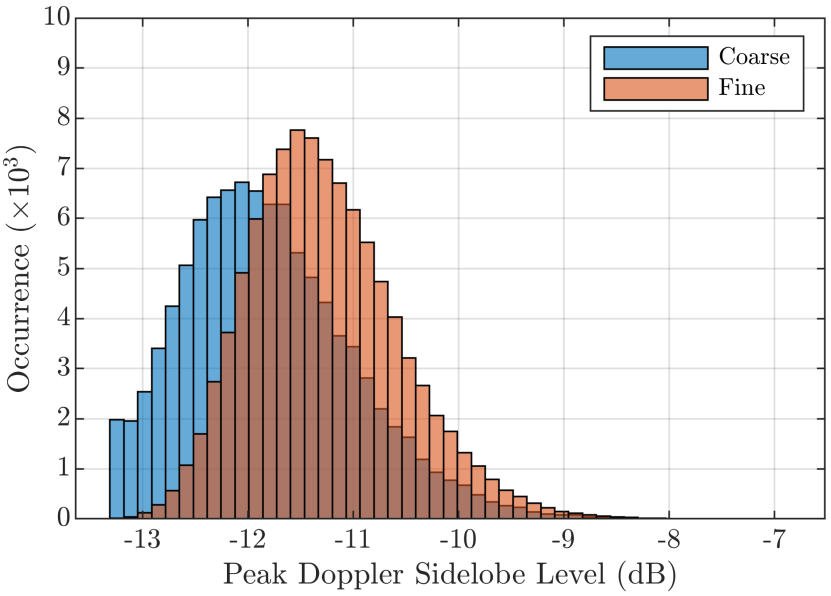

Figure 3.10: Histograms of peak Doppler sidelobe level for 10^5 random trials of $M = 100$ pulse random grid staggered PRIs with $\bar{\delta} = 90\%$.

Coarse grid staggering at $\bar{\delta} = 90\%$ was shown in Fig. 3.9 to provide improvement in both average and maximum PDSL compared to the fine grid staggering case. The histograms in Fig. 3.10 confirm that coarse grid staggering does indeed produce a down-shifted PDSL distribution, with the maximum PDSL improved by $(-7.1) - (-7.3) = 0.2$ dB, minimum PDSL improved by $(-13.3) - (-13.5) = 0.2$ dB, and median improved by $(-11.3) - (-11.9) = 0.6$ dB. While the range of PDSL values still overlap considerably, for $\bar{\delta} = 90\%$, coarser grid granularity appears to improve PDSL performance somewhat. The minimum and maximum improvement are comparably minor, possibly due to the staggering performance reaching a limit, which is visually suggested by the flat left side of the coarse histogram. A similar analysis was performed for various $\bar{\delta}$, the results of which are compiled in Table 3.1. Recall that $\bar{\delta} < 40\%$ did not provide adequate suppression at $f_{\text{nD}} = 2$, so attention is paid to the cases where $\bar{\delta} \geq 40\%$. The table tells a similar story as Fig. 3.9, with the advantageous formulation (coarse or fine) varying with increasing $\bar{\delta}$.

$\bar{\delta}$	Max. PDSL (dB)			Min. PDSL (dB)			Median. PDSL (dB)		
	Coarse	Fine	Diff.	Coarse	Fine	Diff.	Coarse	Fine	Diff.
40%	-1.5	-1.6	0.1	-2	-3.6	1.6	-2	-2.5	0.5
50%	-2.5	-2.3	-0.2	-6.5	-6	-0.5	-4.2	-3.9	-0.3
60%	-3.3	-3.4	0.1	-7	-8.8	1.8	-5.3	-5.8	0.5
70%	-4.7	-4.6	-0.1	-12	-11.9	-0.1	-8.5	-8.3	-0.2
80%	-5.3	-5.8	0.5	-12	-13.1	1.1	-10.2	-10.6	0.4
90%	-7.3	-7.1	-0.2	-13.5	-13.3	-0.2	-11.9	-11.3	-0.6

Table 3.1: Maximum, Minimum, and Median PDSL over 10^5 random trials of coarse ($K = 5$) and fine ($K = 25$) grid staggering.

3.3.2.2 Redundancy and Cumulative Staggering

The aggregate PDSL for 10^4 grid stagger instantiations is shown in Fig. 3.11, as a function of $\bar{\delta}$. Again, the interval $[1/M, 5-1/M]$ was chosen for sidelobe selection.

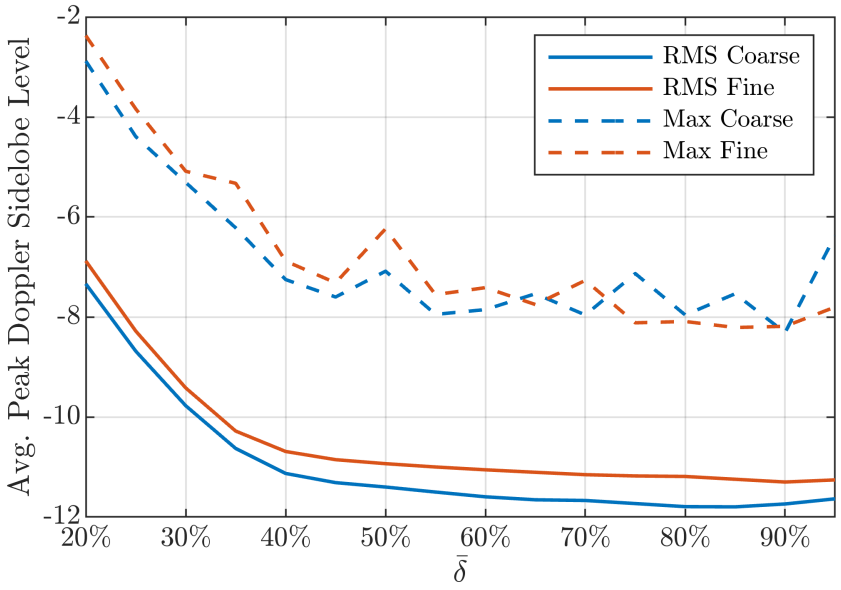

Figure 3.11: Average PDSL for 10^4 random trials of $M = 100$ pulse random cumulative staggered PRIs with varying $\bar{\delta}$ compared for $K = 5, K = 25$.

Contrary to the result for grid staggering in Fig. 3.9, one formulation demonstrates a consistent benefit over another in the average. For cumulative staggering, coarse granularity (high redundancy) clearly possesses a lower average PDSL than the fine granularity discretization, though the

advantage is less present in the maximum PDSL. However, for cumulative staggering the PDSL benefit is diminishing for $\bar{\delta} > 40\%$, so the PDSL behavior with $\bar{\delta}$ is less important beyond this point. Similar to the analysis done for Table 3.1, 10^5 random generations of random cumulative staggering with $\bar{\delta} = 30\%$ was performed, distretized to both a coarse ($K = 5$) and fine ($K = 25$) grid, and the difference between the maximum, minimum and median PDSLs are compiled and shown in Table 3.2.

$\bar{\delta}$	**Max. PDSL (dB)**			**Min. PDSL (dB)**			**Median. PDSL (dB)**		
	Coarse	Fine	Diff.	Coarse	Fine	Diff.	Coarse	Fine	Diff.
30%	-4.6	-4.1	-0.5	-13.2	-12.5	-0.7	-10	-9.7	-0.3
40%	-6.2	-6.3	0.1	-13.6	-13.2	-0.4	-11.3	-10.9	-0.4
50%	-6.7	-6.4	-0.3	-13.8	-13.2	-0.6	-11.6	-11.1	-0.5
60%	-7.5	-6.6	-0.9	-14.1	-13.1	-1	-11.7	-11.2	-0.5
70%	-7	-6.4	-0.6	-14.2	-13.6	-0.6	-11.8	-11.3	-0.5
80%	-6.8	-6.7	-0.1	-14.3	-13.4	-0.9	-11.9	-11.3	-0.6
90%	-7.1	-7.1	0	-14.3	-13.7	-0.6	-11.9	-11.4	-0.5

Table 3.2: Maximum, Minimum, and Median PDSL over 10^5 random trials of coarse ($K = 5$) and fine ($K = 25$) cumulative staggering.

The table corroborates the trends shown in Fig. 3.11; for cumulative staggering, coarse granularity is more likely to produce PRI sequences with lower peak sidelobes.

3.4 Uniqueness of Redundant Sequences

From the perspective of diversity, random PRI staggering is useful due to the uniqueness between sequences inherent in the randomness. When the staggers are independently drawn from a continuous distribution, each sequence can be expected to be unique. By imposing redundancy via grid discretization, sequence uniqueness may be degraded. In order to speak explicitly about this aspect, a uniqueness metric μ developed in [9] based on the PRI stagger co-array is used to analyze the uniqueness between PRI sequences.

3.4.1 PRI Stagger Co-array Revisited

The co-array defined in Eq. 3.1 is further expanded to include the pulsed waveform structure so that a more accurate degree of coherence span due to waveform bandwidth/range resolution may be considered. For the case of repeated unit-energy waveform $s(t)$, let $\tilde{s}(t)$ be the total CPI including all M repeated waveforms $s(t)$ pulses placed at their respective staggered time instances, and zero-valued intervals in between. Then the waveform-included stagger co-array becomes

$$c_{\text{wfm}}(\tau) = \int \tilde{s}(t)\tilde{s}^*(t-\tau)dt \tag{3.4}$$

which realizes an autocorrelation of the entire transmitted CPI, with the peaks in the standard co-array replaced by scaled waveform autocorrelations. This can also be thought of as a Doppler cut of the delay-Doppler ambiguity function for random staggering [6] , which exhibits the familiar "bed-of-nails" structure for a uniform CPI arrangement [5] .

3.4.2 Uniqueness

A slight modification to Eq. 3.4 is introduced in [9] to perform cross-correlation between two sequences. The resulting uniqueness metric is defined as

$$\mu\left[\tilde{s}_1(t), \tilde{s}_2(t)\right] = \frac{1}{M}\max_{\tau}\left|\int \tilde{s}_1(t)\tilde{s}_2^*(t-\tau)dt\right|, \tag{3.5}$$

which can be thought of as a maximum of the "cross-co-array". This metric provides a normalized measure of the two sequences' PRI-dependent structural similarity. The uniqueness metric μ lies on $[1/M, 1]$, with 1 resulting from identical sequences and $1/M$ due to a single correlation peak being the lower bound, implying no commonality between PRIs in the two sequences. Therefore lower μ correspond to more unique sequences.

3.4.2.1 Uniqueness and Grid Staggering

The metric is now used on 1000 independently generated grid staggered sequence pairs discretized according to both $K = 5$ and $K = 25$ granularity. Fig. 3.12 shows the results for $K = 5$ and Fig. 3.13 shows the results for $K = 25$ as a function of $\bar{\delta}$. Also shown is the metric applied to the non-discretized versions of the 1000 sequence pairs in the set in Fig. 3.14.

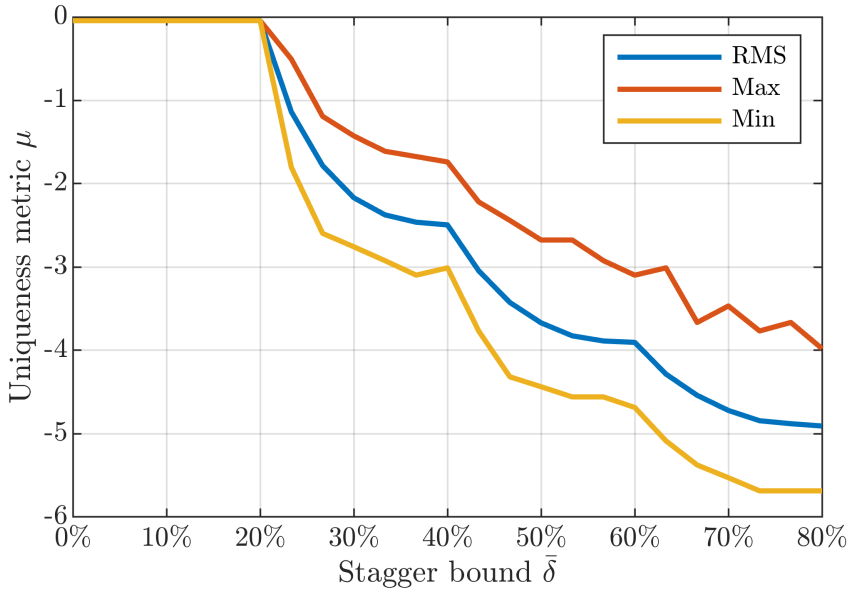

Figure 3.12: Uniqueness metric applied pairwise to 1000 random coarse ($K = 5$) grid stagger sequences of $M = 100$ pulses for different $\bar{\delta}$

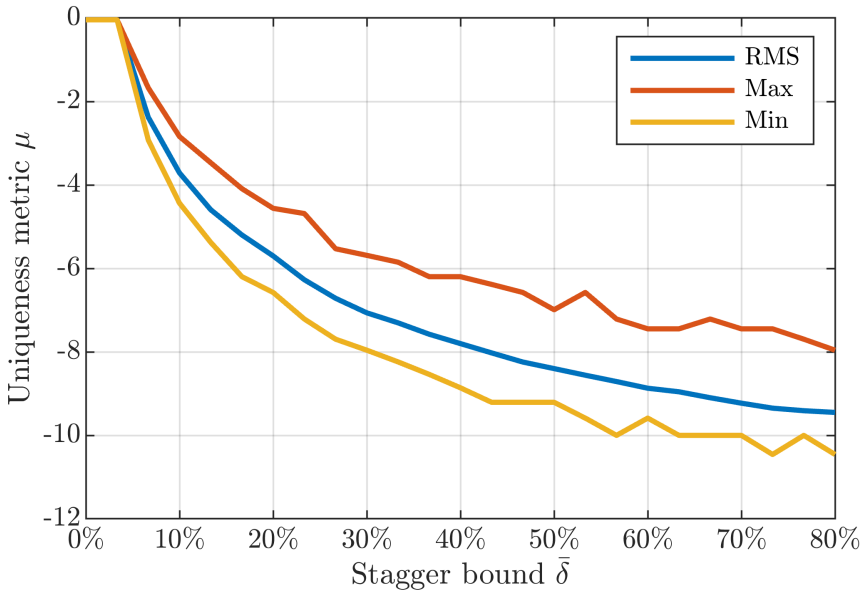

Figure 3.13: Uniqueness metric applied pairwise to 1000 random fine ($K = 25$) grid stagger sequences of $M = 100$ pulses for different $\bar{\delta}$

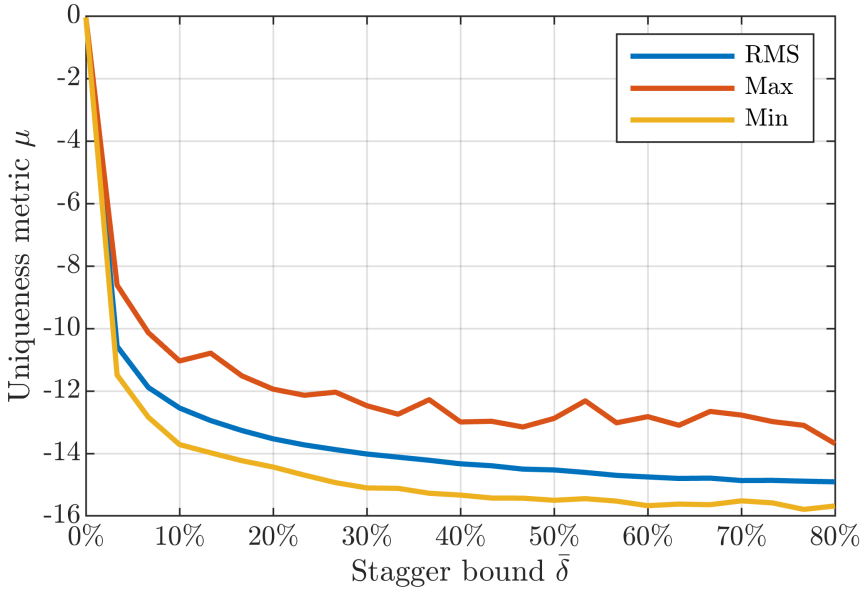

Figure 3.14: Uniqueness metric applied pairwise to 1000 random (no discretization) grid stagger sequences of $M = 100$ pulses for different $\bar{\delta}$

Note that for $K = 5$ grid staggering in Fig. 3.12, the uniqueness between sequences is 0 dB when $\bar{\delta} \leq 20\%$. This is because the discretization process reverts the PRI sequence to the uniform

PRI structure. The same trend is observed in Fig. 3.13 for $K = 25$ when $\bar{\delta} \leq 4\%$. Thus it is required that $\bar{\delta} \geq 1/K$ in order to observe any benefit from grid staggering. Expectedly, for Figs. 3.12 - 3.14, higher stagger deviation results in more unique sequences due to the higher available diversity, shown by the decreasing trend. Also unsurprising is the fact that the undiscretized sequences in Fig 3.14 exhibit higher degrees of uniqueness compared to the discretized versions, with the RMS average approaching an asymptote of -15 dB for undiscretized sequence pairs compared to -9.7 dB for $K = 25$ and -5 dB for $K = 5$. Higher levels of discretization result in sequences that are less unique from one another.

3.4.2.2 Uniqueness and Cumulative Staggering

The same uniqueness simulation is performed for cumulative staggering, with 1000 generated sequence pairs discretized according to $K = 5$ in Fig. 3.15, $K = 25$ in Fig. 3.16, and undiscretized in Fig. 3.17.

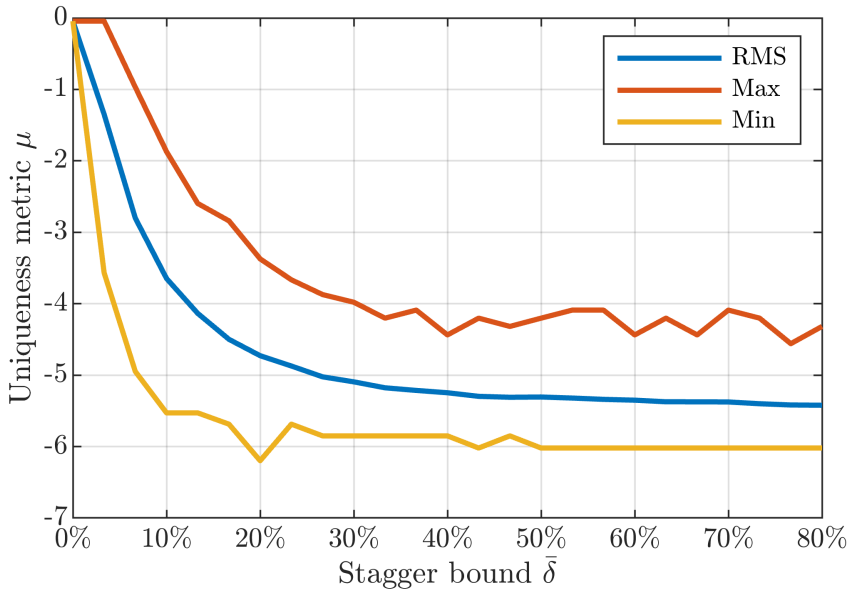

Figure 3.15: Uniqueness metric applied pairwise to 1000 random coarse ($K = 5$) cumulative stagger sequences of $M = 100$ pulses for different $\bar{\delta}$

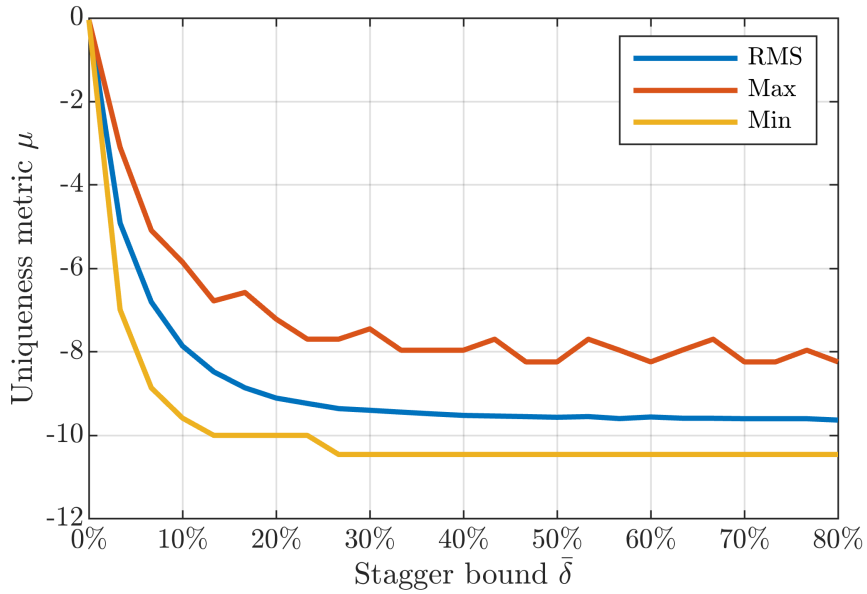

Figure 3.16: Uniqueness metric applied pairwise to 1000 random fine ($K = 25$) cumulative stagger sequences of $M = 100$ pulses for different $\bar{\delta}$

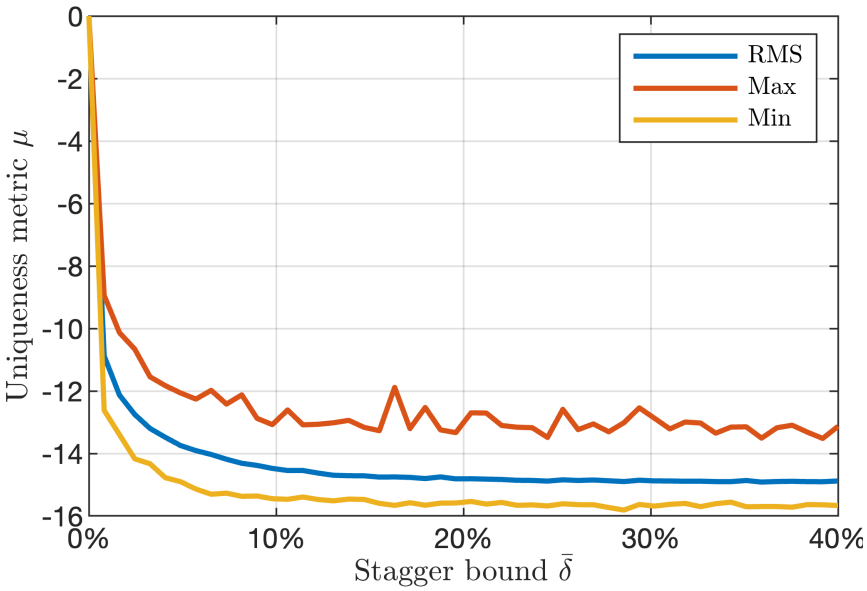

Figure 3.17: Uniqueness metric applied pairwise to 1000 random (no discretization) cumulative stagger sequences of $M = 100$ pulses for different $\bar{\delta}$

Since cumulative staggering can achieve a greater diversity of pulse locations, the same flat trend for grid staggering does not exist for $K = 5$ in Fig. 3.15. The maximum uniqueness curve

does, however, stay flat at 0 dB for $\bar{\delta} < 4\%$, likely due to a lack of suppression of the first Doppler ambiguity. Cumulative staggering is able to construct more unique sequences compared to grid staggering, for all levels of redundancy shown. Within the cumulative staggering set, more redundancy results in less uniqueness between sequences, which makes intuitive sense and is consistent with the grid staggering case.

This chapter explored the effect of redundancy in the PRI staggering co-array on the Doppler response and on the degree of uniqueness between generated sequences. It was shown that the degree of redundancy controls the unambiguous Doppler interval. When using cumulative staggering, it was found that higher degrees of redundancy can contribute to lower peak sidelobe levels, and less uniqueness between sequences. This chapter considered only purely random PRI sequences, which still exhibit unpredictable behavior. The next chapter details design approach involving a gradient-based optimization for low peak sidelobes.

Chapter 4

Gradient-Based Optimization

This chapter reports on a gradient-based optimization procedure developed in [9] that is shown to reduce peak Doppler sidelobes within a desired Doppler interval. First a cost function is defined and posed as a continuous function of underlying continuous parameters, thereby facilitating determination of the gradient. The gradient is provided and used to perform optimization, and performance is assessed in simulation as well as using open-air experimental data.

4.1 Cost Function and Gradient

4.1.1 Cost Function: Generalized Integrated Sidelobe Level (GISL)

The PRI staggering formulation discussed previously is dependent on bounded deviations on $[-\bar{\delta},+\bar{\delta}]$ from the uniform PRI arrangement. This bound may be preserved during optimization by imposing constraints, but here a bounding function is used so that

$$\varepsilon_m = 1+\Delta\varepsilon_m \stackrel{\Delta}{=} 1+\bar{\delta}\sin(\alpha_m) \tag{4.1}$$

for $m = 1,2,...,M-1$ produces a PRI bounded on $\left[1-\bar{\delta},1+\bar{\delta}\right]$ for any real-valued α_m. Note that here the cumulative model is used to generate stagger sequences, since it affords more sidelobe suppression with less range swath loss than the grid staggered model. The vector $\boldsymbol{\alpha} = [0\,\alpha_1\,\alpha_2\,\ldots\,\alpha_{M-1}]^T$ collects these deeper parameters so that the Doppler response $u(\boldsymbol{\varepsilon}(\boldsymbol{\alpha}))$ from Eq. 2.28 possesses a continued functional dependence.

The generalized integrated sidelobe level (GISL) metric was introduced in [51] as a cost func-

tion for optimizing polyphase-coded frequency modulated (PCFM) waveforms for desired autocorrelation sidelobe properties. The PCFM framework is parameterized according to a discrete set of real, scalar parameters [52, 53], lending itself easily to optimization. In [54, 55], the GISL metric is used in a gradient-based optimization to control autocorrelation sidelobes in PCFM waveforms. Recently this optimization was extended to consider other "quasi-bases" [56] , and to design Constant-Envelope Orthogonal Frequency Modulated (CE-OFDM) waveforms in [57] . Here the cost function is applied to the Doppler response, giving

$$J_p(\boldsymbol{\alpha}) = \frac{\| \mathbf{w}_{\text{sl}} \odot \mathbf{u}(\alpha) \|_p^2}{\| \mathbf{w}_{\text{ml}} \odot \mathbf{u}(\alpha) \|_p^2} \tag{4.2}$$

for $\odot$ denoting the Hadamard product, and $\mathbf{w}_{\text{sl}}$ and $\mathbf{w}_{\text{ml}}$ being $N \times 1$ vectors containing ones and zeros that select for the sidelobes and mainlobe, respectively. The mainlobe selector $\mathbf{w}_{\text{ml}}$ has ones on $f_{\text{nD}} \in [0, 1/M]$. Since the region near-in the mainlobe is low and is not greatly affected by staggering [7], additional computational efficiency can be obtained by ignoring this region so that the vector $\mathbf{w}_{\text{sl}}$ selects $f_{\text{nD}} \in [0.5, 0.5\beta_{\text{opt}}]$. For $p = 2$, the cost function in Eq. 4.2 becomes the integrated Doppler sidelobe level (IDSL), which provides a metric for describing average sidelobe level. For $p \to \infty$, Eq. 4.2 becomes a peak Doppler sidelobe (PDSL) metric as the largest term dominates the norm. Since a flat sidelobe response is desired, PDSL is more useful in this context so that the maximum sidelobes are minimized. As p is increased, the computational complexity quickly blows up, so here the value $p = 10$ is used as it is sufficient to achieve flat Doppler sidelobes. The IDSL and PDSL metrics are used independently in Section 4.3.2 analyzed in the context of optimized Doppler responses

One last note before the gradient is presented: Eq. 4.2 is a nonconvex function of α, and therefore optimization will likely converge toward different solutions depending on the random initialization. Thus, though optimized PRI sequences may obtain qualitatively similar Doppler responses, the particular solutions will likely be distinct from each other. This uniqueness aspect is explored in Section 4.3.3.

4.1.2 Gradient

The derivation in the appendix of [55] is leveraged here to determine the gradient of Eq. 4.2. In [55], the GISL cost function is used to optimize the underlying parameters for polyphase-coded FM [52] waveforms, the autocorrelation of which is analogous to Eq. 2.28 in the Doppler context. Here the functional dependence between the response in question (pulse compression for the waveform case and Doppler spectrum for the PRI staggering case) and the underlying optimizable parameter is changed. Appendix A of this thesis as well as [9] derives the gradient to be

$$\nabla_{\boldsymbol{\alpha}} J_p = \frac{4\pi\bar{\delta}}{M} J_p \mathbf{G}^T \left[\frac{\mathbf{w}_{\mathrm{sl}}}{\mathbf{w}_{\mathrm{sl}}^T |\mathbf{u}|^p} - \frac{\mathbf{w}_{\mathrm{ml}}}{\mathbf{w}_{\mathrm{ml}}^T |\mathbf{u}|^p} \right], \tag{4.3}$$

with the $M \times N$ matrix $\mathbf{G} = [\mathbf{0}_{N\times 1}\, \mathbf{g}_1 \ldots \mathbf{g}_{M-1}]$, where

$$\mathbf{g}_m = |\mathbf{u}|^{(p-2)} \odot \Im \left\{ \left(\left(\mathbf{V}^H \odot \left(\mathbf{f}_{\mathrm{nD}} \left(\cos\{\boldsymbol{\alpha} \odot \mathbf{e}_m\} \right)^T \mathbf{B}^T \right) \right) \mathbf{v}_0 \right) \odot \mathbf{u}^* \right\} \tag{4.4}$$

where $\Im\{\bullet\}$ takes the imaginary part of the argument, $\mathbf{e}_m$ is an $M \times 1$ elementary vector containing all zeros save for a 1 at the m^{th} element, and $(\bullet)^*$ denotes complex conjugation. This gradient can now be used in any gradient-based optimization framework to optimize the real, scalar parameters in $\boldsymbol{\alpha}$ for low sidelobes in the Doppler response.

4.2 Method

The optimization is performed here using the limited-memory Broyden–Fletcher–Goldfarb–Shanno (BFGS) algorithm [58] , which is an unconstrained quasi-Newton method that requires only a gradient calculation at each iteration, avoiding the costly Hessian calculation characteristic of the Newton method. The algorithm is implemented using the function "minf_lbfgs" from the Tensorlab toolbox [59] , with the objective function iterative difference tolerance set to 10^{-7} and the step-size tolerance set to 10^{-8}. The parameter values α_m for $m = 1, 2, ..., M-1$ are drawn from a uniform distribution on $[-\pi, +\pi]$ and used to produce a random stagger sequence via Eq. 4.1 for

some chosen $\bar{\delta}$. The PRIs thereby fall on a sine distribution, which tends to have a flatter Doppler response than for uniformly distributed PRIs (due to the bimodal nature of the sine distribution meaning higher probability for large stagger values), and thus requires fewer iterations to converge. Additional computational efficiency is achieved by exploiting the symmetry of the Doppler response and considering only the interval $f_{\text{nD}} \in [0, 0.5\beta_{\text{opt}}]$, plus the additional buffer discussed in Section 2.2.3.2.

4.3 Assessment of PRI Stagger Optimization

In this section the results of the optimization method presented in the previous section are shown and analyzed, including examples of the improved Doppler responses, a Monte Carlo numerical analysis using the IDSL and PDSL metrics, and a uniqueness assessment between initial and corresponding optimized sequences using the metric defined in Section 3.4.2.

4.3.1 Optimized Doppler Response

The benefit of optimization is demonstrated in the two examples of random initializations with particularly high PDSL shown in Figs. 4.1 and 4.2. These were the worst cases observed in 1000 instantiations of random staggering formed according to Eq. 4.1, for $M = 100$, $\bar{\delta} = 30\%$, and $\beta_{\text{opt}} = 4$. Implemented as described in the previous section, gradient-based optimization achieves a 9.8 dB PDSL improvement in Fig. 4.1, in which a large peak is observed at $f_{\text{nD}} = 1$ where the mainlobe would be repeated for the uniform PRI case. The optimization clearly works as intended, flattening the entire sidelobe pedestal. Though the second example in Fig. 4.2 shows a smaller PDSL improvement (8.8 dB), this particular random instantiation could be even more problematic, as it contains multiple peaks that could result in false alarms. These two cases exemplify the need for optimization, as random PRI staggering can exhibit very high sidelobes if they are not mitigated via careful PRI design. Observe that the response over the interval $[0, 0.75]$ follows the uniform PRI response closely.

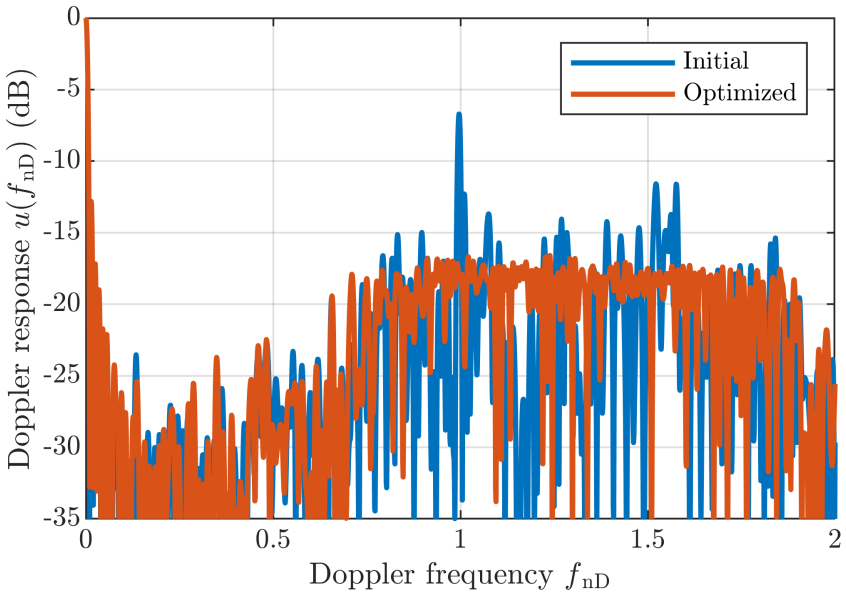

Figure 4.1: Single instantiation of random staggering for M = 100 and compared to gradient-based optimization (9.8 dB PDSL improvement)

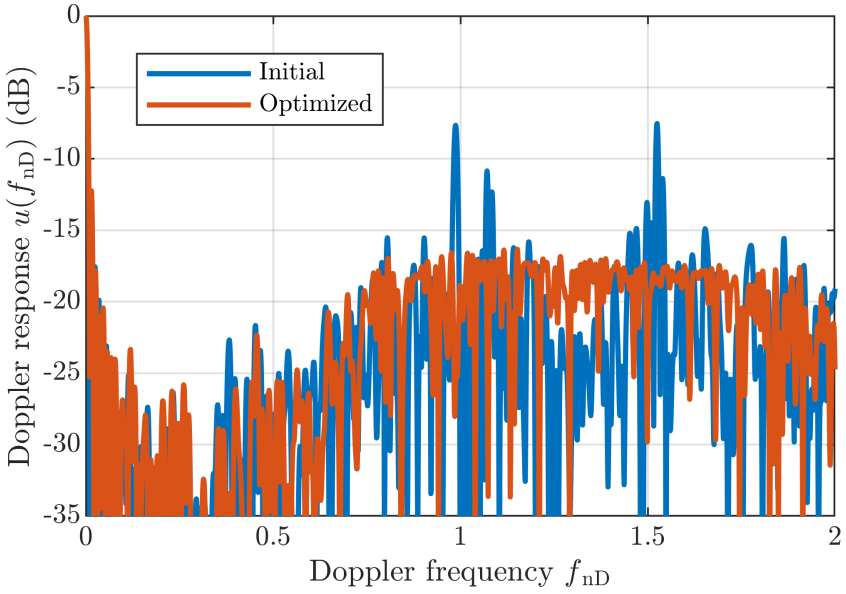

Figure 4.2: Single instantiation of random staggering for M = 100 and compared to gradient-based optimization (8.8 dB PDSL improvement))

To observe the overall behavior of this optimization, now consider the Doppler response in aggregate over the 1000 independent trials, shown in Fig. 4.3. Only examining the root-mean-

square (RMS) curves, the advantage of the optimized over the initial responses is not evident, with the former exhibiting a modest flattening of the latter. However, as was exemplified in Figs. 4.1 and 4.2, it is the peak sidelobe that may pose problems. The maximum at each f_{nD} across the 1000 trials reveals that optimization does in fact reduce the peak level, by 2-10 dB over the entire sidelobe extent. The maximum curves additionally show that optimization tends toward a more consistent peak value across the entire Doppler span. The greatest degree of improvement occurs at $f_{\mathrm{nD}} = 1$, which corresponds to the high sidelobe peaks in Figs. 4.1 and 4.2 and aligns with the first ambiguity for the uniform PRI case, suggesting that some random instantiations retain a degree of uniform structure. Further, notice that the optimized RMS and maximum curves are much closer than those for the initialization, indicating that the optimization produces a more consistent result with less variance. In short, optimization avoids the worst-case conditions that randomness may induce.

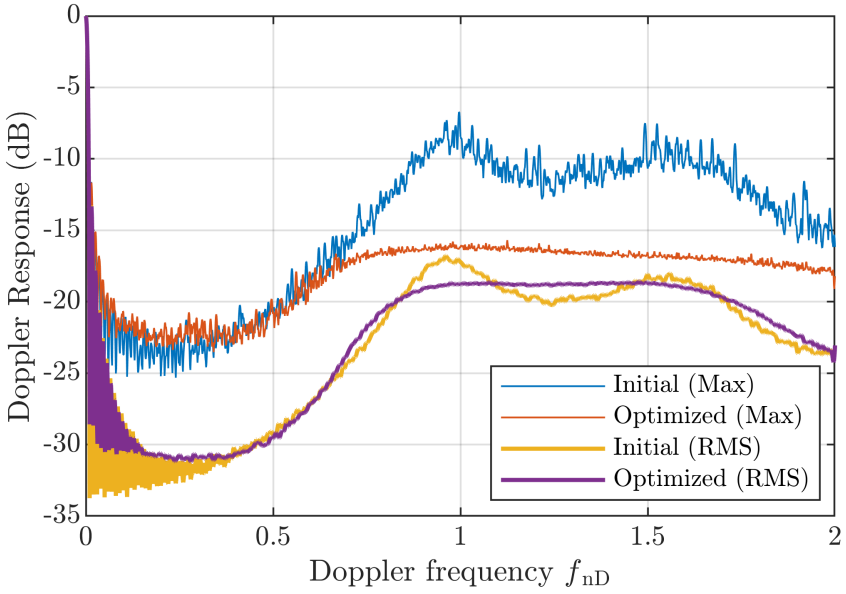

Figure 4.3: Aggregate mean and maximum of random staggering for M = 100 and compared to gradient-based optimization

4.3.2 Numerical Analysis

The GISL cost function from Eq. 4.2 was described in terms of the integrated Doppler sidelobe (IDSL) and peak Doppler sidelobe (PDSL). Here these metrics are formally defined and used to analyze the impact of optimization.

4.3.2.1 Integrated Doppler Sidelobe Level (IDSL) and Peak Doppler Sidelobe Level (PDSL) Definitions

First, the IDSL is

$$\text{IDSL} \triangleq \frac{\| \mathbf{w}_{\text{sl}} \odot \mathbf{u} \|_{p=2}^2}{\beta_{\text{opt}} \| \mathbf{w}_{\text{ml}} \odot \mathbf{u} \|_{p=2}^2}, \tag{4.5}$$

where β_{opt} is the chosen Doppler span for optimization, $\mathbf{w}_{\text{sl}}$ and $\mathbf{w}_{\text{ml}}$ select for the sidelobes ($f_{\text{nD}} \in [0.5, 0.5\beta_{\text{opt}}]$) and mainlobe (($f_{\text{nD}} \in [0, 1/M]$), respectively, and $\mathbf{u}$ is the Doppler response from Eq. 2.28.

The PDSL was loosely defined in Eq. 3.3. Explicitly defined as a special case of the GISL cost function, it is

$$\begin{aligned} \text{PDSL} &\triangleq \frac{\| \mathbf{w}_{\text{sl}} \odot \mathbf{u} \|_{p\to\infty}^2}{\beta_{\text{opt}} \| \mathbf{w}_{\text{ml}} \odot \mathbf{u} \|_{p\to\infty}^2} \\ &= \frac{\max\limits_{f_{\text{nD}}} |\mathbf{w}_{\text{sl}} \odot \mathbf{u}|^2}{\max\limits_{f_{\text{nD}}} |\mathbf{w}_{\text{ml}} \odot \mathbf{u}|^2}, \end{aligned} \tag{4.6}$$

which simply measures the ratio of the highest Doppler sidelobe to the mainlobe peak (at $f_{\text{nD}} = 0$) over the same intervals as the IDSL metric.

4.3.2.2 IDSL and PDSL Histograms

Applying these metrics to the sets of 1000 independent random initial and optimized trials (with $\bar{\delta} = 30\%$, $M = 100$, and $\beta_{\text{opt}} = 4$), specific information about the optimization behavior is

revealed.

When only considering the histogram of IDSL in Fig. 4.4, optimization does not appear to improve the sidelobe response much, with the initial and optimized histograms centered around a similar value. Indeed optimization for this particular M, $\bar{\delta}$, β_{opt} does not improve the IDSL much, only slightly tightening the distribution indicating a more consistent average sidelobe behavior. This behavior can be explained in Fig. 4.3 by the observation that the average curves are close and would integrate to a similar value over the same extended Doppler interval.

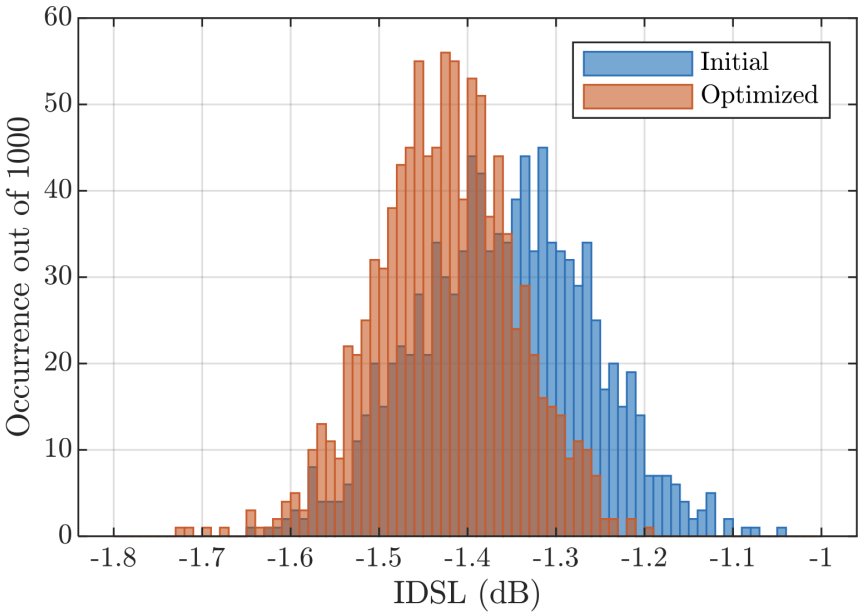

Figure 4.4: Histogram of IDSL for 1000 independent initial and optimized random stagger sequences for $M = 100$, $\bar{\delta} = 30\%$, and $\beta_{\text{opt}} = 4$

In contrast, observe the PDSL histogram in Fig. 4.5, in which the benefit of optimization is immediately apparent. Indeed this metric is more telling, as the goal of optimization is to flatten peak sidelobes and achieve a level closer to the theoretical limit of $10\log_{10}(1/M)$, which was the reason for the choice of $p = 10$. Fig 4.5 reveals the PDSL is distinctly decreased via optimization, and moreover the distribution possesses significantly less variance, indicating that PDSL is more consistent among the optimized sequences. Specifically, 98.9% of trials lie between -17 and -16 dB centered on the median of -16.5 dB. By comparison, this same percent of trials for the initial random stagger sequences lie between -13.5 and -8.4 dB centered on the median of -10.9 dB.

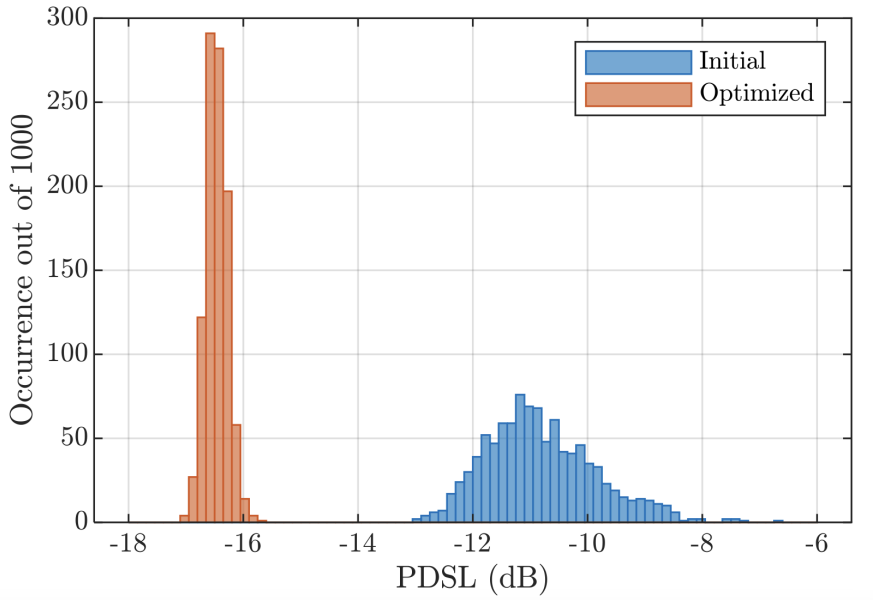

Figure 4.5: Histogram of PDSL for 1000 independent initial and optimized random stagger sequences for $M = 100$, $\bar{\delta} = 30\%$, and $\beta_{\text{opt}} = 4$

While the histogram in Fig. 4.5 clearly demonstrates a performance enhancement via optimization, it is also worth examining the PDSL improvement on a case-by-case basis. A histogram for the improvement in PDSL for each trial is shown in Fig. 4.6, wherein between 3 and 10 dB of improvement is obtained over the 1000 trials, with a median around 5.6 dB. Based on the examples in Section 4.3.1, it can be inferred that the most improvement is achieved when the PDSL for the random initialization is particularly severe.

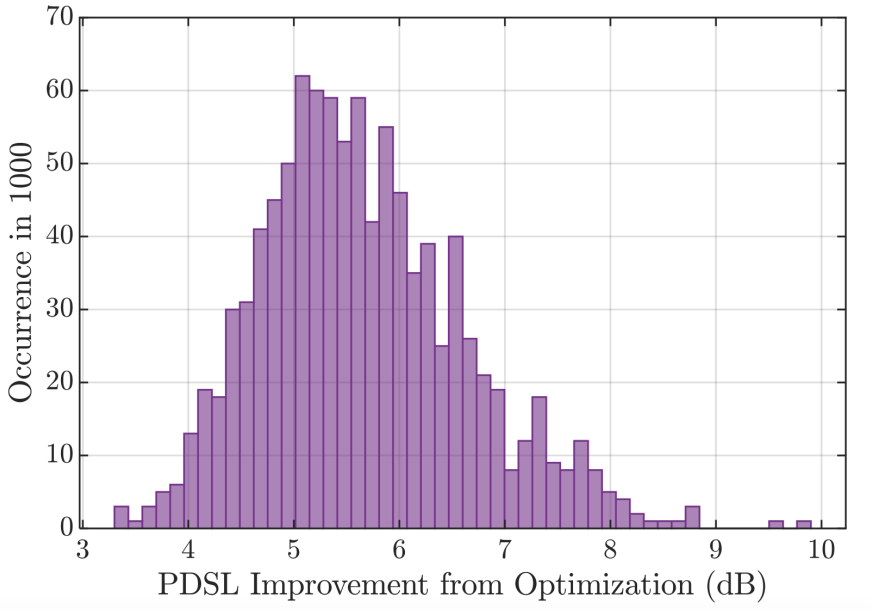

Figure 4.6: Histogram of PDSL improvement between 1000 independent initial and optimized random stagger sequences for $M = 100$, $\bar{\delta} = 30\%$, and $\beta_{\text{opt}} = 4$

4.3.2.3 PDSL Behavior with Stagger Limit and Optimized Doppler Interval

The choice of stagger limit $\bar{\delta}$ and optimized Doppler interval β_{opt} do affect the optimization performance shown in the previous section. First, consider the impact on the PDSL as $\bar{\delta}$ is varied. The RMS average over 1000 independent trials is evaluated for $\bar{\delta}$ from 0% to 50%, and the $10\log_{10}(\bullet)$ of the average PDSL is plotted in Fig. 4.7. The initial PDSL curve clearly demonstrates a downward trend, with a small bump around 40%. From Fig. 2.7, the same trend is portrayed: a flattening of the expected Doppler response with increasing stagger limit.The optimized result has a monotonically decreasing trend, suggesting that the available diversity from a greater stagger limit allows for better optimization solutions to exist.

The difference between the initial and optimized responses is the largest at approximately 8 dB for around $\bar{\delta} = 5\%$ and about 6 dB at the point of least difference, about $\bar{\delta} = 30\%$. Note that this plot is intended to show optimized PDSL performance as a function of $\bar{\delta}$ to reveal trends, but that realistically higher $\bar{\delta}$ should be avoided due to greater blind range swath and shorter range ambiguities. Based on Fig. 4.7, the justification for the choice of $\bar{\delta} = 30\%$ becomes clear, as

staggering where $\bar{\delta} > 30\%$ does not pose an additional advantage.

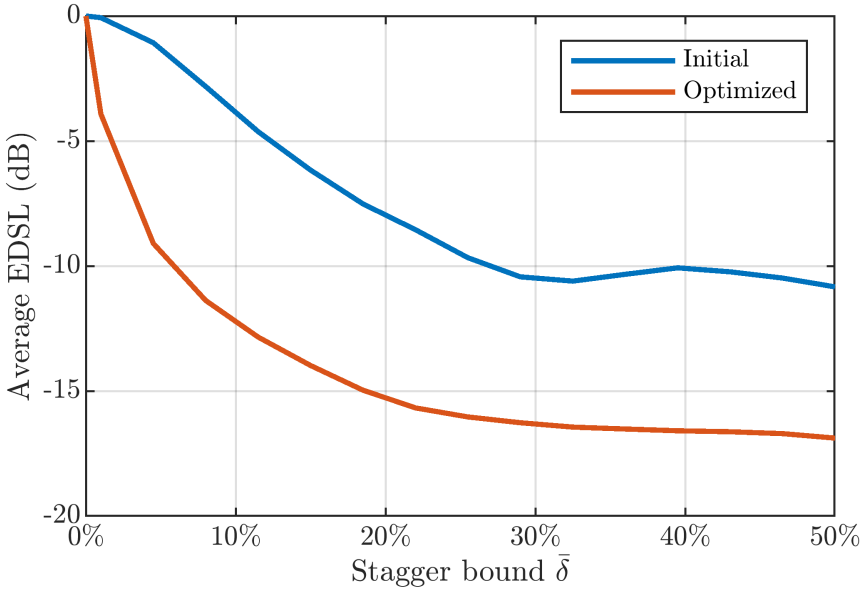

Figure 4.7: Mean PDSL as a function of $\bar{\delta}$ over 1000 independent initial and optimized random stagger sequences for $M = 100$ and $\beta_{\text{opt}} = 4$

Next, consider the same experiment but for fixed $\bar{\delta} = 30\%$ and β_{opt} varied from 1 to 20. One can intuit that as PDSL is evaluated over an increasing Doppler interval, the initial random instantiations have a higher likelihood of exhibiting a high peak in the extended sidelobe response. Additionally the available degrees of freedom M must contend with a larger Doppler span over which to optimize. Observe Fig. 4.8, which displays a monotonically increasing trend in PDSL for both the initial and optimized sequences, albeit with a slightly different shape between the two curves. An interesting inflection exists at $\beta_{\text{opt}} = 1.5$ (or $f_{\text{nD}} \in [0, 0.75]$) for the initial sequence. The reason for this inflection can be understood when noting that the extension of β_{opt} from 1 to 1.5 extracts only the sidelobes from the low roll-off region near the mainlobe, where the phase slope deflection from Section 2.3.3 is not great enough to provide the sidelobe flattening effect seen for $f_{\text{nD}} > 0.75$. For $\beta_{\text{opt}} > 1.5$, the first Doppler ambiguity is subsumed, which tends to have its largest value at/near $f_{\text{nD}} = 1$. For higher β_{opt} (> 6) the rate of increase reduces considerably while still gradually trending upward, which makes sense when considering that PDSL is being computed (or optimized for) over a progressively larger span. Still, PDSL is consistently improved

by optimization for all β_{opt}.

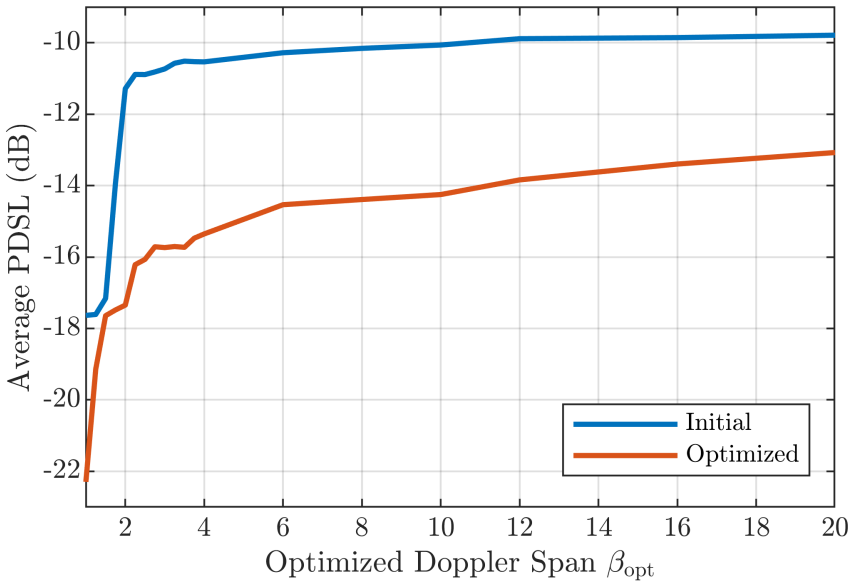

Figure 4.8: Mean PDSL as a function of Doppler span β_{opt} over 1000 independent initial and optimized random stagger sequences for $M = 100$ and $\bar{\delta} = 30\%$

4.3.3 Uniqueness Assessment

As discussed in Section 3.4, a prospective benefit of random PRI staggering is the unique nature of each PRI sequence. The nonconvex nature of the cost function in Eq. 4.2 likely realizes optimized sequences that, when differently initialized, maintain their uniqueness from one another. The effect of optimization on uniqueness is demonstrated using the uniqueness metric from [8] used in Section 3.4. Examples of the waveform-dependent co-array from Eq. 3.4 are shown in Fig. 4.9 for the case of a uniform CPI, a random initialization, and an optimized version thereof, with $s(t)$ being an LFM with an oversampling factor of 5 relative to swept bandwidth. The uniform co-array exhibits the familiar triangle shape characteristic of the maximally redundant array. The random and optimized sequences produce co-arrays with significantly fewer redundancies as the PRI intervals are no longer aligned. The random initialization realizes a nearly minimal redundancy co-array, whereas the optimized co-array produces a slight increase near-in 0 lag. While the co-array is shown in absolute scale, the cutaway in Fig. 4.9 shows a zoomed version of the final

peak in the co-array in decibel scale, showing that the peaks are scaled versions of the waveform autocorrelation.

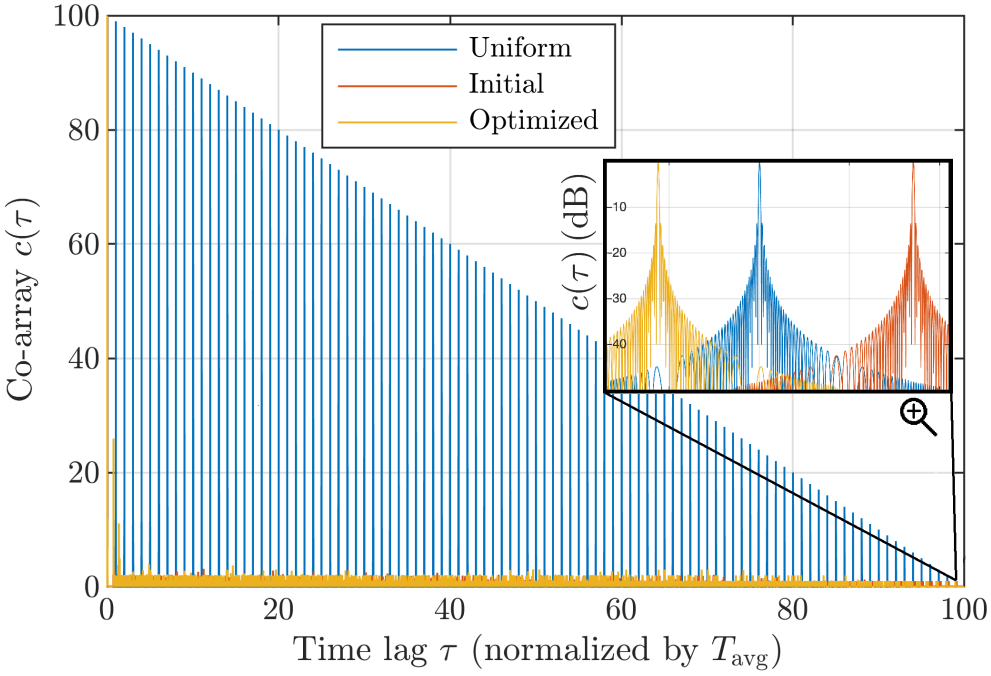

Figure 4.9: Stagger co-array for $M = 100$ pulses in uniform, random, and optimized configurations

The metric from Eq. 3.5 is applied pairwise between sequences drawn from a set of 1000 independent random sequences. The same sequences are optimized according to the method described in Section 4.2 using the same function settings. The optimized sequences corresponding to the same pairs used to evaluate the initial μ are then used to determine an optimized μ. In Fig. 4.10 and 4.11, histograms are shown for $\bar{\delta} = 5\%$ and $\bar{\delta} = 20\%$ to further analyze the trend with $\bar{\delta}$.

For $\bar{\delta} = 5\%$, the initial and optimized median are similar: -11.4 dB and -11.6 dB respectively. However the optimization clearly has an unpredictable effect on uniqueness, even greatly reducing uniqueness with 28.8% of trials resulting in μ greater than -4 dB. This is likely because the available solution space is smaller with the limited stagger boundary. For $\bar{\delta} = 20\%$, the initial and optimized sequences have an equal median of -15.0 dB. However the optimization slightly widens the distribution, with 91.5% of trials lying on the interval -15.5 dB to -14 dB, compared to 97.5% of trials lying on this same interval for the initial sequences. The optimization may diminish the

uniqueness afforded by the initial sequence, with 2.2% of trials lying on the interval from -14 dB to -11.5 dB, and 7.4% on the same interval for the optimized case. This may be explained by the increased redundancy in the optimized sequence as discussed in [8] and Chapter 3. Even so, for an adequate stagger limit, a high degree of uniqueness is achieved between optimized sequences.

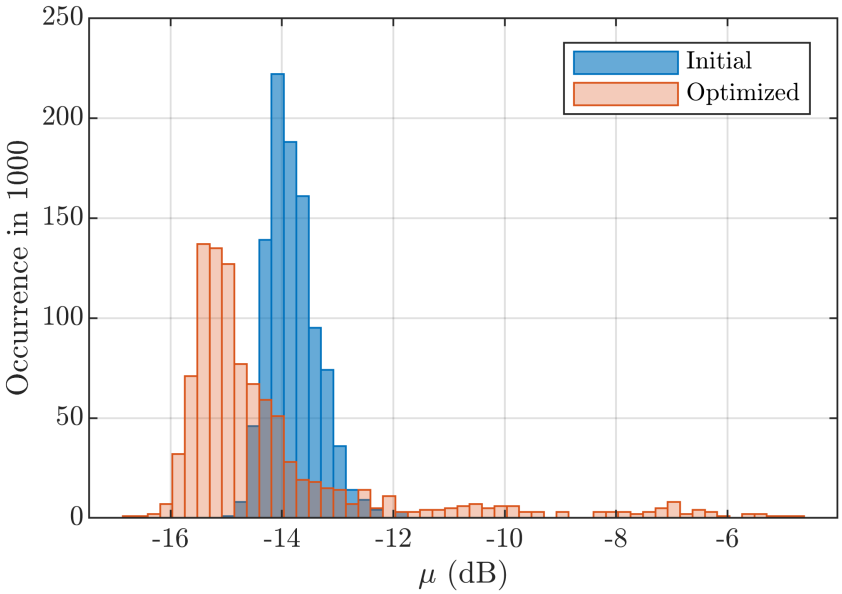

Figure 4.10: Histograms for uniqueness metric applied pairwise within the 1000 random stagger sequences and (separately) within the 1000 optimized sequences for $M = 100$ pulses and $\bar{\delta} = 5\%$

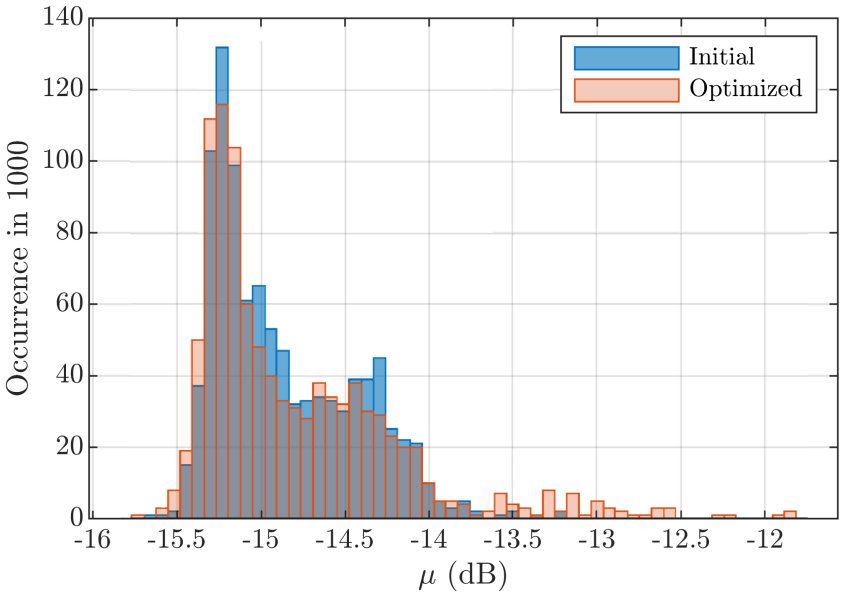

Figure 4.11: Histograms for uniqueness metric applied pairwise within the 1000 random stagger sequences and (separately) within the 1000 optimized sequences for $M = 100$ pulses and $\bar{\delta} = 20\%$

4.3.3.1 Shuffled Sequences

The optimized sequences consistently have a flatter sidelobe performance than the initial sequences, for the same stagger limit $\bar{\delta}$ and over the same Doppler interval β_{opt}. There must therefore be a particular aspect of these optimized sequences that produces a flat Doppler response. Hypothesizing that the structure/ordering of the PRI sequence is of special importance, an analysis of optimized, then permuted PRI sequences follows.

First, consider the metric in Eq. 3.5 [9] applied to an optimized sequence paired with 1000 random permutations of the same sequence. Fig. 4.12 displays a histogram of the results. Random shuffling of a single optimized sequence is seemingly able to generate endless unique sequences.

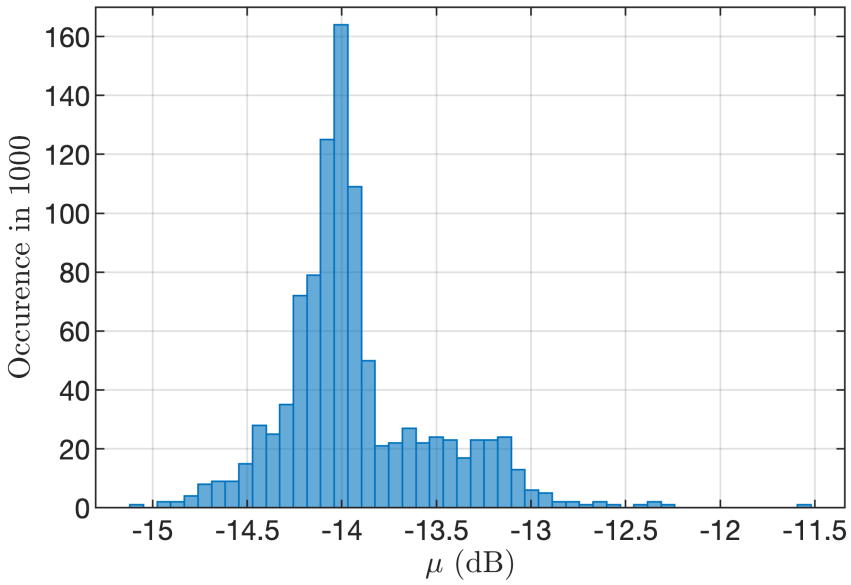

Figure 4.12: Histogram for uniqueness metric applied between an optimized PRI sequence and 1000 random permutations of the same sequence for $M = 100$ pulses, $\beta_{\text{opt}} = 4$, and $\bar{\delta} = 30\%$

A different perspective is gleaned by showing the PDSL histogram for 1000 optimized then shuffled sequences, overlaid on the PDSL histograms from Fig. 4.5. Randomly shuffling the order of the optimized sequence consequently degrades the Doppler response almost completely to the sidelobe perfomance achieved by a random stagger generation. Thus it can be concluded that the particular ordering is a significant feature of the optimized PRIs that produces sidelobe flattening. This result can be intuitively understood by considering that the sidelobe cancellation effect is achieved via a phase-decoherence that is determined by the cumulative PRI values per Eq. 2.20 and Eq. 2.28. A re-ordering of these PRIs would change the cumulative values and thus could not guarantee the sidelobe flattening effect granted by optimization.

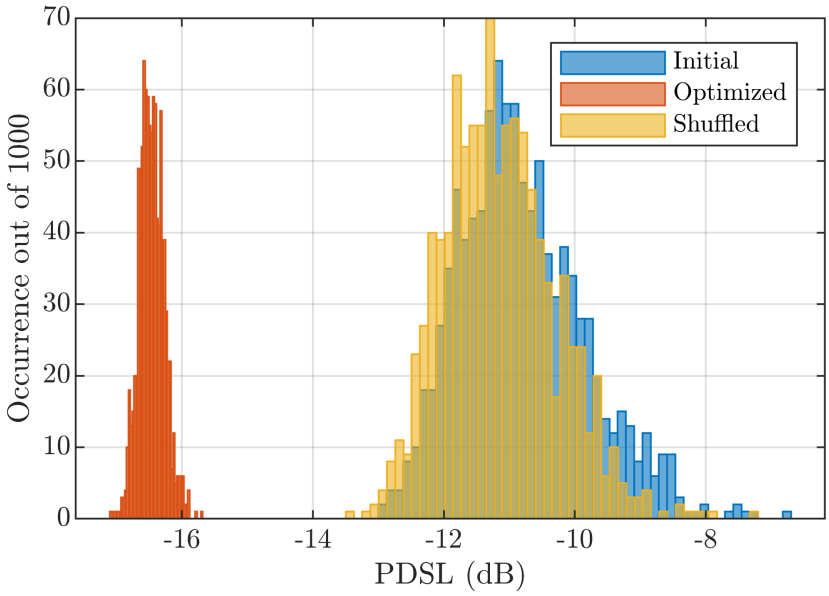

Figure 4.13: Histograms of PDSL for $M = 100$, $\bar{\delta} = 30\%$, and $\beta_{\text{opt}} = 4$ with each optimized sequence having the order of its PRIs randomly shuffled

4.3.4 Effect of CPI Scaling

In Section 2.1.1.1, it was demonstrated that the cumulative model may produce PRIs that slightly violate the per-PRI design boundary $[1-\bar{\delta}, 1+\bar{\delta}]$ after scaling to maintain a fixed CPI extent. Fig. 4.14 shows a similar histogram to Fig. 2.4 in the mentioned section, but for 1000 trials of $M = 100$ pulse CPIs of random initializations according to Eq. 4.1 and their corresponding optimized sequences, after scaling.

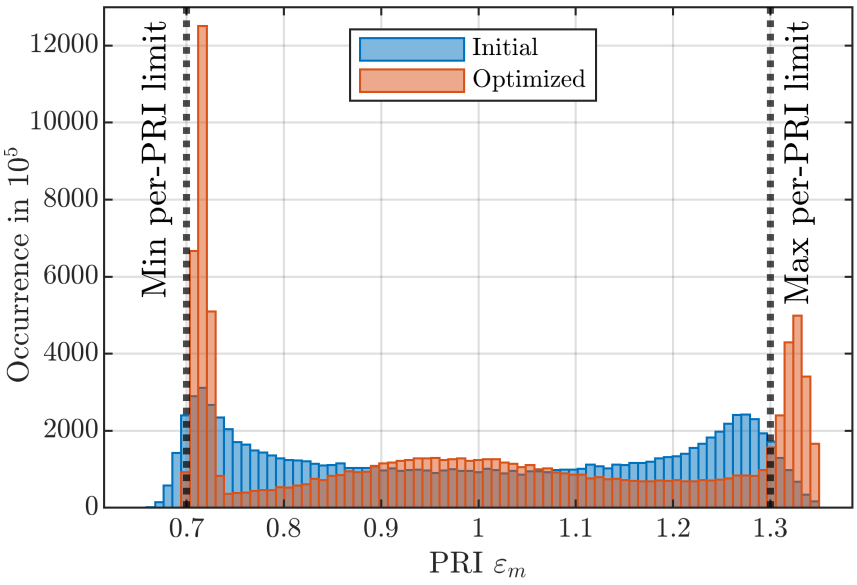

Figure 4.14: Histograms of initial and optimized PRIs post-scaling for 100 trials with $M = 100$, $\bar{\delta} = 30\%$, and $\beta_{\text{opt}} = 4$

Optimization exaggerates the bimodal distribution already present in the initialization due to the sine bounding function, as more PRI diversity corresponds to flatter sidelobes. Thus a pronounced number more PRIs fall outside of the upper per-PRI stagger limit, albeit only by a modest amount. On the other side of the distribution, however, optimization has improved the number of PRIs falling below the minimum limit. Since the contraction case is more problematic due to the augmented effect of blind ranges, and dilation is not an issue so long as β_{opt} is sufficient, optimization has conveniently mitigated the minor disadvantages created by CPI scaling.

4.3.5 Timing Quantization

The optimization described in this Chapter is based on PRI values lying on a continuum to enable determination of a gradient. However in real systems, where digital hardware is used, timing is dictated by an internal clock. The PRI values must therefore by quantized according to a radar system's receiver digital-to-analog converter rate. Since the waveform realistically has some bandwidth and the coherence span is $\pm 1/B$ [7], any timing quantization that is sufficiently less than $1/B$ would result in a negligible deviation from the optimized result.

4.4 Experimental Validation

To confirm the applicability of optimized PRIs, open-air experimental data was collected. The transmit and receive beams were pointed at the intersection of 23rd St. and Iowa St. in Lawrence, KS, from the rooftop of Nichols hall at the University of Kansas at a distance of about 1.1 km. The measurements were captured when North-South traffic accelerated after a stoplight change. Fig. 4.15 shows the geometry of the scene via Google Earth image.

Figure 4.15: Geometry of data collect

The waveforms were generated using a Tektronix 70002A arbitrary waveform generator with a 10 gigasamples/second sample rate and a center frequency of 3.45 GHz. The backscatter was captured using a Rohde & Schwarz real-time spectrum analyzer, and sampled at 200 megasamples/s after the signal was down-converted to baseband.

4.4.1 Waveform

The transmitted waveform consisted of three concatenated 250 ms CPIs containing repeated LFM chirp waveforms with 160 MHz swept bandwidth and 5 μs pulsewidth. The first two CPIs were composed of $M = 100$ randomly staggered sub-CPIs with $\bar{\delta}$ and the optimized version using β_{opt}, in that order. The sub-CPIs contained 10 uniformly spaced pulses at a PRF of 40 kHz. Each of these sub-CPIs was coherently integrated by presumming after pulse compression. The sub-CPIs had an effective PRF of 400 Hz on average, corresponding to an unambiguous velocity of $\pm$8.7 m/s

for the uniform case. Thus a comparable uniform sub-CPI can be expected to alias in the context of a 40 mph speed limit (17.9 m/s).

The third CPI contained 200 sub-CPIs with uniform arrangement and an 800 Hz effective PRF. By processing all 200 sub-CPIs, a ground truth is established. By down-selecting every other pulse in the uniform CPI, an $M = 100$, 400 Hz effective PRF case with uniform arrangement is able to be compared to the first two CPIs.

Fig. 4.16 shows a simulation of the Doppler response for the initial and optimized sequences that were transmitted. This pair realizes a 6.8 dB PDSL improvement in simulation. A Monte Carlo analysis for β_{opt} showed that the median improvement in 1000 trials was 4.4 dB.

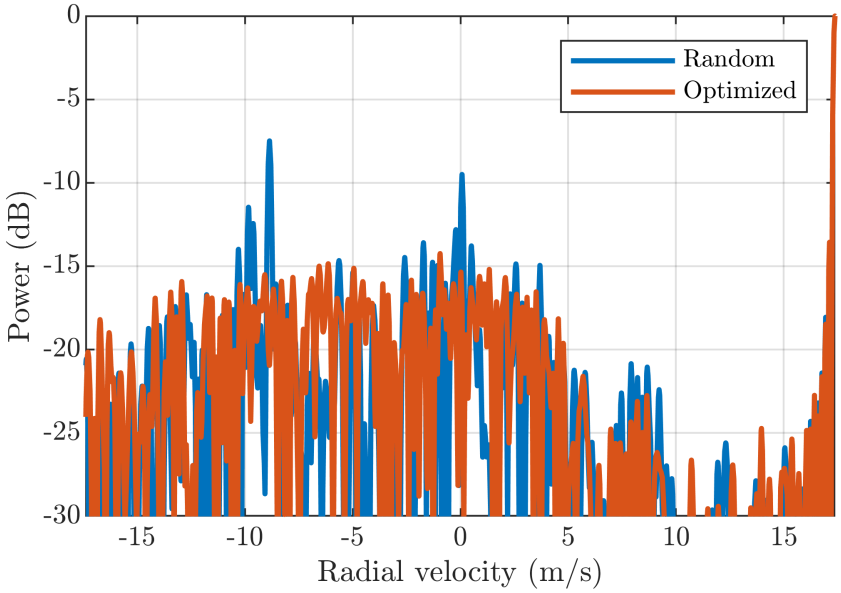

Figure 4.16: Simulated Doppler response of hypothetical mover at the speed limit for random instantiation and corresponding optimized staggering for $M = 100$, $\bar{\delta} = \pm 30\%$, and $\beta_{\text{opt}} = 8$ (6.8 dB PDSL improvement)

4.4.2 Range-Doppler Maps

Each CPI is pulse compressed using a Hamming-weighted mismatched filter (using loopback data) to reduce possible interference from range sidelobes on the ensuing analysis, so that focus can be placed on Doppler sidelobe performance. The range-Doppler maps (RDMs) after pulse

compression, presumming the first 10 pulses, clutter cancellation, and Doppler processing are shown in Figs. 4.17-4.20.

Figure 4.17 shows the ground truth using a uniform sub-CPI of 800 Hz effective PRF to avoid Doppler aliasing. In this figure three movers are pointed out for more detailed observation to follow. The aliased case in Fig. 4.18, where sub-CPIs with an effective PRF of 400 Hz are processed, shows many of the moving cars are ambiguous. If the operating scenario required this effective PRF due to blind range constraints, the necessity for staggering becomes evident.

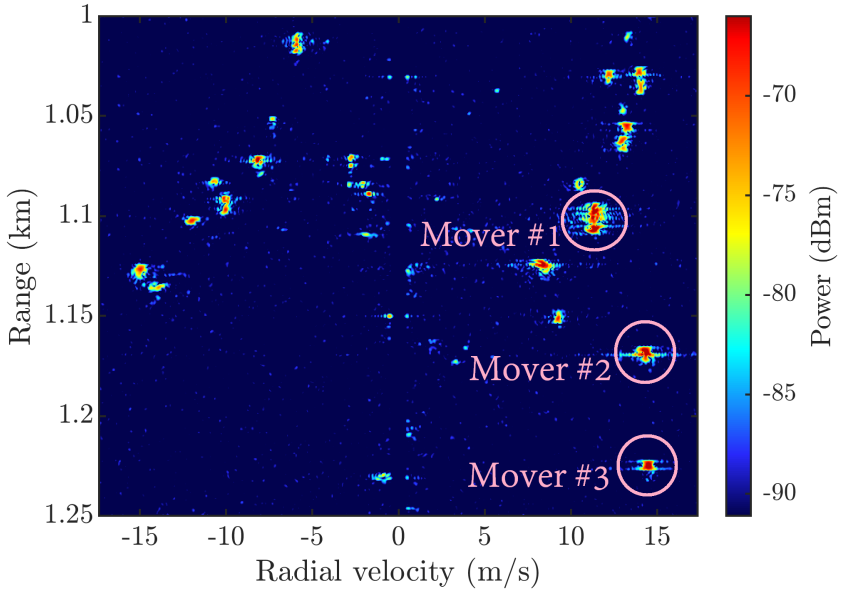

Figure 4.17: Range-Doppler Map of intersection 23rd and Iowa Streets in Lawrence, Kansas. Uniform PRF at 800 Hz uncovers ground truth.

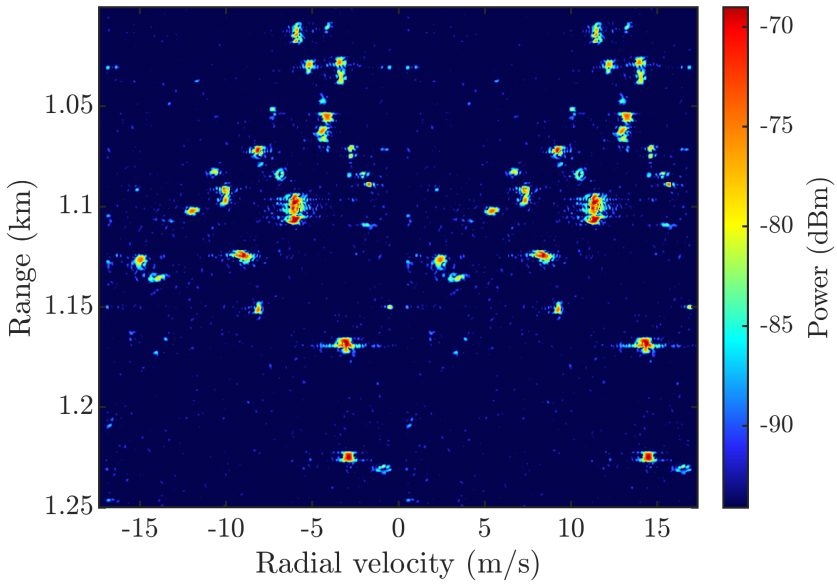

Figure 4.18: Range-Doppler Map of intersection 23rd and Iowa Streets in Lawrence, Kansas. Using uniform PRF at 400 Hz, scene is heavily aliased.

Now compare to the RDMs for the same scene using staggered sub-CPIs, shown in Figs. 4.19-4.20 for purely random staggering and corresponding pseudo-random optimized staggering. As expected, staggering avoids aliasing of the Doppler space seen by the uniform sub-CPI with the same average effective PRF of 400 Hz. However staggering does incur random spurious sidelobes that could appear as false alarms. The optimized case in Fig. 4.20 avoids the false peaks seen in Fig. 4.19, though this particular data set appears to worsen the Doppler sidelobes upon a quick glance, bearing closer examination in the following section.

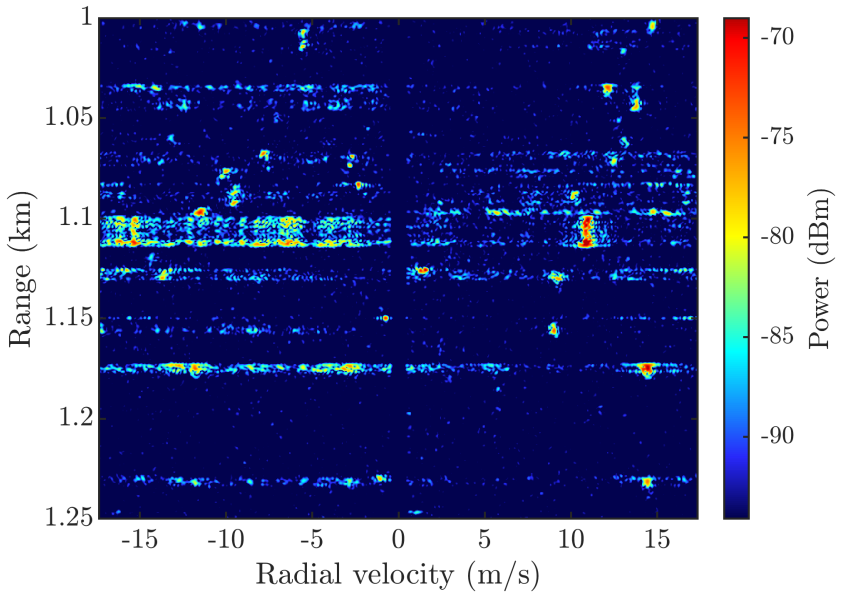

Figure 4.19: Range-Doppler Map of intersection 23rd and Iowa Streets in Lawrence, Kansas. Random staggering uncovers aliased attributes at the cost of increased and random sidelobes that could result in false alarms.

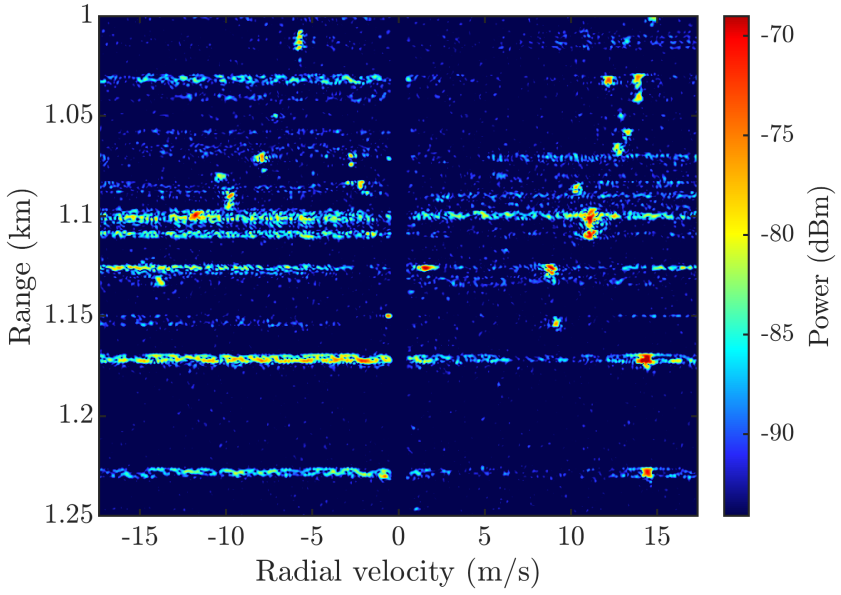

Figure 4.20: Range-Doppler Map of intersection 23rd and Iowa Streets in Lawrence, Kansas. Pseudo-random optimized staggering flattens the peaks from the random case.

4.4.3 Callouts

There are a few interesting comparisons between the random and the optimized cases. For the movers 2 and 3 from Fig. 4.17, optimization appears to worsen the PDSL compared to the random case. Doppler slices from the range bins corresponding to these movers are shown in Figs. 4.21 and 4.22, which reveal a 3 and 5 dB scintillation effect (resulting in a power discrepancy). Though the received SNR has changed for these movers from the random staggering CPI to the subsequent optimized CPI (consequently varying sidelobe level as well), the sidelobe response peak relative to the mainlobe peak is in fact improved by optimization. Mover 2 sees a 4.9 dB relative PDSL improvement while Mover 3 has a 3.9 dB improvement.

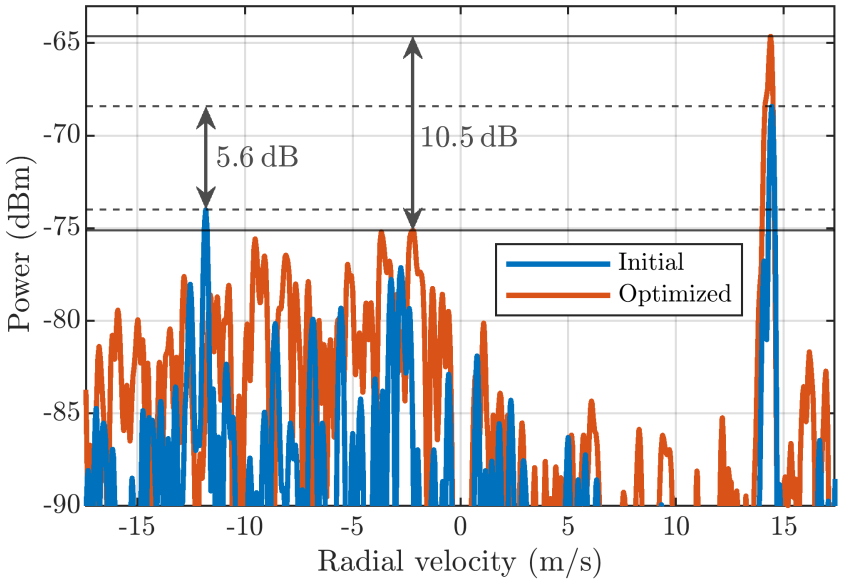

Figure 4.21: Doppler slice for range cell containing Mover 2 showing 4.9 dB PDSL improvement via optimization

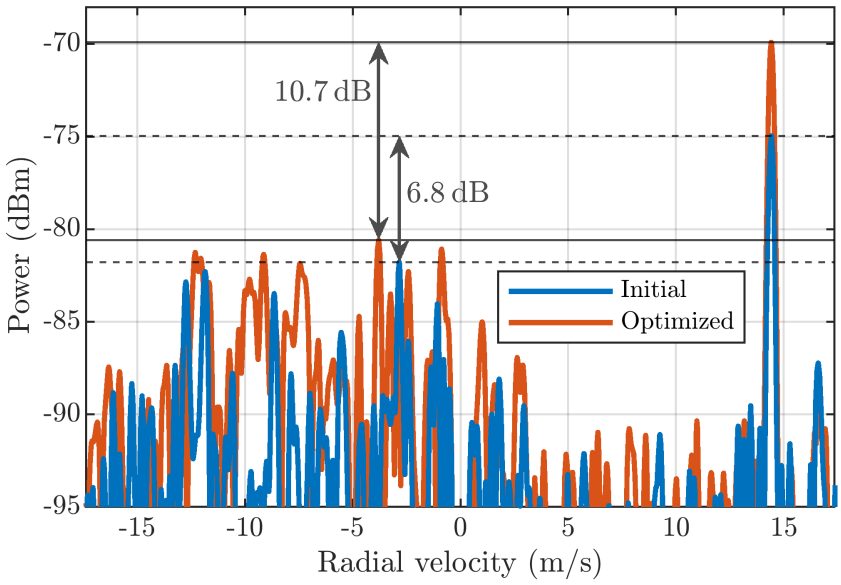

Figure 4.22: Doppler slice for range cell containing Mover 3 showing 3.9 dB PDSL improvement via optimization

Another comparison is shown by Figs. 4.23 and 4.24, which show Figs 4.19 and 4.20 zoomed in around the sidelobes from mover 1 which has about a 15 m range extent and is likely a large truck. The dynamic range depicted is reduced to enhance visibility. For random staggering (Fig. 4.23), large sidelobe peaks occur at Doppler coinciding with the expected peaks for this random PRI sequence from Fig. 4.16. These peaks may be quite problematic, as they are difficult to distinguish from the true scatterer nearby, identified in the figure. The optimized PRI sequence in Fig. 4.24 mitigates this risk of false alarm by flattening the sidelobes, allowing the true target to stand out.

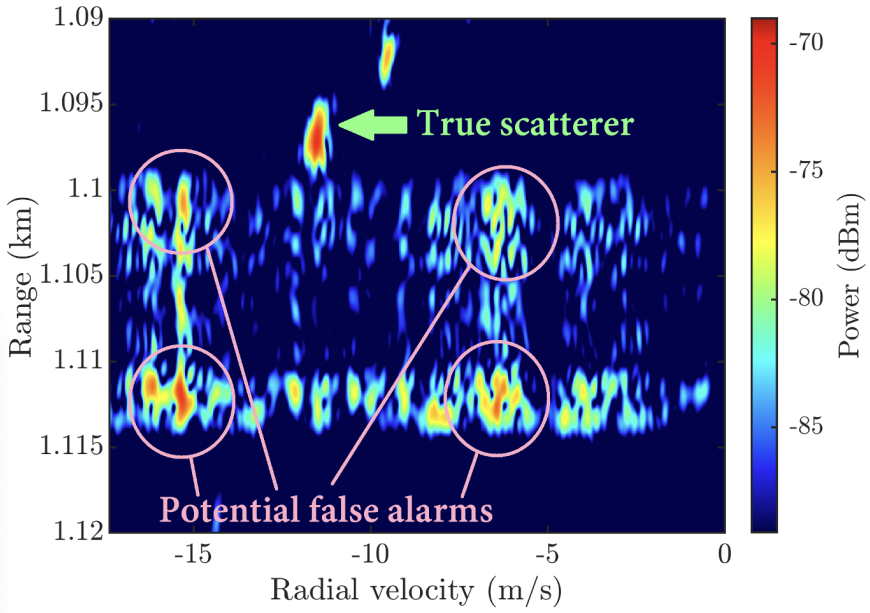

Figure 4.23: Zoomed range-Doppler response of sidelobes from Mover 1 for random staggering

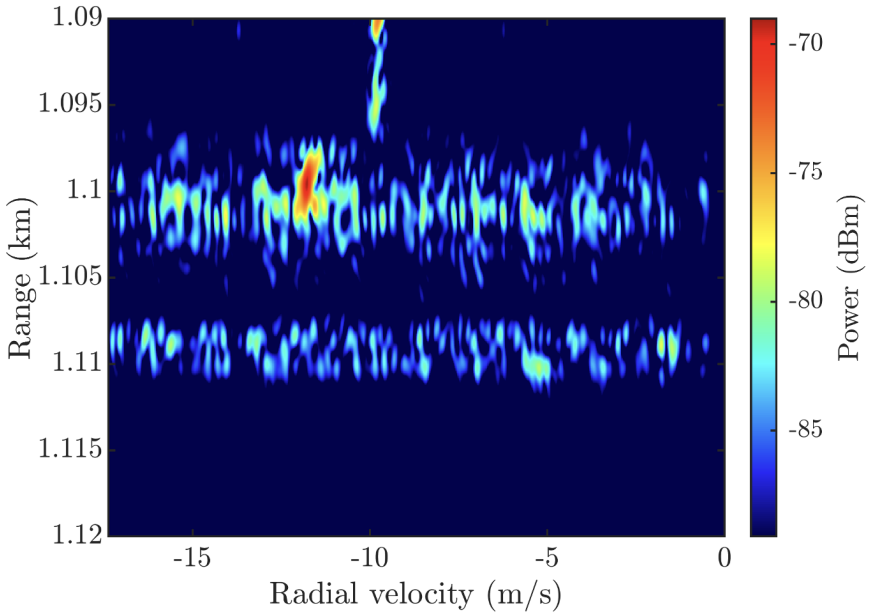

Figure 4.24: Zoomed range-Doppler response of sidelobes from Mover 1 for pseudo-random optimized staggering

The optimized average sidelobe level was limited by the number of pulses $M = 100$ used for these particular open-air measurements. For larger M, the advantage of pseudo-random optimized staggering over random staggering is expected to be even more significant.

In this chapter, a cost function and gradient alongside an optimization procedure were presented for flattening Doppler sidelobes via PRI stagger sequence design. The optimization was shown to improve peak Doppler sidelobe performance significantly in both simulated and open-air measurements, while maintaining a degree of uniqueness between optimized sequences.

Chapter 5

Conclusions and Future Work

This thesis addressed the issue of spurious Doppler sidelobes when using PRI staggering. Characterization of random PRI staggering and redundancy was presented, as well as an optimization method that was demonstrated in simulation and physical experimentation to significantly reduce the peaks present within a prescribed span when using purely random staggering.

Two PRI generation methods were defined and compared. Cumulative staggering affords a higher degree of diversity than grid staggering, enabling the suppression of Doppler sidelobe peaks while using a limited amount of staggering to preserve unambiguous range requirements. By contrast, grid staggering requires much larger staggers to achieve the same level of sidelobe suppression. One potential drawback of cumulative staggering is the requirement of a PRI scaling stage to maintain a fixed CPI extent, which may cause a violation of per-PRI design boundaries. However, given that the amount of necessary staggering is small, and that design boundary violation is rare, cumulative staggering appears to be a superior PRI generation method.

The effect of PRI redundancy on the associated Doppler response and uniqueness was explored using the PRI staggering co-array concept. The degree of redundancy in the PRI sequence determines the unambiguous Doppler interval, and has some effect on peak sidelobe levels, especially for cumulative staggering. It was shown that higher redundancy in a PRI sequence consistently results in a peak sidelobe improvement for cumulative staggering. It was also shown that redundancy in two PRI sequences is negatively correlated with uniqueness between the two.

Though notions about redundancy and the PRI staggering co-array may aid purely random PRI sequence generation, such sequences cannot be expected to tame peak sidelobes due to the inherent randomness and unpredictability. Thus a dedicated sidelobe suppression technique via gradient-

based optimization was demonstrated in this thesis as an effective method for notably improving peak sidelobes. Experimental results corroborated the performance seen in simulation, suggesting the validity of optimization as a method to address the spurious sidelobe problem in random PRI staggering. The optimization was also shown to maintain uniqueness between pseudo-random optimized sequences due to the highly nonconvex nature of the presented cost function.

The PRI staggering co-array detailed in this paper was borrowed from the similar field of sparse array design. Thus it is reasonable to expect that the optimization reported on in this thesis could be used to design sparse arrays for low spatial sidelobes. This is a topic that will be explored in future work. Other future work includes extending the optimization to account for limits imposed by range requirements, multiple time around scattering, and multiple-input multiple-output decoherence characterized in [7]. While Doppler sidelobe suppression imposes an upward design pressure on staggering, these other three aspects present a downward design pressure which optimization may be able to address. Finally, the adaptive receive processing demonstrated in [60] will be performed in conjunction with the optimization presented in this thesis. By using an optimized PRI sequence on transmit, fewer adaptive processing stages may then be required on receive to suppress sidelobes, so the two techniques are expected to be a practical pairing.

Appendix A

Derivation of Expected Doppler Response for Grid Stagger Model

The following leverages the derivation in [7] to develop the expected Doppler response in Eq. 2.28 for the grid stagger model depicted in Eq. 2.30. First, the expectation can be written as

$$E\left[|u(f_{\mathrm{nD}})|^2\right] = E\left[\left|\frac{1}{M}\sum_{m=1}^{M} e^{-j2\pi f_{\mathrm{nD}}\varepsilon_{acc}(m)}\right|^2\right] \tag{A.1}$$

$$= E\left[\left|\frac{1}{M}\sum_{m=1}^{M} e^{-j2\pi f_{\mathrm{nD}}[(m-1)+\Delta\varepsilon_m]}\right|^2\right] \tag{A.2}$$

$$= \frac{1}{M^2}E\left[\left(\sum_{m=1}^{M} e^{-j2\pi f_{\mathrm{nD}}[(m-1)+\Delta\varepsilon_m]}\right)\times\left(\sum_{\tilde{m}=1}^{M} e^{-j2\pi f_{\mathrm{nD}}[(\tilde{m}-1)+\Delta\varepsilon_{\tilde{m}}]}\right)\right]. \tag{A.3}$$

Combining the summations in Eq. A.3, we have

$$E\left[|u(f_{\mathrm{nD}})|^2\right] = \frac{1}{M^2}E\left[\sum_{m=1}^{M}\sum_{\tilde{m}=1}^{M} e^{-j2\pi f_{\mathrm{nD}}[(m-\tilde{m})+\Delta\varepsilon_m-\Delta\varepsilon_{\tilde{m}}]}\right] \tag{A.4}$$

$$= \frac{1}{M^2}\sum_{m=1}^{M}\sum_{\tilde{m}=1}^{M} e^{-j2\pi f_{\mathrm{nD}}(m-\tilde{m})}E\left[e^{-j2\pi f_{\mathrm{nD}}[\Delta\varepsilon_m-\Delta\varepsilon_{\tilde{m}}]}\right] \tag{A.5}$$

$$= \frac{1}{M^2}\sum_{m=1}^{M}\left[1+\sum_{\tilde{m}=1}^{m-1} e^{-j2\pi f_{\mathrm{nD}}(m-\tilde{m})}E\left[e^{-j2\pi f_{\mathrm{nD}}[\Delta\varepsilon_m-\Delta\varepsilon_{\tilde{m}}]}\right] + \sum_{\tilde{m}=m+1}^{M} e^{-j2\pi f_{\mathrm{nD}}(m-\tilde{m})}E\left[e^{-j2\pi f_{\mathrm{nD}}[\Delta\varepsilon_m-\Delta\varepsilon_{\tilde{m}}]}\right]\right]. \tag{A.6}$$

Eq. A.5 exploits linearity, and Eq. A.6 splits the terms in the summation into components where $\tilde{m} = m$, $\tilde{m} < m$, and $\tilde{m} > m$ for separate consideration, as per [7]. Now the expectation is evaluated

for the component where $\tilde{m} < m$ as

$$E\left[e^{-j2\pi f_{\mathrm{nD}}[\Delta\varepsilon_m - \Delta\varepsilon_{\tilde{m}}]}\right] = E\left[e^{-j2\pi f_{\mathrm{nD}}\Delta\varepsilon_m}\right] \times E\left[e^{+j2\pi f_{\mathrm{nD}}\Delta\varepsilon_{\tilde{m}}}\right] \tag{A.7}$$

$$= \left[\int_{-\frac{\bar{\delta}}{2}}^{+\frac{\bar{\delta}}{2}} \left(\frac{1}{\bar{\delta}} e^{-j2\pi f_{\mathrm{nD}}\Delta\varepsilon_q}\right) d\Delta\varepsilon_q\right]^2 \tag{A.8}$$

$$= \left[\frac{\sin(\pi f_{\mathrm{nD}}\bar{\delta})}{\pi f_{\mathrm{nD}}\bar{\delta}}\right]^2 = \left[\mathrm{sinc}(\pi f_{\mathrm{nD}}\bar{\delta})\right]^2, \tag{A.9}$$

and for $\tilde{m} > m$ the expectation is equivalently

$$E\left[e^{-j2\pi f_{\mathrm{nD}}[\Delta\varepsilon_m - \Delta\varepsilon_{\tilde{m}}]}\right] = \left[\mathrm{sinc}(\pi f_{\mathrm{nD}}\bar{\delta})\right]^2. \tag{A.10}$$

Substituting Eq. A.9 and A.10 into Eq. A.6 and simplifying yields

$$E\left[|u(f_{\mathrm{nD}})|^2\right] = \frac{1}{M^2}\sum_{m=1}^{M}\left[1 + \sum_{\tilde{m}=1}^{m-1} e^{-j2\pi f_{\mathrm{nD}}(m-\tilde{m})}\left[\mathrm{sinc}(\pi f_{\mathrm{nD}}\bar{\delta})\right]^2\right. \tag{A.11}$$

$$\left. + \sum_{\tilde{m}=m+1}^{M} e^{-j2\pi f_{\mathrm{nD}}(m-\tilde{m})}\left[\mathrm{sinc}(\pi f_{\mathrm{nD}}\bar{\delta})\right]^2\right] \tag{A.12}$$

$$= \frac{1}{M^2}\left[M + \left[\mathrm{sinc}(\pi f_{\mathrm{nD}}\bar{\delta})\right]^2 \times\right. \tag{A.13}$$

$$\left(\left(M-1\right)2\cos\left(2\pi f_{\mathrm{nD}}(1)\right)\right. \tag{A.14}$$

$$+ (M-2)2\cos\left(2\pi f_{\mathrm{nD}}(2)\right) \tag{A.15}$$

$$\left.\left. \ldots + (1)2\cos\left(2\pi f_{\mathrm{nD}}(M-1)\right)\right)\right] \tag{A.16}$$

$$= \frac{1}{M} + 2\left(\frac{\mathrm{sinc}(\pi f_{\mathrm{nD}}\bar{\delta})}{M}\right)^2 \times \sum_{m=1}^{M-1} m\cos\left(2\pi f_{\mathrm{nD}}(M-m)\right) \tag{A.17}$$

Appendix B

Gradient Derivation

Here the gradient of Eq. 4.2 given in Eqs. 4.3 and 4.4 is derived. First, rewrite the Doppler response as

$$\mathbf{u}(\varepsilon) = \frac{1}{M}\mathbf{V}^H\mathbf{v}_0 \tag{B.1}$$

$$= \frac{1}{M}(\mathbf{v}_0 \otimes \mathbf{I}_{N\times N})\text{vec}\{\mathbf{V}^H\} \tag{B.2}$$

$$= \frac{1}{M}(\mathbf{v}_0 \otimes \mathbf{I}_{N\times N})\bar{\mathbf{v}}_{NM\times 1} \tag{B.3}$$

exploiting the Kronecker identity of the vectorization operation vec$\{\bullet\}$[61], with $\otimes$ the Kronecker product, and $\mathbf{I}$ an identity matrix. The vectorized form of $\mathbf{V}^H = \bar{\mathbf{v}}_{NM\times 1}$ from Eq. B.3 is

$$\bar{\mathbf{v}}_{NM\times 1} = \text{vec}\{\mathbf{V}^H\} \tag{B.4}$$

$$= \exp\left\{-j2\pi\ \text{vec}\{\mathbf{f}_{\text{nD}}\varepsilon^T\mathbf{B}^T\}\right\} \tag{B.5}$$

$$= \exp\left\{-j2\pi(\mathbf{B}\otimes\mathbf{f}_{\text{nD}})\varepsilon\right\}, \tag{B.6}$$

which relies on the identity vec$\{\mathbf{XYZ}\} = (\mathbf{Z}^T\otimes\mathbf{X})vec\{\mathbf{Y}\}$, and where exp$\{\bullet\}$ denotes element-wise exponentiation. Group terms as

$$\theta_{NM\times 1} = (\mathbf{B}\otimes\mathbf{f}_{\text{nD}})\varepsilon \tag{B.7}$$

so that

$$\bar{\mathbf{v}}_{NM\times 1} = \exp\{-j2\pi\theta_{NM\times 1}\}. \tag{B.8}$$

For compactness, the dependence on α is assumed and not written explicitly. Thus Eq. 4.2 is written as

$$J_p = \frac{\| \mathbf{w}_{\text{sl}} \odot \mathbf{u} \|_p^2}{\| \mathbf{w}_{\text{ml}} \odot \mathbf{u} \|_p^2} = \left(\frac{\mathbf{w}_{\text{sl}}^T |\mathbf{u}|^p}{\mathbf{w}_{\text{ml}}^T |\mathbf{u}|^p} \right)^{(2/p)}. \tag{B.9}$$

Leveraging the gradient derivation in the appendix of [55] and by the chain rule, the partial derivative of Eq. 4.2 with respect to parameter α_m is

$$\frac{\partial J_p}{\partial \alpha_m} = \left(\frac{2}{p}\right) J_p \times \left[\frac{1}{\mathbf{w}_{\text{sl}}^T |\mathbf{u}|^p} \left(\mathbf{w}_{\text{sl}}^T \frac{\partial |\mathbf{u}|^p}{\partial \alpha_m} \right) - \frac{1}{\mathbf{w}_{\text{ml}}^T |\mathbf{u}|^p} \left(\mathbf{w}_{\text{ml}}^T \frac{\partial |\mathbf{u}|^p}{\partial \alpha_m} \right) \right], \tag{B.10}$$

in which

$$\frac{\partial |\mathbf{u}|^p}{\partial \alpha_m} = p|\mathbf{u}|^{(p-2)} \odot \left[\left(\frac{\partial |\mathbf{u}|^p}{\partial \alpha_m} \mathbf{u} \right) \odot \mathbf{u}^* + \mathbf{u} \odot \left(\frac{\partial |\mathbf{u}|^p}{\partial \alpha_m} \mathbf{u}^* \right) \right] \tag{B.11}$$

$$= p|\mathbf{u}|^{(p-2)} \odot \Re \left\{ \left(\frac{\partial |\mathbf{u}|^p}{\partial \alpha_m} \mathbf{u} \right) \odot \mathbf{u}^* \right\} \tag{B.12}$$

for $\Re\{\bullet\}$ extracting the real part of the argument. By the chain rule, the partial derivative inside Eq. B.12 is

$$\frac{\partial}{\partial \alpha_m}\mathbf{u} = \frac{1}{M}\frac{\partial}{\partial \alpha_m}\left[(\mathbf{v}_0^T \otimes \mathbf{I}_{N\times N})\bar{\mathbf{v}}\right] \tag{B.13}$$

$$= \frac{1}{M}(\mathbf{v}_0^T \otimes \mathbf{I}_{N\times N})\frac{\partial}{\partial \alpha_m}[\bar{\mathbf{v}}] \tag{B.14}$$

$$= \frac{1}{M}(\mathbf{v}_0^T \otimes \mathbf{I}_{N\times N})\frac{\partial}{\partial \alpha_m}\left[\exp\{-j2\pi\theta\}\right] \tag{B.15}$$

$$= \frac{-j2\pi}{M}(\mathbf{v}_0^T \otimes \mathbf{I}_{N\times N})\left[\exp\{-j2\pi\theta\} \odot \frac{\partial}{\partial \alpha_m}[\theta]\right] \tag{B.16}$$

$$= \frac{-j2\pi}{M}(\mathbf{v}_0^T \otimes \mathbf{I}_{N\times N})\left[\bar{\mathbf{v}} \odot \frac{\partial}{\partial \alpha_m}\left[(\mathbf{B}\otimes \mathbf{f}_{\mathrm{nD}})\varepsilon\right]\right] \tag{B.17}$$

$$= \frac{-j2\pi}{M}(\mathbf{v}_0^T \otimes \mathbf{I}_{N\times N})\left[\bar{\mathbf{v}} \odot \left[(\mathbf{B}\otimes \mathbf{f}_{\mathrm{nD}})\frac{\partial}{\partial \alpha_m}[\varepsilon]\right]\right] \tag{B.18}$$

$$= \frac{+j2\pi\bar{\delta}}{M}(\mathbf{v}_0^T \otimes \mathbf{I}_{N\times N})\left[\bar{\mathbf{v}} \odot \left[(\mathbf{B}\otimes \mathbf{f}_{\mathrm{nD}})(\cos\{\alpha\} \odot \varepsilon)\right]\right], \tag{B.19}$$

where $\mathbf{e}_m$ is an $M \times 1$ elementary vector with 1 in the m^{th} element and zeros elsewhere. Because Kronecker products are computationally expensive, it is convenient to undo the vectorization via the identity above, leading to

$$\frac{\partial}{\partial \alpha_m}\mathbf{u} = \frac{+j2\pi\bar{\delta}}{M}(\mathbf{v}_0^T \otimes \mathbf{I}_{N\times N})\left[\bar{\mathbf{v}} \odot \left[(\mathbf{B}\otimes \mathbf{f}_{\mathrm{nD}})(\cos\{\alpha\} \odot \varepsilon)\right]\right] \tag{B.20}$$

$$= \frac{+j2\pi\bar{\delta}}{M}(\mathbf{v}_0^T \otimes \mathbf{I}_{N\times N})\left[\bar{\mathbf{v}} \odot \mathrm{vec}\{\mathbf{f}_{\mathrm{nD}}(\cos\{\alpha\} \odot \mathbf{e}_m)^T\mathbf{B}^T\right] \tag{B.21}$$

$$= \frac{+j2\pi\bar{\delta}}{M}(\mathbf{v}_0^T \otimes \mathbf{I}_{N\times N}) \times \left[\mathrm{vec}\left\{\mathbf{V}^H \odot \left(\mathbf{f}_{\mathrm{nD}}(\cos\{\alpha\} \odot \mathbf{e}_m)^T\mathbf{B}^T\right)\right\}\right] \tag{B.22}$$

$$= \frac{+j2\pi\bar{\delta}}{M}\left(\mathbf{V}^H \odot \left(\mathbf{f}_{\mathrm{nD}}(\cos\{\alpha\} \odot \mathbf{e}_m)^T\mathbf{B}^T\right)\right)\mathbf{v}_0. \tag{B.23}$$

Substituting Eq. B.23 back into B.12 yields

$$\frac{\partial |\mathbf{u}|^p}{\partial \alpha_m} = p|\mathbf{u}|^{(p-2)} \odot \Re\left\{ \left(\frac{\partial}{\partial \alpha_m} \mathbf{u} \right) \odot \mathbf{u}^* \right\} \tag{B.24}$$

$$= \frac{2\pi\bar{\delta}}{M} p \left[|\mathbf{u}|^{(p-2)} \odot \Im\left\{ \left(\left(\mathbf{V}^H \odot \left(\mathbf{f}_{\mathrm{nD}}(\cos\{\alpha\} \odot \mathbf{e}_m)^T \mathbf{B}^T \right) \right) \mathbf{v}_0 \right) \odot \mathbf{u}^* \right\} \right] \tag{B.25}$$

$$= \frac{2\pi\bar{\delta}}{M} p \, \mathbf{g}_m \tag{B.26}$$

where $\mathbf{g}_m$ subsumes the terms inside the square brackets, containing the Hadamard product between $|\mathbf{u}|^{(p-2)}$ and the $\Im\{\bullet\}$ term, which extracts the imaginary part of the argument. Substituting B.26 into B.10 gives

$$\frac{\partial J_p}{\partial \alpha_m} = \frac{4\pi\bar{\delta}}{M} J_p \left[\frac{\mathbf{w}_{\mathrm{sl}}^T}{\mathbf{w}_{\mathrm{sl}}^T |\mathbf{u}|^p} - \frac{\mathbf{w}_{\mathrm{ml}}^T}{\mathbf{w}_{\mathrm{ml}}^T |\mathbf{u}|^p} \right] \mathbf{g}_m \tag{B.27}$$

$$= \frac{4\pi\bar{\delta}}{M} J_p \, \mathbf{g}_m^T \left[\frac{\mathbf{w}_{\mathrm{sl}}}{\mathbf{w}_{\mathrm{sl}}^T |\mathbf{u}|^p} - \frac{\mathbf{w}_{\mathrm{ml}}}{\mathbf{w}_{\mathrm{ml}}^T |\mathbf{u}|^p} \right], \tag{B.28}$$

which allows for the collection of terms for $m = 1, 2, \ldots, M-1$ as

$$\nabla_\alpha J_p = \frac{4\pi\bar{\delta}}{M} J_p \, \mathbf{G}^T \left[\frac{\mathbf{w}_{\mathrm{sl}}}{\mathbf{w}_{\mathrm{sl}}^T |\mathbf{u}|^p} - \frac{\mathbf{w}_{\mathrm{ml}}}{\mathbf{w}_{\mathrm{ml}}^T |\mathbf{u}|^p} \right] \tag{B.29}$$

for

$$\mathbf{G}_{N \times M} = [\mathbf{0}_{N \times 1} \quad \mathbf{g}_1 \quad \ldots \quad \mathbf{g}_{M-1}] \tag{B.30}$$

References

[1] S.D. Blunt and E.L. Mokole. Overview of radar waveform diversity. *IEEE Aerospace and Electronic Systems Magazine*, 31(11):2–42, 2016.

[2] F. Gini, A. De Maio, and L. Patton. *Waveform Design and Diversity for Advanced Radar Systems*. IET London, UK, 2012.

[3] M. Wicks, S.D. Mokole, E.and Blunt, and B. Schneible. *Principles of Waveform Diversity and Design*. SciTech, 2010.

[4] U. Pillai, K.Y. Li, I. Selesnick, and B. Himed. *Waveform Diversity: Theory & Applications*. McGraw-Hill, 2011.

[5] N. Levanon and E. Mozeson. *Radar Signals*. John Wiley & Sons, 2004.

[6] M. Kaveh and G.R. Cooper. Average ambiguity function for a randomly staggered pulse sequence. *IEEE Transactions on Aerospace and Electronic Systems*, (3):410–413, 1976.

[7] S.D. Blunt, L.A. Harnett, B.G. Ravenscroft, R.J. Chang, C.T. Allen, and P.M. McCormick. Implications of diversified Doppler for random PRI radar. *To appear in IEEE Transactions on Aerospace and Electronic Systems*, 2023.

[8] R.J. Chang, D.B. Herr, J.W. Owen, P.M. McCormick, S.D. Blunt, and J.M. Stiles. On the relationship between PRI staggering and sparse arrays. In *IEEE Radar Conference San Antonio, TX, USA*. IEEE, 2023.

[9] R.J. Chang, C.C. Jones, J.W. Owen, and S.D. Blunt. Gradient-based optimization of pseudo-random PRI staggering. *To appear in IEEE Transactions on Radar Systems*, 2023.

[10] M.A. Richards, J. Scheer, W.A. Holm, and W.L. Melvin. *Principles of Modern Radar*, volume 1. SciTech, 2010.

[11] M.A. Richards. *Fundamentals of Radar Signal Processing*. McGraw-Hill Education, 2014.

[12] M.I. Skolnik. *Radar Handbook*. McGraw-Hill Education, 2008.

[13] D.C. Schleher. *MTI and Pulsed-Doppler Radar*. Artech House, 1932.

[14] H. Nyquist. Certain topics in telegraph transmission theory. *Transactions of the AIEE*, 47(2):617–644, 1928.

[15] C.E. Shannon. Communication in the presence of noise. *Proceedings of the IRE (retitled Proceedings of the IEEE)*, 37(1):10–21, 1949.

[16] C. Doppler. On the coloured light of the binary stars and some other stars of the heavens. *Proceedings of the Royal Bohemian Society of Sciences, Prague (Part V)*, 465:482, 1842.

[17] T.P. Gill. *The Doppler Effect: An Introduction to the Theory of the Effect*. Academic Press, 1965.

[18] C.L. Temes. Relativistic consideration of Doppler shift. *IRE Transactions on Aeronautical and Navigational Electronics*, (1):37–37, 1959.

[19] J.G. Proakis and D.G. Manolakis. *Digital Signal Processing: Principles, Algorithms, and Applications*. Prentice Hall, 1996.

[20] J.E. Quirk, R.J. Chang, J.W. Owen, S.D. Blunt, and P.M. McCormick. A simple yet effective metric for assessing Doppler tolerance. *To appear in IEEE Transactions on Radar Systems*, 2023.

[21] R.J. Sullivan. *Radar Foundations for Imaging and Advanced Concepts*, volume 2. IET, 2004.

[22] P.J.A. Prinsen. Elimination of blind velocities of mti radar by modulating the interpulse period. *IEEE Transactions on Aerospace and Electronic Systems*, (5):714–724, 1973.

[23] R.J. McAulay. The effect of staggered PRFs on MTI signal detection. *IEEE Transactions on Aerospace and Electronic Systems*, (4):615–618, 1973.

[24] Y.X. Lu, Z.Y. Tang, Y.P. Zhang, and L. Yu. Maximum unambiguous frequency of random PRI radar. In *CIE International Conference on Radar Guangzhou, China*. IEEE, 2016.

[25] S.A. Hovanessian. An algorithm for calculation of range in a multiple PRF radar. *IEEE Transactions on Aerospace and Electronic Systems*, (2):287–290, 1976.

[26] G. Trunk and S. Brockett. Range and velocity ambiguity resolution. In *IEEE National Radar Conference Lynnfield, MA, USA*. IEEE, 1993.

[27] G.V. Trunk and M.W. Kim. Ambiguity resolution of multiple targets using pulse-Doppler waveforms. *IEEE Transactions on Aerospace and Electronic Systems*, 30(4):1130–1137, 1994.

[28] P. Stinco, M. Greco, F. Gini, A. Farina, and L. Timmoneri. Analysis and comparison of two disambiguity algorithms: The modified CA and CRT. In *IEEE International Radar Conference "Surveillance for a Safer World" Bordeaux, France*. IEEE, 2009.

[29] F.D.A. García, A.S. Guerreiro, G.R. de Lima Tejerina, J.C.S. Santos Filho, G. Fraidenraich, Mi.D. Yacoub, M.A.M. Miranda, and H. Cioqueta. Probability of detection for unambiguous Doppler frequencies in pulsed radars using the chinese remainder theorem and subpulse processing. In *53rd Asilomar Conference on Signals, Systems and Computers Pacific Grove, CA, USA*. IEEE, 2019.

[30] M. Villano, G. Krieger, and A. Moreira. Onboard processing for data volume reduction in high-resolution wide-swath SAR. *IEEE Geoscience and Remote Sensing Letters*, 13(8):1173–1177, 2016.

[31] A.W. Rihaczek. Radar resolution properties of pulse trains. *Proceedings of the IEEE*, 52(2):153–164, 1964.

[32] R. Roy and O. Lowenschuss. Design of MTI detection filters with nonuniform interpulse periods. *IEEE Transactions on Circuit Theory*, 17(4):604–612, 1970.

[33] M. Sachidananda and D.S. Zrnić. Clutter filtering and spectral moment estimation for Doppler weather radars using staggered pulse repetition time (PRT). *Journal of Atmospheric and Oceanic Technology*, 17(3):323–331, 2000.

[34] M.A. Arbabian, M.H. Bastani, and M. Tabesh. Optimization of PRF staggering in MTI radar. In *IEEE International Radar Conference Arlington, VA, USA*. IEEE, 2005.

[35] M. Villano, G. Krieger, and A. Moreira. Staggered-SAR for high-resolution wide-swath imaging. In *IET International Conference on Radar Systems Glasgow, UK*. IET, 2012.

[36] M. Villano, G. Krieger, and A. Moreira. Staggered SAR: High-resolution wide-swath imaging by continuous PRI variation. *IEEE Transactions on Geoscience and Remote Sensing*, 52(7):4462–4479, 2013.

[37] J.K. Hsiao. On the optimization of MTI clutter rejection. *IEEE Transactions on Aerospace and Electronic Systems*, (5):622–629, 1974.

[38] L.B. Milstein. Reduction of eclipsing loss in high PRF radars. *IEEE Transactions on Aerospace and Electronic Systems*, (2):410–415, 1978.

[39] R. Benjamin. Form of Doppler processing for radars of random PRI and RF. *Electronics Letters*, 24(15):782, 1979.

[40] L. Vergara-Dominguez. Analysis of the digital MTI filter with random PRI. *IEE Proceedings F (Radar and Signal Processing)*, 140(2):129–137, 1993.

[41] M. Modarres-Hashemi and M.M. Nayebi. Performance evaluation of random PRF signals in LPD radars. In *IEEE International Radar Conference Alexandria, VA, USA*. IEEE, 2000.

[42] Z. Liu, X.Z. Wei, and X. Li. Aliasing-free moving target detection in random pulse repetition interval radar based on compressed sensing. *IEEE Sensors Journal*, 13(7):2523–2534, 2013.

[43] J.L. Zhu, T. Zhao, T.Y. Huang, and D.F. Zhang. Analysis of random pulse repetition interval radar. In *IEEE Radar Conference Verona, NY, USA*. IEEE, 2016.

[44] W. van Rossum and L. Anitori. Simultaneous resolution of range-Doppler ambiguities using agile pulse intervals with sparse signal processing. In *IEEE Radar Conference Florence, Italy*. IEEE, 2020.

[45] X.W. Long, K. Li, J. Tian, J. Wang, and S.L. Wu. Ambiguity function analysis of random frequency and PRI agile signals. *IEEE Transactions on Aerospace and Electronic Systems*, 57(1):382–396, 2020.

[46] P.M. McCormick. *Design and Optimization of Physical Waveform-Diverse and Spatially-Diverse Radar Emissions*. PhD thesis, University of Kansas, 2018.

[47] P. Anglin. The application of marginal Fisher's information to radar transmit coding and temporal sampling arrays. Master's thesis, University of Kansas, 2010.

[48] J.M. Stiles and J. Jenshak. Sparse array construction using marginal fisher's information. In *2009 International Waveform Diversity and Design Conference*. IEEE, 2009.

[49] G. Di Martino and A. Iodice. Coprime synthetic aperture radar (CopSAR): A new acquisition mode for maritime surveillance. *IEEE Transactions on Geoscience and Remote Sensing*, 53(6):3110–3123, 2015.

[50] H.L. Van Trees. *Optimum Array Processing: Part IV of Detection, Estimation, and Modulation Theory*. John Wiley & Sons, 2002.

[51] P.M. McCormick and S.D. Blunt. Nonlinear conjugate gradient optimization of polyphase-coded FM radar waveforms. In *IEEE Radar Conference Seattle, WA, USA*. IEEE, 2017.

[52] S.D. Blunt, M. Cook, J. Jakabosky, J. De Graaf, and E. Perrins. Polyphase-coded FM (PCFM) radar waveforms, part i: implementation. *IEEE Transactions on Aerospace and Electronic Systems*, 50(3):2218–2229, 2014.

[53] P.S. Tan, J. Jakabosky, J.M. Stiles, and S.D. Blunt. Higher-order implementations of polyphase-coded FM radar waveforms. *IEEE Transactions on Aerospace and Electronic Systems*, 55(6):2850–2870, 2019.

[54] J.M. Baden, M.S. Davis, and L. Schmieder. Efficient energy gradient calculations for binary and polyphase sequences. In *IEEE Radar Conference Arlington, VA, USA*. IEEE, 2015.

[55] C.A. Mohr, P.M. McCormick, C.A. Topliff, S.D. Blunt, and J.M. Baden. Gradient-based optimization of PCFM radar waveforms. *IEEE Transactions on Aerospace and Electronic Systems*, 57(2):935–956, 2020.

[56] B. White, M.B. Heintzelman, and S.D. Blunt. Alternative "bases" for gradient-based optimization of parameterized FM radar waveforms,". In *IEEE Radar Conference San Antonio, TX, USA*, 2023.

[57] D.G. Felton and D.A. Hague. Gradient-descent based optimization of constant envelope OFDM waveforms. In *IEEE Radar Conference San Antonio, TX, USA*, 2023.

[58] D.C. Liu and J. Nocedal. On the limited memory BFGS method for large scale optimization. *Mathematical programming*, 45(1-3):503–528, 1989.

[59] N. Vervliet, O. Debals, and L. De Lathauwer. Tensorlab 3.0—numerical optimization strategies for large-scale constrained and coupled matrix/tensor factorization. In *50th Asilomar Conference on Signals, Systems and Computers Pacific Grove, CA, USA*. IEEE, 2016.

[60] L.A. Harnett, B.G. Ravenscroft, S.D. Blunt, and C.T. Allen. Experimental evaluation of adaptive Doppler estimation for PRI-staggered radar. In *IEEE Radar Conference New York City, NY, USA*. IEEE, 2022.

[61] K.B. Petersen, M.S. Pedersen, and et. al. The matrix cookbook. *Technical University of Denmark*, 7(15):510, 2008.